Structural Analysis and Client Binding Studies of the ER-Specific Molecular Chaperones BiP and Grp94

A Dissertation

Presented to

The Faculty of the Graduate School of Arts and Sciences
Brandeis University

Graduate Program in Biochemistry & Biophysics

Timothy O. Street, Advisor

In Partial Fulfillment
of the Requirements for the Degree
Doctor of Philosophy

by

Erin Elizabeth Deans

February 2024

This dissertation, directed and approved by Erin Elizabeth Deans' Committee, has been accepted and approved by the Faculty of Brandeis University in partial fulfillment of the requirements for the degree of:

DOCTOR OF PHILOSOPHY

Wendy Cadge, Dean
Graduate School of Arts and Sciences

Dissertation Committee:

Dr. Timothy O. Street, Department of Biochemistry
Dr. Jeff Gelles, Department of Biochemistry
Dr. Daniel Oprian, Department of Biochemistry
Dr. Daniel Bolon, Department of Biochemistry and Molecular Pharmacology, University of Massachusetts Chan Medical School

ACKNOWLEDGEMENTS

In reflecting on my PhD journey, it seems a bit crazy that I made it to the point of writing this thesis. The PhD experience truly challenged me and took me to one of the lowest points I've ever experienced. But I made it here, and much of that is because of my supervisor Dr. Timothy Street. Timo's support and encouragement over the last couple of years allowed me to rediscover my scientific curiosity and love for research. With his patient and thoughtful guidance, I was able to explore the questions I was passionate about (many of which made it into this thesis). The way in which Timo thinks about science and pursues research is inspiring, and I consider myself lucky to have him as a mentor.

I would also like to thank my thesis committee members: Dr. Jeff Gelles, Dr. Daniel Oprian, and Dr. Daniel Bolon. They provided valuable insight on this thesis, and have encouraged me throughout this journey.

Much of the work in this thesis would not have been possible without past and present members of the Street Lab. In particular, thank you to Bin Huang for collecting all of the single-molecule data presented in this thesis, and just overall being a wonderful person to talk to and work with. Thank you to Sam LaRussa for helping me come out of my shell when I first started in the lab and answering all of the little questions I came up with. Thank you to the undergraduate researchers Van Nguyen, Luna Han, Mia Nydam, and Zhilin Luo for your continued support and contributions to this thesis. Thank you to Street Lab alumni Dr. Judy Kotler and Dr. Reyal Hoxie for their contributions as well. And finally, a big thank you to Tara Azam for being a friend, a shoulder to lean on, and unironically being a Twihard with me. Our almost daily lunch dates made the bad days better and the good days into great days.

I truly lucked out that my cohort turned into lifelong friends over the course of this journey. We saw each other through the peaks, pits, and unexpected turns, always laughing along the way (usually at ourselves). So, to everybody's favorite 9th grade English teacher (Michael Sennett), my favorite fun-gi (Alex Sarkis), and the plant goddess (Tina Quasney): thank you.

I would also like to thank my parents and brother who have been my cheerleaders from the beginning, even when I decided to apply to PhD programs instead of veterinary programs at the very last minute. Last, but certainly not least, I have to thank my life partner Jared Martin. Jared, you took a leap of faith moving halfway across the country with me so I could pursue this PhD, even when we had only been dating for a year. Now, a little over six years later, you get to watch me finish this PhD. You have been my biggest supporter, holding me up during the lowest lows and running alongside me during the highest highs. It is impossible for me to put into words my gratitude for you taking on this journey with me. What I can say is that I didn't finish this PhD. Instead, WE finished this PhD.

ABSTRACT

Structural Analysis and Client Binding Studies of the ER-Specific Molecular Chaperones BiP and Grp94

A dissertation presented to the Faculty of the
Graduate School of Arts and Sciences of Brandeis University
Waltham, Massachusetts

By Erin Elizabeth Deans

Hsp70 and Hsp90 are families of ATP-dependent chaperones that are part of a quality control network that maintains cellular homeostasis by assisting protein folding. Hsp90s provide folding assistance for many oncogenic proteins, and numerous Hsp90-specific inhibitors have been developed as potential cancer treatments. Hsp90s have minimal capacity to fold client proteins ("clients") alone and instead often work in coordination with Hsp70s. Recent evidence suggests that the combined Hsp70/Hsp90 system may be an important biological target of Hsp90 inhibitors. However, the structural and mechanistic basis of Hsp70 and Hsp90 coordinated function, and how Hsp90 inhibitors influence this function, remains an active area of research. My thesis focuses on the ER-specific Hsp70/Hsp90 pair, BiP/Grp94, and how these chaperones bind clients and work together.

Hsp70s are able to differentiate between oligomeric and monomeric states of certain clients by binding oligomers with higher affinity than monomers. In contrast, other Hsp70 clients exhibit a negligible difference in affinity between oligomers and monomers. Up until now, it was not known why Hsp70s only bind certain oligomers with high affinity and what the driving force behind this high affinity is. In Chapter 2, I discuss a novel electrostatic steering mechanism by which negatively-charged BiP binds oligomers of a positively-charged client, proIGF2, with high

affinity compared to monomeric peptides. Based on results in the literature, this electrostatic mechanism could be widespread for the Hsp70 family.

Recently, a structure of the cytosol-specific Hsp70/Hsp90 pair bound to a monomeric client was solved (the "loading structure"), which provides new structural insights into cytosolic Hsp70/Hsp90 coordinated function. However, it is unclear if these insights are relevant to the BiP/Grp94 system. In Chapter 3 I examine three questions raised by the loading structure using BiP, Grp94, and proIGF2.

Previous findings from the Street Lab provide the foundation for Chapter 4, where it was found that BiP radically alters the impact of ATP-competitive inhibitors on the conformation of Grp94. Specifically, some inhibitors are compatible with a BiP-stabilized closure intermediate of Grp94 (the "C'-state") while others are not. In Chapter 4, I combine structural data, FRET data, and mutational analysis to discover the basis for this surprising effect. I mutated residues in the Grp94 nucleotide pocket based on candidate structures, one of which being the loading structure. Mutation of a phenylalanine based on the loading structure indicates this residue undergoes a rotamer change in the C' state. Some inhibitors can accommodate this rotamer change while others cannot, explaining the observed conformational specificity of certain Hsp90 inhibitors when bound to Grp94.

The findings in Chapters 3 and 4 show examples in which specific insights from the cytosolic Hsp70/Hsp90 system are applicable to BiP/Grp94. This opens the door for the BiP/Grp94 system to be utilized for structural and mechanistic analysis of Hsp90 inhibitor action on client proteins.

TABLE OF CONTENTS

LIST OF TABLES

LIST OF FIGURES

CHAPTER 1: Introduction

1.1 Hsp90 and Hsp70 Chaperones

Most proteins function by folding into specific three-dimensional structures. Environmental stresses (changes in temperature, pH, etc.) can disrupt protein folding, potentially resulting in protein aggregation and decreased cell viability. A network of molecular chaperones protects against disruptions in protein folding as a way to maintain cellular homeostasis. Heat-shock proteins (Hsp40, Hsp70, Hsp90, etc.) are chaperones that are selectively expressed or upregulated in response to thermal cell stress[1]. Hsp70 and Hsp90 are families of ATP-dependent chaperones that are ubiquitous and highly conserved across eukaryotes, bacteria, and within organelles[2,3]. In metazoans, multiple Hsp90s and Hsp70s are expressed in the cytosol, Grp94 (Hsp90 paralog) and BiP (Hsp70 paralog) are expressed in the ER, and Trap1 (Hsp90 paralog) and Mortalin (Hsp70 paralog) are expressed in mitochondria.

For my thesis, when using the term Hsp70 or Hsp90 I am referring to the families of evolutionarily related chaperones, or general aspects of the chaperones that are shared among family members. When discussing particular members of these families, I will use their specific names (Table 1.1).

Hsp70 and Hsp90 act on diverse states of client proteins. For example, Hsp70s can aid in assembly/disassembly of protein complexes, prevent aggregation of misfolded proteins, and selectively disassemble toxic amyloids and fibrils[4,5]. Hsp90s are involved in numerous cellular processes by binding and stabilizing proteins involved in signaling pathways, and also aid in protein complex assembly. For instance, Hsp90 is required for the assembly of RNA polymerase II without being part of the final complex[6].

Domain/Kingdom	Chaperone Family	Cellular Location	Name
Animalia/Plantae/ Protista	Hsp90	Cytosol	Hsp90α
			Hsp90β
		ER	Grp94
		Mitochondria	Trap1
		Chloroplast (*C. reinhardtii)*	Hsp90C
	Hsp70	Cytosol	Hsp70
			Hsc70
		ER	BiP
		Mitochondria	Mortalin
		Chloroplast (*C. reinhardtii)*	Hsp70B
Fungi (Yeast)	Hsp90	Cytosol	Hsp82
			Hsc82
	Hsp70	Cytosol	Ssa1
Bacteria	Hsp90	Cytosol	HtpG
	Hsp70	Cytosol	DnaK

Table 1.1. Names of Hsp90 and Hsp70 family members.

Mounting evidence suggests that Hsp70/Hsp90 pairs have a conserved combined chaperoning function[7]. For example, Hsp70/Hsp90 pairs from bacteria to humans have a conserved binding interface which enables the two chaperones to bind directly and operate as a concerted unit[8–13]. Uncovering the structural and mechanistic details of this joint function is an active area of research. An important issue is to identify which specific structural and mechanistic features are shared among different Hsp70/Hsp90 systems, and which features are unique to specific Hsp70/Hsp90 systems. My thesis will focus on the ER-specific Hsp70/Hsp90 pair, BiP/Grp94.

Hsp90 is a long established drug target because numerous oncogenic proteins are clients of Hsp90[2,14,15], but recent evidence suggests that the combined Hsp70/Hsp90 system itself may be an important biologically-active target of Hsp90 inhibitors. For example, certain malignant cell lines contain high-molecular-weight chaperone complexes centered around Hsp70 and Hsp90. Cell lines enriched in these complexes are more sensitive to Hsp90 inhibitors[16]. Further, *in vitro* studies show Hsp90 inhibitors can prevent refolding of client proteins by the Hsp70/Hsp90

system[17]. However, the structural and mechanistic basis of how Hsp90 inhibitors influence the Hsp70/Hsp90 system is not well understood. Hsp70/Hsp90 pairs are difficult to study due to both chaperones being large, highly dynamic molecular machines. The cytosolic Hsp70/Hsp90 pair is also extensively regulated by co-chaperones and post-translational modifications (PTMs), making it difficult to experimentally dissect the influence of Hsp90 inhibitors.

Grp94 itself is a potential drug target via its influence on HER2 regulation in certain breast cancers[18]. The BiP/Grp94 pair, which has far fewer co-chaperones and PTMs than the cytosolic Hsp70/Hsp90, is a more tractable system to study the influence of Hsp90 inhibitors. Indeed, in Chapter 4, I discuss previous results from the Street Lab showing that fundamental differences between Hsp90 inhibitors only become apparent when Grp94 is working with BiP. I have found a structural explanation for these previous observations, and identified a conserved residue in the Grp94 nucleotide binding pocket that plays a key role for inhibitor specificity.

1.2 Hsp70 Conformational Cycle

Hsp70 is comprised of the nucleotide binding domain (NBD) and the substrate binding domain (SBD), connected by a flexible linker (Figure 1.1.A). The SBD is divided into the β-region (SBD_β) and the α-helical lid (SBD_α). The SBD_β contains a client-binding cleft in the β-sheet between loops $L_{1,2}$ and $L_{3,4}$[19] (Figure 1.1.B). In the ATP-bound state, the NBD and SBD are docked with an open lid that allows clients to transiently interact with the substrate binding cleft[19,20]. Upon ATP hydrolysis, the NBD and SBD undock and the lid closes against the SBD_β, effectively functioning as a clamp to trap a client. Because of this, the ADP-bound state exhibits slow client dissociation rates[19,21]. When ADP is exchanged for ATP, Hsp70 converts back to the lid-open conformation and the trapped client is released.

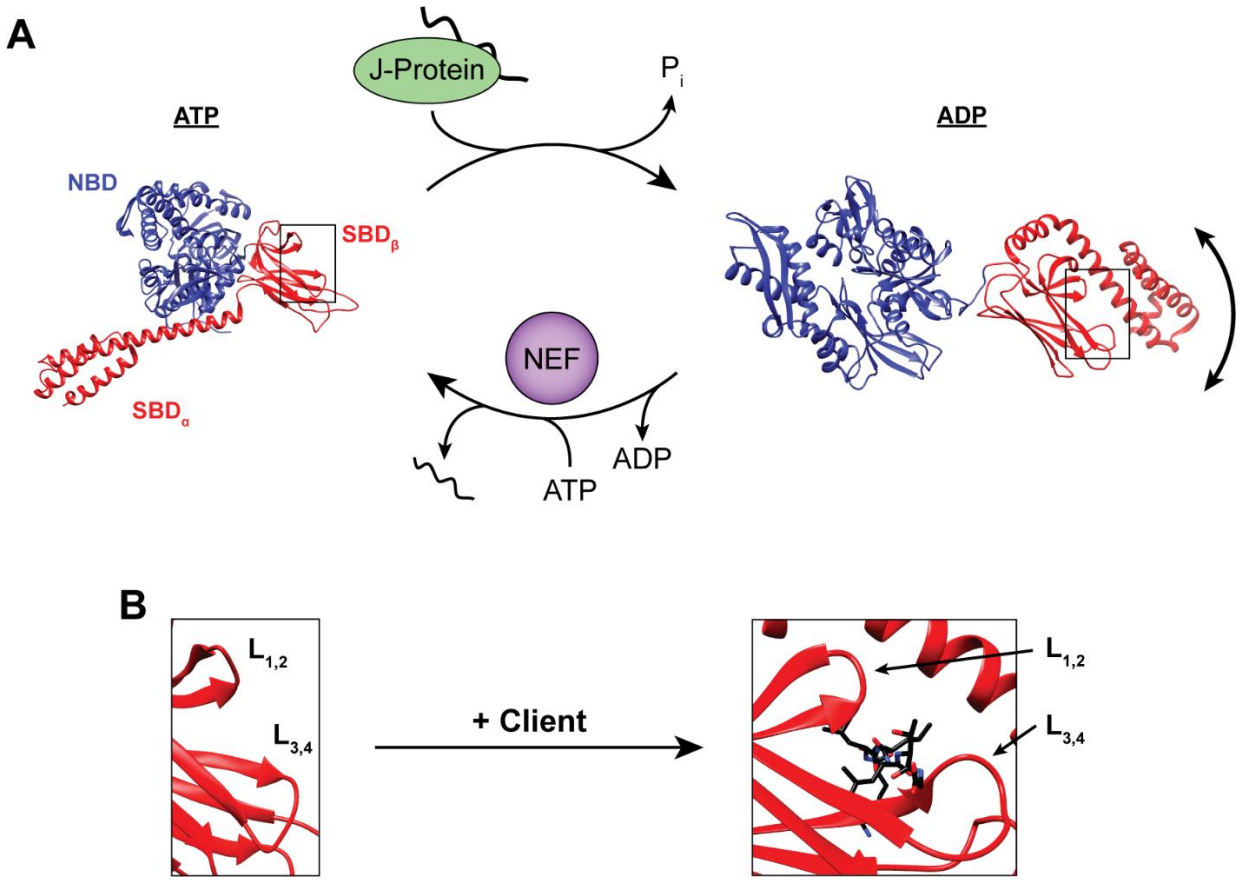

Figure 1.1. A. Hsp70 cycles between the ATP-bound conformation (left, modeled by BiP, PDB: 5E84) and the ADP-bound conformation (right, modeled by DnaK, PDB: 2KHO), regulated by J-proteins and NEFs. NBD is in blue and the SBD is in red. Double arrows represents conformational heterogeneity of the SBD. **B.** Hsp70 client binding cleft on SBD_β without client (left) and with peptide bound (right, PDB: 4PO2, peptide shown in black). Loops in the client-binding site ($L_{1,2}$ and $L_{3,4}$) are numbered according to which β-strands they connect.

In the ADP-bound state the NBD and SBD are only connected by a flexible linker. This results in SBD position heterogeneity that has been characterized by single molecule FRET (smFRET) for numerous Hsp70 family members when in the ADP state, both with and without a bound client protein[22]. The functional role of Hsp70 SBD position heterogeneity (shown schematically by the double-sided arrow in Figure 1.1.A) is not clear.

One possibility is that the NBD/SBD separation is necessary for client binding and the SBD position heterogeneity enables binding of structurally diverse clients. A recent structural

analysis of DnaK argues against this possibility by proposing a model in which client trapping occurs in a "stimulating state" where the DnaK NBD/SBD are not separated[23].

A second possible functional role of SBD position heterogeneity is related to Hsp70 oligomerization, which occurs when Hsp70 is at high concentrations but not bound to clients. BiP oligomerization is well-characterized and results from the SBD of one BiP binding the interdomain linker of a second BiP, meaning the linker is solvent exposed and unstructured to allow for SBD binding. These "cross-protomer" linkages form a chain-like structure which dissociates under ATP conditions[24]. Given the necessity of an unstructured linker, Hsp70 SBD position heterogeneity may be a consequence of the characteristics required for Hsp70 oligomerization.

Hsp70 SBD position heterogeneity may impose a challenge for client handover from Hsp70 to Hsp90. This is because an Hsp70-bound client will be presented to Hsp90 in a wide variety of configurations, but the client must be positioned in a specific location between the Hsp90 dimer arms to be trapped. In Chapter 3, I examine how the SBD position heterogeneity of BiP influences the joint chaperoning function of BiP/Grp94.

Hsp70s have a low intrinsic ATP turnover rate in the range of 0.01-0.5 min^{-1} [4]. Hsp70 conformational cycling is regulated by two classes of co-chaperones: J-domain proteins (*e.g.*, ERdjs in the ER) and nucleotide exchange factors (NEFs, *e.g.*, GrpE in *E. coli* and Sil1 in the ER). J-domain proteins (Hsp40 chaperone family) accelerate Hsp70 ATPase activity and facilitate client trapping (Figure 1.1.A). The J-domain (JD) contains a highly conserved histidine-proline-aspartate (HPD) motif[4]. A crystal structure of the JD from DnaJ (*E. coli* Hsp40) in complex with ATP-bound DnaK shows the JD binding at the NBD-SBD_β docking region and at the linker-SBD_β region[25]. The JD HPD motif is proposed to propagate an allosteric signal to the NBD, inducing a client-dependent destabilization of the NBD-SBD_β interface. Client-induced SBD_β conformational

changes are also proposed to transmit signals through the JD to readjust the interdomain linker, positioning active-site residues in the NBD for ATP hydrolysis[25]. These two allosteric pathways are proposed to effectively couple JD-dependent Hsp70 ATPase stimulation with client trapping. This model of Hsp70 action differs from the model in which a lid-closed ATP-bound "stimulating state" of DnaK is responsible for client trapping[23], therefore this subject remains unresolved and an active area of research.

NEFs accelerate ADP release from Hsp70, which promotes rebinding of ATP and release of a trapped client[4] (Figure 1.1.A). Bacterial, mitochondrial, and chloroplast-specific Hsp70s utilize GrpE homologs as a NEF[26], whereas cytoplasmic and ER-specific NEFs are different. Cytoplasmic Hsp70s utilize three NEFs: Hsp110, HspBP1, and BAG1[4]. Similar to the cytoplasmic Hsp70, BiP utilizes Hsp110 and HspBP1-type NEFs (Grp170 and Sil1 respectively)[4,27]. Currently, there are no known BAG-like NEFs associated with BiP[27].

1.3 Hsp70-Client Interactions

Hsp70s act on a diverse array of protein clients. In comparison to proteases which have well-defined binding motifs, Hsp70s are more promiscuous. However, Hsp70s have some specificity, selectively binding exposed hydrophobic regions of unfolded, misfolded, or partially-folded proteins[28]. Hsp70s recognize short linear motifs consisting of five to seven residues enriched in hydrophobic and basic side chains[29,30]. Five residues of a bound peptide directly interact with the Hsp70 binding cleft[31–33]. Position three is the most specific, favoring leucine residues, and to a lesser extent isoleucine, valine, and proline. Residues at position 1 and 2 are biased to large hydrophobic side chains. Positions 4 and 5 disfavor acidic residues but are

otherwise non-specific[33]. Hsp70s can bind most client proteins in both an N-to-C or C-to-N orientation within the SBD[33].

Hsp70 specificity was determined from studies with short monomeric peptides because the binding of Hsp70s to full-length clients is more complex due to client folding and/or oligomerization. Recent studies show Hsp70 influencing the oligomerization of full-length clients. For example, BiP suppresses oligomerization of the pro-protein of insulin-like growth factor 2 (proIGF2), a BiP/Grp94 client, while having only a modest effect on folding[34]. Cytosolic Hsp70 inhibits tau aggregation by both suppressing nucleation of tau monomers and sequestering tau oligomers and mature fibrils to prevent further elongation. The apparent binding affinity of Hsp70 to tau fibrils increases with the size of the fibril[35]. Hsp70 can also preferentially disaggregate short, toxic amyloid fibrils[5]. Specifically, Hsp70 in collaboration with an Hsp40 and a NEF can disaggregate short α-synuclein and tau fibrils by first destabilizing the fibril ends, unzipping the protofilaments, followed by rapid depolymerization.

A common characteristic of neurodegenerative diseases is the accumulation of misfolded and aggregated proteins[36]. It is important to understand not only the mechanism by which Hsp70s disaggregate, but also how Hsp70s differentiate between oligomeric and monomeric states of client proteins. For certain clients, Hsp70s bind the oligomeric state with a higher affinity than the monomeric state. For example, Hsp70 binds tau fibrils with ~300-fold higher affinity compared to 1-2mers of tau[35]. However, other Hsp70 clients such as α-synuclein and clathrin have a negligible difference in affinity between oligomers and monomers[37,38]. Up until now, it was not known why Hsp70s only bind certain oligomers with high affinity and what is the driving force behind the high affinity.

In Chapter 2, I discuss a novel electrostatic mechanism by which negatively-charged BiP binds positively-charged proIGF2 oligomers with high affinity compared to monomeric peptides. Based on the net charges of various Hsp70 clients, this electrostatic mechanism could be widespread for the Hsp70 family.

1.4 Hsp90 Conformational Cycle

Hsp90 chaperones are homodimers with each monomer comprised of three domains, the N-terminal domain (NTD), the middle domain (MD), and the C-terminal domain (CTD). The NTD binds nucleotides, and the MD makes key contacts with clients and co-chaperones. The CTD dimerizes the Hsp90 arms and also makes key contacts with clients (Figure 1.2.A). Like Hsp70s, Hsp90s have two major conformations. In apo or ADP conditions, Hsp90 adopts an open conformation where the NTDs are separated and the client binding interface on the MD and CTD is exposed[39]. Upon binding of ATP, Hsp90 can adopt a closed conformation in which the NTDs interact. The closed state can trap unfolded clients between the dimer arms[40]. Upon ATP hydrolysis, Hsp90 cycles back to the open conformation and releases bound client.

Hsp90s have a low intrinsic ATPase rate in the range of 0.1-1.0 min^{-1} [2]. For most Hsp90s, arm closure is slower than ATP hydrolysis in the closed state and subsequent reopening, which makes arm closure the rate limiting step in the ATPase cycle[41,42] (Figure 1.2.A). The cytosolic Hsp90 conformational cycle is extensively regulated by co-chaperones, clients, and PTMs. For example, the co-chaperone Aha1 accelerates Hsp90 ATPase by accelerating arm closure[43]. In contrast, the co-chaperones p23 and Hop decrease Hsp90 ATPase by slowing down arm opening and closure, respectively[44,45]. Grp94 lacks co-chaperones homologous to Aha1, p23, or Hop, but Grp94 ATPase is stimulated by its client proIGF2[34], similar to the stimulation of the HtpG ATPase

by the L2 ribosomal protein and model client Δ131Δ[46,47]. Environmental conditions such as pH and molecular crowding also influence Hsp90 activity[48,49].

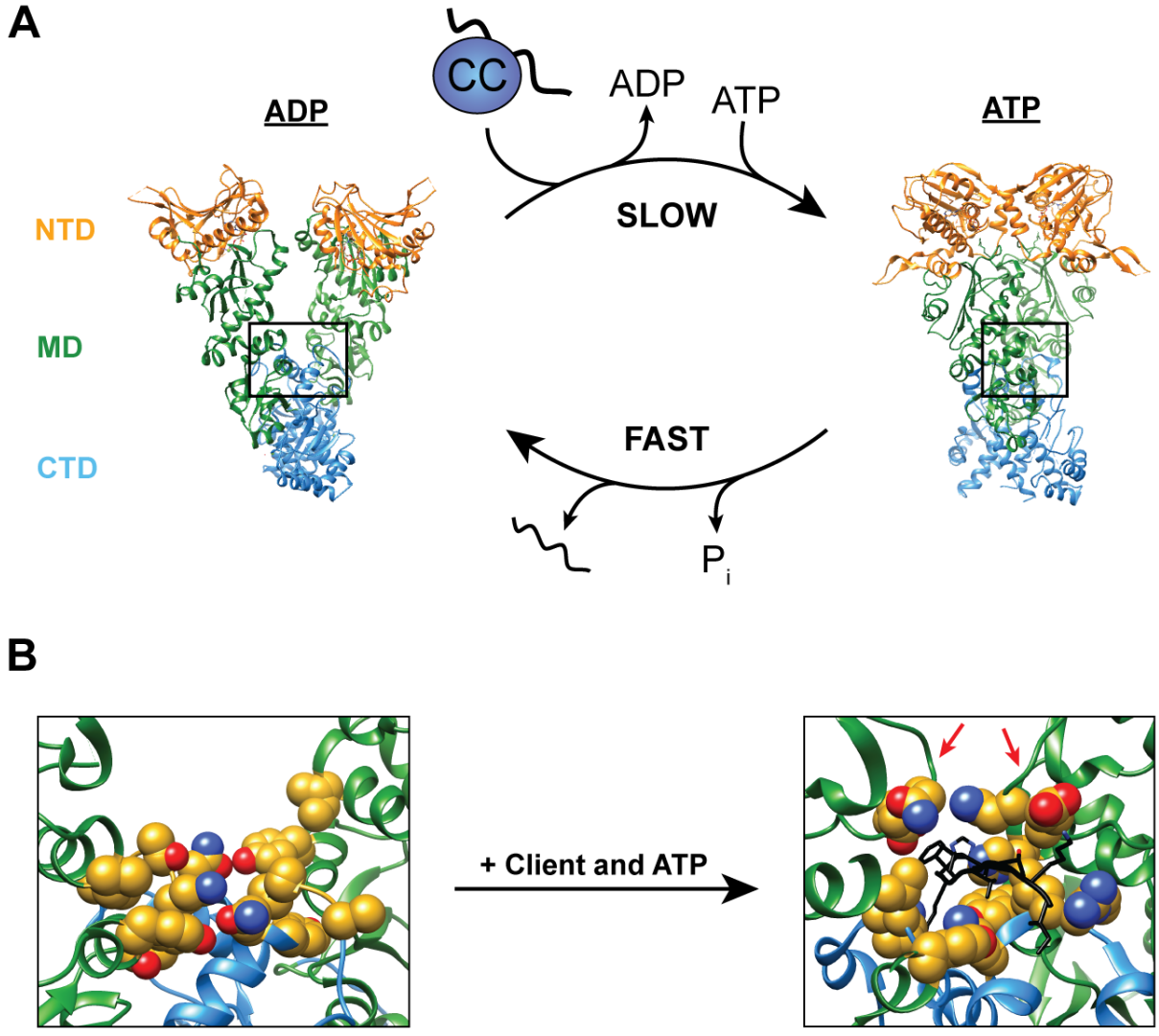

Figure 1.2. A. Hsp90 cycles between the ADP-bound, open conformation (left, modeled by Grp94, PDB: 2O1V) and the ATP-bound, closed conformation (right, modeled by Grp94, PDB: 5ULS). The NTD is shown in orange, the MD is shown in green, and the CTD is shown in blue. Co-chaperone (CC) shown recruiting unfolded client. **B.** Hsp90 client MD/CTD client binding patch without client (left, PDB: 2O1V) and with client bound (right, modeled by Hsp90β bound to CDK4, PDB: 5FWK, client shown in black). Binding patch residues shown in gold, unstructured loops indicated by red arrows.

1.5 Hsp90-Client Interactions

Hsp90s have intrinsically weak affinity for clients, and therefore often require co-chaperones to deliver client proteins[2,7] (Figure 1.2.A). Unlike Hsp70s, for which client binding

specificity can be determined from peptide measurements, the weak affinity of Hsp90 for clients has complicated efforts to define specificity patterns. Studies with various Hsp90 clients have identified widely dispersed client-binding sites on all three Hsp90 domains[7]. However, numerous clients have been shown to interact with a specific extended hydrophobic patch between the MD and CTD. This binding site is crucial for the binding of Hsp90s to the glucocorticoid receptor (GR)[13,50–52], Cdk4 kinase[53], and the model clients L2 and Δ131Δ[54,55]. Structures of Hsp90 show this hydrophobic patch is where unfolded clients are trapped, as discussed next.

At present five high-resolution structures have been determined in which client contacts on the Hsp90 dimer have been visualized (PDB: 5FWK, 7KW7, 7KRJ, 5ULS, 8FX4). Four client bound structures are of Hsp90 in the closed state, and one is in a semi-closed conformation which will be discussed later. At present there are no high-resolution structures of Hsp90/client in the open state. In the closed state, the residues of the hydrophobic patch form a U-shaped tunnel with unstructured loops on the MD enclosing the client (Figure 1.2.B, right). In contrast, the residues of the hydrophobic patch do not form a continuous surface in the open state (Figure 1.2.B, left). Based on the available structures, Hsp90 binds 7-9 client residues within its binding cleft. Similar to Hsp70, the five core residues are comprised primary of aliphatic residues. Unlike Hsp70, Hsp90 can also accommodate polar client residues in the binding cleft. This may be due to the MD loops being able to adopt different conformations based on the client sequence (see arrows in Figure 1.2.B).

While Hsp90/client structures have yielded insights about how Hsp90s bind clients, questions remain about how Hsp90s work on clients. For example, opposite to Hsp70s, which suppress client oligomerization, Hsp90s can enhance client oligomerization. Cytosolic Hsp90 promotes oligomerization of tau[56,57] while Grp94 promotes oligomerization of proIGF2 and

myocilin[34,58]. Interestingly, while Hsp90 promotes oligomerization, it can also prevent a transition to irreversible aggregates[56,59,60]. Grp94 can work upstream of BiP to suppress the formation of insoluble luciferase aggregates under strong denaturation conditions[60]. Further, Grp94 has been shown to preferentially act on proIGF2 oligomers instead of aggregates[34], and a similar observation has been made for cytosolic Hsp90 and α-synuclein[59]. This indicates Hsp70 and Hsp90 can both decrease client aggregation, albeit by different mechanisms.

1.6 Evolutionarily Conserved Collaboration Between Hsp90 and Hsp70

In 1992, one of the first indications of Hsp70/Hsp90 collaborative function came from the Toft lab observing that adding an α-Hsp70 antibody to rabbit reticulocyte lysate disrupts client binding to Hsp90[61]. Later, pulldown assays identified Hsp70 and Hsp90 complex with Hop (Hsp70/Hsp90 Organizing Protein)[62], and the complex could be disrupted by an α-Hop antibody[63]. Finally, the Hsp70/Hsp90/Hop complex was determined to be a key step in the binding of GR and progesterone receptor clients to Hsp90[62,64]. Interestingly, recent findings have identified an alternative pathway by which Hsp90 can receive GR without utilizing Hop[65].

These initial findings on Hsp70 and Hsp90 collaborative function were determined from experiments on metazoan cell lysates. However, more recently the *E. coli* Hsp70/Hsp90 pair (DnaK/HtpG) were shown to collaborate in client protein remodeling[66], even though *E. coli* does not encode a Hop-like protein to mediate DnaK/HtpG interaction. A major step forward was the proposal of DnaK/HtpG direct interaction via the DnaK NBD and HtpG MD[8,9]. This binding interface, later termed interface I, was also shown to be important for the collaboration of yeast Hsp70/Hsp90 despite this system possessing a Hop-like protein[10,11]. A direct interaction of the mitochondrial Hsp70/Hsp90 pair via interface I has been suggested[67], but further characterization

is needed. Despite these advances, some ambiguity remained because the assays used to analyze DnaK/HtpG provided mostly indirect evidence about their interaction.

Similar to the bacterial Hsp70/Hsp90 system, previous findings also suggested a direct BiP/Grp94 interaction despite the lack of Hop co-chaperone in the ER. For example, Grp94 co-precipitates with BiP in pulldown assays[68] and both chaperones associate with unassembled immunoglobulin chains[69,70]. Pulldown measurements suggested BiP/Grp94 function sequentially, in which clients bind to BiP first and Grp94 second[70]. A similar sequence was proposed for DnaK/HtpG[17] and the cytosolic Hsp70/Hsp90 system[71–73], although the mechanistic explanation was unclear.

1.7 BiP and Grp94

Findings with the bacterial Hsp70/Hsp90 system paved the way for discoveries with the BiP/Grp94 system. The development of a binding assay for BiP and Grp94 confirmed their direct interaction via the BiP NBD and Grp94 MD (interface I)[12]. These measurements also indicated that the Grp94 NTD provides an additional contribution to the binding of BiP. As discussed later, this NTD contribution is now understood by a secondary interaction interface (interface II).

The BiP/Grp94 measurements not only validated the interacting domains, but also confirmed the specific residues identified as bridging DnaK/HtpG. For example, two DnaK/HtpG mutations that cause both *in vivo* and *in vitro* interaction defects[8,9] correspond to E243A and K467A on BiP and Grp94, respectively. Mutation of either of these residues abolishes the BiP/Grp94 interaction[12]. These residues are highly conserved for Hsp70/Hsp90 pairs, which suggests an evolutionarily conserved Hsp70/Hsp90 function. The K467A mutation also enables

the construction of Grp94 heterodimers where only one BiP can bind, which is an important element of the experimental design in Chapter 3.

As discussed above, Hsp70s and Hsp90s often exhibit ordered client binding, but the explanation was not clear. The BiP/Grp94 system provided insight into this subject. In binding assays BiP exhibits a ~20-fold higher affinity for Grp94 under ADP conditions compared to ATP[12]. Nucleotide-specific association of BiP and Grp94 is a simple mechanism that imposes ordered interactions with clients (Figure 1.3, steps 1 and 2). A docking model of BiP and Grp94 provided a structural explanation in which the SBD clashes with Grp94 when BiP is in the ATP-bound state[12]. This explanation was later confirmed by a cryoEM structure[13]. One unexplained aspect of the binding between BiP and Grp94 was that full-length BiP bound Grp94 with higher affinity than the NBD under ADP conditions[12]. The cause of this difference is discussed in Chapter 3, in which I have found that the BiP SBD has a docking site on the Grp94 CTD.

Nucleotide-specific regulation of BiP/Grp94 interaction makes sense in the context of BiP's involvement in the unfolded protein response (UPR), which is a cellular stress response to the accumulation of misfolded proteins in the ER lumen. UPR signaling is mediated by transducers which detect the accumulation of misfolded proteins and transmit signals to upregulate UPR target genes. BiP binds UPR transducers under normal conditions and dissociates under stress conditions[74–76], suggesting that BiP suppresses the UPR by binding transducers to prevent activation and signal transmission. A well-supported model is that the UPR is initiated by accumulation of misfolded proteins in the ER that causes competition for BiP binding, allowing for transducer activation and signal transmission[77]. BiP has higher affinity for ATP versus ADP[78], meaning it will be in the ATP state when bound to UPR transducers. If BiP/Grp94 interaction was not nucleotide-specific, Grp94 and UPR transducers would compete for BiP binding in unstressed

conditions which could inadvertently activate the UPR. Prolonged UPR signaling has been linked to numerous neurodegenerative, inflammatory, and metabolic diseases[79].

Conformation-specific binding of BiP/Grp94 explained how client proteins are presented to Grp94, but major questions remained. For example, the slow arm closure of Hsp90 (0.1-1 min^{-1}) poses a problem for client trapping. Hsp90's inherently low affinity for clients implies a fast dissociation rate, making client trapping kinetically unlikely. The next discovery with the BiP/Grp94 system was that BiP accelerates Grp94 closure, changing the rate-limiting step from closure to opening[80]. In the working model of BiP/Grp94 coordinated function, BiP traps a client protein in the ADP conformation and selectively associates with Grp94. Binding of BiP to Grp94 provides the stimulation for Grp94 to trap the client presented by BiP (Figure 1.3, steps 3 and 4). The efficiency of client transfer from BiP to Grp94 remains unknown (indicated by question mark at step 4 in Figure 1.3).

BiP accelerates Grp94 closure by thermodynamically stabilizing a Grp94 closure intermediate, termed the C' state[80] (Figure 1.3, step 3). The control of Grp94 closure kinetics via a high-energy conformational intermediate is reminiscent of the role of high-energy states in enzyme catalysis that control the rate of substrate turnover. In smFRET experiments, the C' state has FRET efficiency higher than that of the closed conformation, suggesting that the C' state involves a rearrangement of the Grp94 NTDs[80]. A structure of the C' state has not been determined, but a structure of a Trap1 NTD dimer in a "coiled-coil" conformation is a candidate because the fluorophore locations are predicted to be closer than in the Grp94 closed state[80,81]. A Grp94 crosslinking mutant derived from the coiled-coil conformation shows robust disulfide formation in the presence of BiP, and a ~50-fold increase in affinity between crosslinked Grp94 and BiP versus wild type[80]. More recently, a structure of Hsp90α in a semi-closed conformation was

published[13]. This structure is also a candidate for the Grp94 C' state, raising the question of if the C' state more closely resembles the semi-closed or coiled-coiled conformation (indicated by question mark at step 3 in Figure 1.3).

Before the discovery that BiP stabilizes the Grp94 C' state, it was known that Grp94 can adopt an alternative closed state when the chaperone has ATP and ADP on opposite arms. For context, most available structures of the Hsp90 closed conformation have two bound ATP molecules, but the mixed ATP/ADP state is likely to predominate under biologically-relevant nucleotide conditions[82–84]. Little was known about the mixed ATP/ADP state because for most Hsp90 homologs the closed state is transient under ATP turnover conditions[41,47,82,83]. Grp94 has a slower opening rate compared to other Hsp90 homologs, resulting in robust closed state accumulation under ATP conditions[85]. Grp94 smFRET measurements with ATP show two closed states. The first has characteristics of the known Grp94 closed state. The second is a dynamic, alternative closed state with higher FRET efficiency than the closed conformation. Grp94 can cycle between the closed conformation and this alternative closed conformation[85], but the functional role of closed state cycling is unknown (indicated by question mark at step 6 in Figure 1.3). For my thesis I will also refer to this alternative closed conformation as the C' state since no structure has been determined to differentiate it from the C' state stabilized by BiP.

The C' state is populated under mixed nucleotide conditions, suggesting that Grp94 can undergo sequential ATP hydrolysis[85]. With two ATP molecules bound, Grp94 remains in the closed conformation (Figure 1.3, step 4). Upon the first hydrolysis event, Grp94 adopts a dynamic ATP/ADP state that can cycle between the closed and C' conformations (Figure 1.3, step 5 and 6). Hydrolysis of the second ATP molecule causes a rapid transition from the C' to open conformation (Figure 1.3, step 7).

While considerable progress has been made in understanding BiP/Grp94 coordinated function, key questions remain. For example, the stoichiometry of BiP to Grp94 necessary to accelerate Grp94 closure is not known. The observation of BiP-dependent closure acceleration was made under conditions which allowed one or two BiPs to bind Grp94[80]. Until recently, structural details of Hsp70/Hsp90 interaction were limited to docking models. A new structure of Hsp90α in complex with Hsp70 provides a tool to answer these open questions in the BiP/Grp94 system.

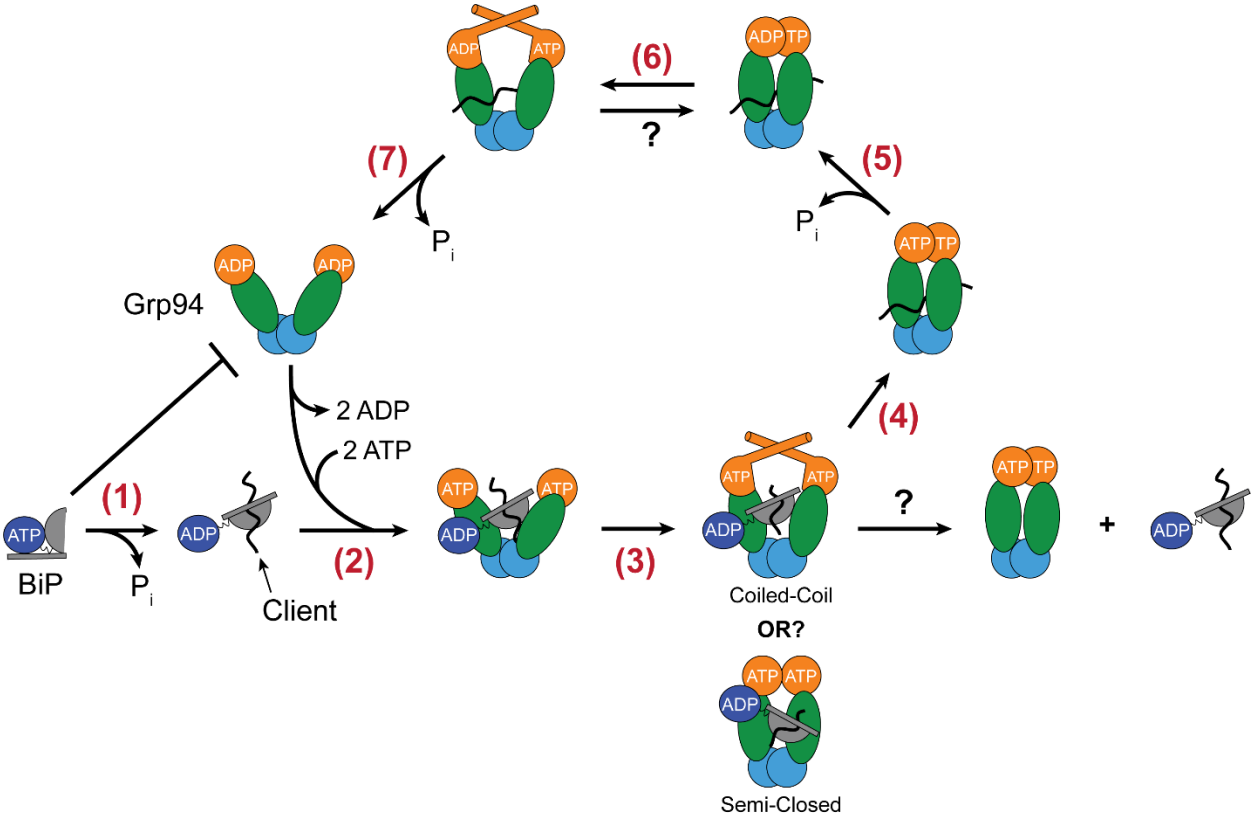

Figure 1.3. Working model of BiP/Grp94 function. (1) ATP conformation of BiP is unable to bind Grp94. BiP traps a client, driven by ATP hydrolysis. (2) Client-bound BiP binds to the open conformation of Grp94. (3) BiP binding stabilizes the C' conformation of Grp94. Question mark denotes unknown structure of the BiP-stabilized C' conformation. (4) Stabilization of the C' state accelerates closure of Grp94, trapping the client presented by BiP. Question mark denotes the unknown efficiency of client transfer between BiP and Grp94. (5) First Grp94 hydrolysis event. (6) Conformational cycling of the dynamic ATP/ADP Grp94 closed state. Question mark denotes unknown function of Grp94 closed state conformational cycling. (7) Second Grp94 hydrolysis event and rapid opening. Bound ADP molecules are exchanged for ATP, readying Grp94 for BiP binding. P_i denotes inorganic phosphate.

1.8 Hsp70/Hsp90/Hop/GR Loading Structure

The Hsp70/Hsp90/Hop/GR loading structure reveals an Hsp90α dimer bound to GR and flanked by two symmetrically bound Hsp70s, with the whole complex stabilized by Hop[13] (Figure 1.4.A). The Hsp90 dimer is in a "semi-closed" conformation where the NTDs are rotated similarly to the closed state, but lid closure over the nucleotide-binding pocket has not occurred and the arms have not yet fully closed. Comparison of the semi-closed and closed lid structure is shown in Figure 1.4.B. In the semi-closed NTD structure, lid residues form a dimer interface with the opposing arm's NTD (teal residues in Figure 1.4.B). The lid must be in an open conformation to form this dimer interface, but it was unclear if this lid structure is relevant for substrate binding or Hsp90 closure. The potential relevance of this structural feature will be discussed later.

The client, GR, is in a partially unfolded state. The folded, globular region of the GR lies on one side of Hsp90 with the unfolded region passing through the Hsp90 arms. On the opposite side of Hsp90, the unfolded region of GR is held in place between the Hsp90 arms by Hop and further extends into the Hsp70 SBD binding cleft. The partially unfolded state of GR is reminiscent of Hsp90 trapping an unfolded region of the Cdk4 kinase[53].

The NBDs of each Hsp70 interact with Hsp90 through two interfaces. The first is interface I. The loading complex structure validates not only the interacting domains, but also the specific residues bridging the domains. The second interface, termed interface II, is a previously unknown binding region between the Hsp70 NBD and Hsp90 NTD. The interaction between the two chaperones at interface II notably orients the Hsp90 NTD in relation to the MD. Hsp90 mutations at interface II cause growth defects in yeast cells[13,86]. However, interface II mutations in the Hsp90 open state are likely destabilizing the chaperone and making resulting defects difficult to interpret.

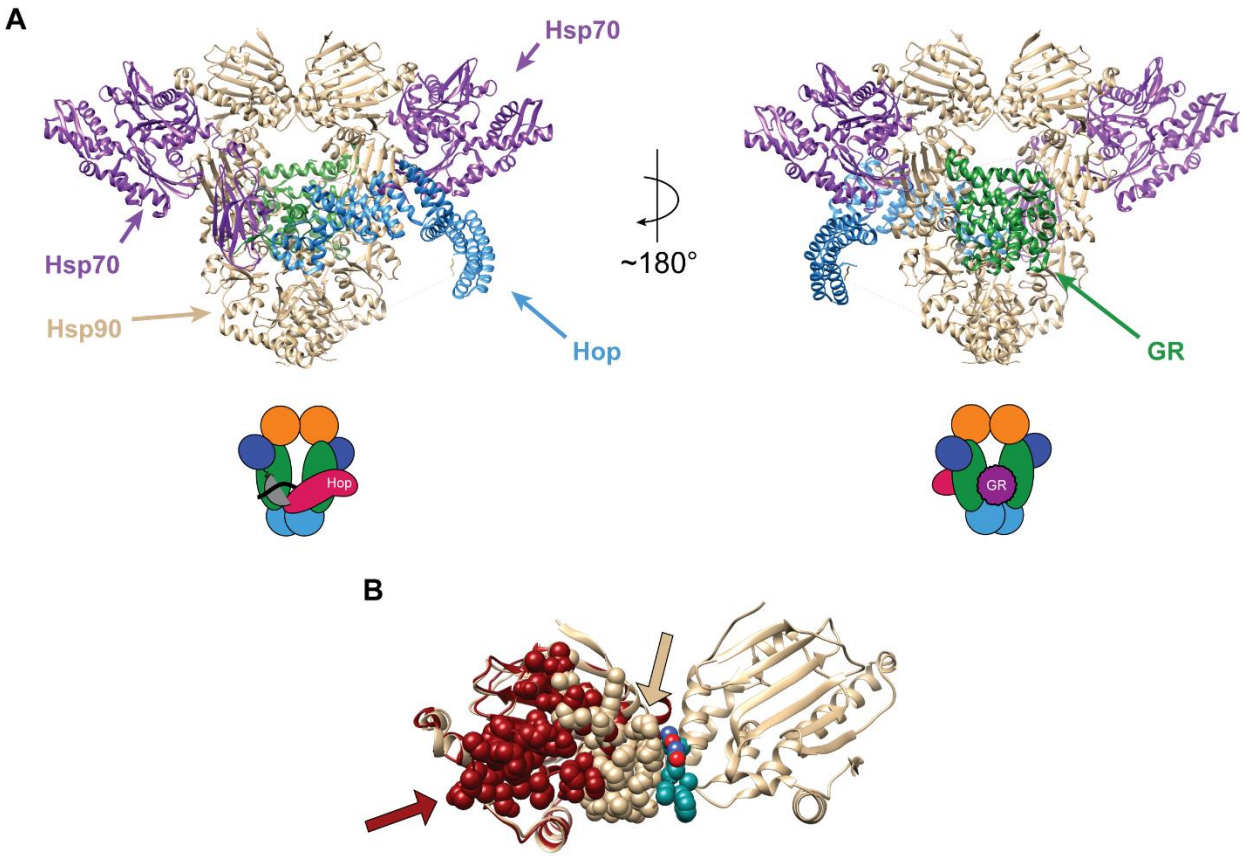

Figure 1.4. A. Front (left) and back (right) view of Hsp90:Hsp70:Hop:GR loading complex cryoEM structure (PDB: 7KW7). Hsp90 is shown in tan, Hsp70 is shown in purple, Hop is shown in blue, and GR is shown in green. Cartoon representations shown underneath the corresponding view. **B.** Overlay of NTDs from Hsp90 semi-closed conformation (tan, PDB: 7KW7) and Hsp90 closed state (red, PDB: 5FWK). Semi-closed NTD dimer interface shown in teal. Lid structures shown in space filling. Tan arrow pointing to lid conformation in the semi-closed conformation, red arrow pointing to the lid conformation in closed state.

An interesting aspect of the Hsp70/Hsp90 loading structure is that the Hsp90 nucleotide pocket configuration is sterically incompatible with nucleotide binding due to a steric clash with Phe138 (Figure 1.5). This residue appears to stabilize the lid-open conformation by making a hydrophobic cluster with lid residues, allowing for formation of the NTD dimer interface (teal residues in Figure 1.4.B and 1.5). In Chapter 4, I show that the unusual position of Phe138 provides an explanation for why some ATP-competitive inhibitors are compatible with the C' state of Grp94 while others are not[87], indicating the Phe138 rotamer change and resulting lid-open conformation are relevant to the C' state and Grp94 closure.

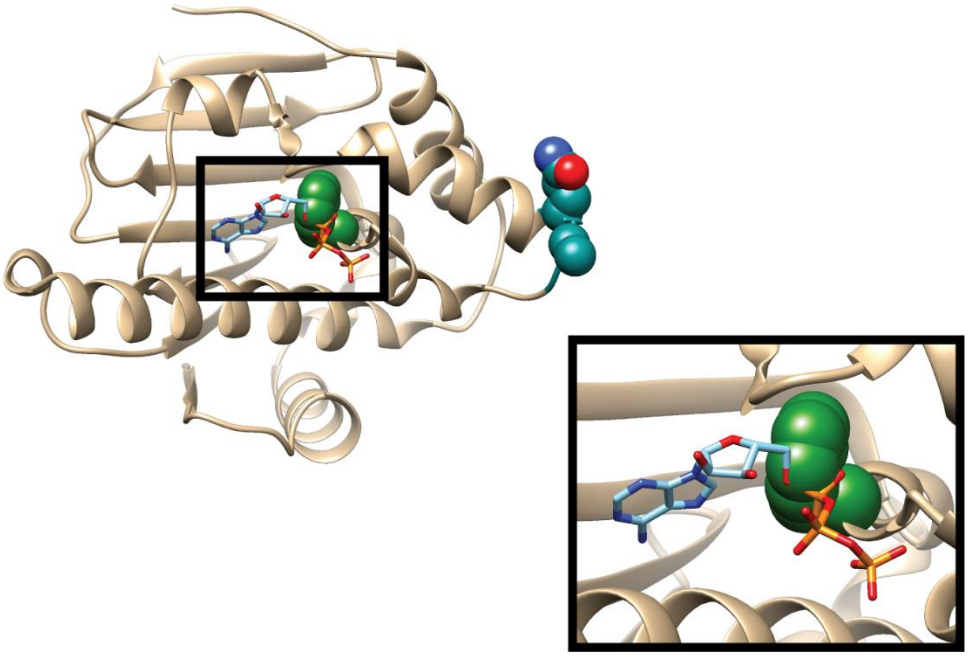

Figure 1.5. Superposition of ATP-bound Hsp90 NTD structure (PDB: 3T0Z) and the semi-closed Hsp90 NTD structure (PDB: 7KW7). Semi-closed Hsp90 shown in tan, ATP shown in light blue, Phe138 shown in green. Semi-closed NTD dimer interface shown in teal.

While Hsp70 delivers unfolded GR to the loading complex, it does not directly position GR within the Hsp90 arms. Instead, Hop guides the unfolded region of GR between the Hsp90 arms. This raises a question of how Hsp70 guides clients on Hsp90 without Hop. One possibility is that the Hsp70 SBD can guide the client, but the loading complex structure provides little insight into how this could occur. The SBD region bound to GR in the loading complex is low-resolution and lacks the α-helical lid region, while the SBD on the second Hsp70 is not visible at all. The lack of a well-defined position of the SBD may be due to the extensive contacts of Hop and the globular region of GR on either side of the Hsp90 binding cleft, which occupy much of the available regions for potential SBD docking. In Chapter 3 I discuss the discovery of new interaction interfaces between the BiP SBD and Grp94 which may play a role in client positioning during transfer.

1.9 ProIGF2

ProIGF2 is the pro-protein of insulin-like growth factor 2 (IGF2). IGF2 is a member of the insulin family of hormones, which also includes insulin and IGF1. IGF1 and IGF2 have overlapping functional roles *in vivo*, with IGF2 preferentially expressed during early embryonic and fetal development and IGF1 preferentially expressed after birth and peaking at puberty[88,89]. Expression of both hormones declines into adulthood[88]. IGF2, specifically, is a crucial factor in fetal and placental cell growth, as well as cell migration and differentiation[88,90].

IGF2 is synthesized as a precursor hormone, termed pre-proIGF2, which contains an N-terminal ER-signaling sequence. This signal sequence is cleaved upon entrance to the ER, yielding proIGF2. ProIGF2 is composed of a 67-residue hormone region (mIGF2) followed by an 89-residue E-peptide region. The hormone region folds in the ER via three disulfide bonds that stabilize three α-helices, whereas the E-peptide region is mostly disordered[34]. Once folded, proIGF2 is translocated to the Golgi where the E-peptide is glycosylated to promote further processing[91]. ProIGF2 is proteolytically cleaved to yield IGF2 and an additional hormone, preptin[91,92]. Preptin is located at the beginning of the E-peptide region of proIGF2 and is co-secreted with IGF2.

ProIGF2 is a stringent client of the BiP/Grp94 system due to the essential role Grp94 plays in IGF2 folding and secretion. Embryonic stem cells that lack Grp94 are unable to differentiate into muscle cells and are hypersensitive to stress due to lack of IGF2 secretion[93–95]. Mouse embryonic fibroblasts with hydrolytically inactive Grp94 mutants are unable to survive in serum-free media, indicating Grp94 ATPase activity is required for IGF2 chaperoning[96]. While evidence suggests secretion of insulin and IGF1 is also dependent on Grp94[94,97,98], the association between Grp94 and IGF2 is better characterized.

A common characteristic of peptide hormones, including insulin, is that their oligomerization promotes efficient sorting in the secretory pathway[99–102]. The E-peptide region of proIGF2 drives the formation of dynamic oligomers with minimal effect on proIGF2 folding[34]. This oligomerization could play a biological role in clustering proIGF2 for ER-to-Golgi transport. However, proIGF2 oligomerization complicates *in vitro* experiments needed to understand the chaperoning mechanism of BiP/Grp94. Given that all client-bound Hsp90 structures are of single clients bound to the chaperone, a monomeric proIGF2 construct is needed to test predictions from these structures in the context of BiP/Grp94. Chapter 3 discusses a new monomeric proIGF2 construct that I designed.

Figure 1.6 shows the range of topics about BiP/Grp94/proIGF2 that will be addressed in my thesis. Chapter 2 covers a novel electrostatic mechanism by which BiP differentiates oligomeric and monomeric states of certain clients. This project, which I worked on with a previous graduate student (Judy Kotler), is published. Chapter 3 examines questions raised from the loading complex structure in the BiP/Grp94 system, which ultimately led to the discovery of a third interaction interface between the BiP SBD and Grp94 CTD. Chapter 4 shows how the position of Phe138 explains why some ATP-competitive inhibitors are compatible with the C' state of Grp94 while others are not.

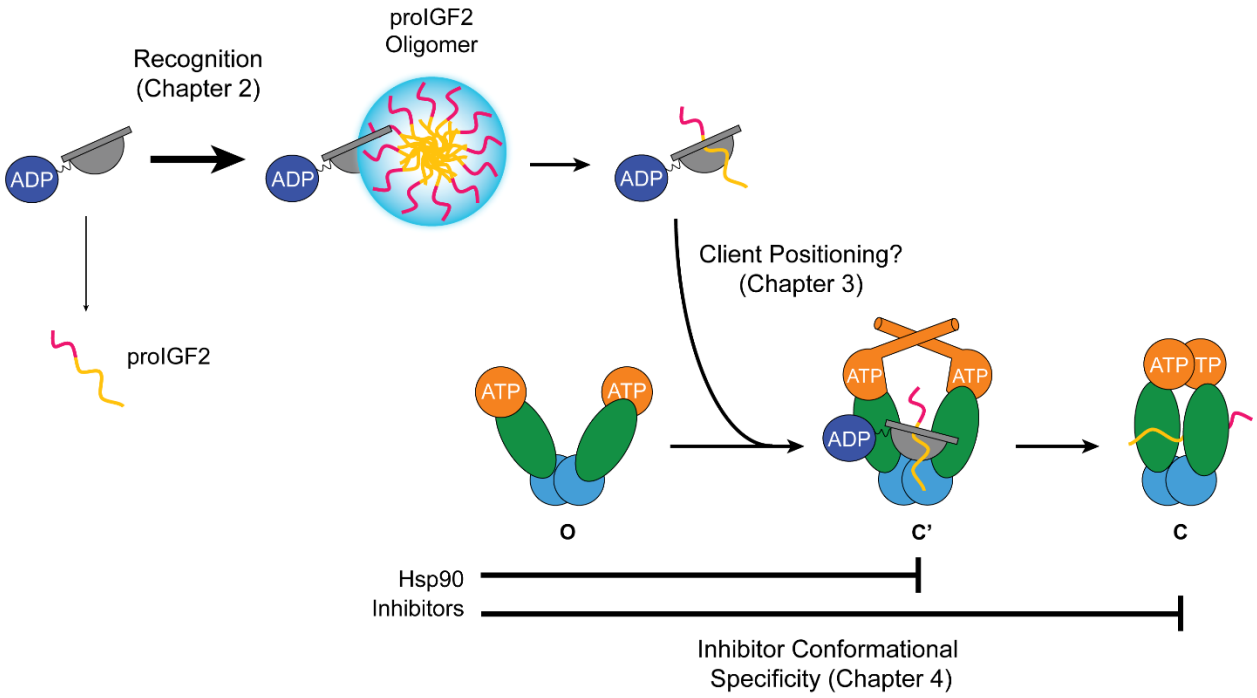

Figure 1.6. ProIGF2 is comprised of the IGF2 region (pink) and E-peptide region (yellow). Open (O), C', and closed (C) Grp94 conformations are labeled under the corresponding cartoon. Bold arrow indicates BiP's higher affinity for proIGF2 oligomers compared to monomers.

CHAPTER 2: Electrostatics Drive the Molecular Chaperone BiP to Preferentially Bind Oligomerized States of a Client Protein

PREFACE

This research was originally published in the Journal of Molecular Biology. Deans, E. E, Kotler, J. L. M., Wei, W. S., Street, T. O. Electrostatics Drive the Molecular Chaperone BiP to Preferentially Bind Oligomerized States of a Client Protein. Journal of Molecular Biology. 2022; 434: 167638.

AUTHOR CONTRIBUTIONS

J. L. M. K. and T. O. S. conceptualization; E. E. D., J. L. M. K., and W. S. W. investigation; E. E. D., J. L. M. K., W. S. W., and T. O. S. writing – original draft; E. E. D., J. L. M. K., and T. O. S. writing – review & editing; T. O. S. supervision; T. O. S. funding acquisition.

ACKNOWLEDGEMENTS

We thank Linda Hendershot, Daniel Oprian, and Tijana Ivanovic for helpful feedback on the results. Research for this project was supported by NIH R01 GM115356 and NSF-MRSEC-DMR-2011846.

2.1 Abstract

Hsp70 chaperones bind short monomeric peptides with a weak characteristic affinity in the low micromolar range, but can also bind some aggregates, fibrils, and amyloids, with low nanomolar affinity. While this differential affinity enables Hsp70 to preferentially target potentially toxic aggregates, it is unknown how a chaperone can differentiate between monomeric and aggregated states of a client protein and why preferential binding is only observed for some aggregated clients but not others. Here we examine the interaction of BiP (the Hsp70 paralog in the endoplasmic reticulum) with the client proIGF2, the pro-protein form of IGF2 that includes a long and mostly disordered E-peptide region that promotes proIGF2 oligomerization. By dissecting the mechanism by which BiP targets proIGF2 and E-peptide oligomers we discover that electrostatic attraction is a powerful driving force for oligomer recognition. We identify the specific BiP binding sites on proIGF2 and as monomers they bind BiP with characteristically weak affinity in the low micromolar range, but electrostatic attraction to E-peptide oligomers boosts the affinity to the low nanomolar level. The dominant role of electrostatics is manifested kinetically as a steering force that accelerates the binding of BiP to E-peptide oligomers by approximately two orders of magnitude as compared against monomeric peptides. Electrostatic targeting of Hsp70 provides an explanation for why preferential binding has been observed for some aggregated clients but not others, as all the currently-documented cases in which Hsp70 binds aggregates with high-affinity involve clients that have an opposite charge to Hsp70.

2.2 Introduction

Hsp70-family chaperones are crucial molecular machines involved in folding nascent polypeptides, holding non-native state protein folding intermediates, and disaggregating misfolded proteins[4,103]. They bind exposed, extended, and hydrophobic segments of unfolded, misfolded, or partially-folded proteins[104,105]. Hsp70s are composed of two domains held together by an interdomain linker: a nucleotide-binding domain (NBD) and substrate-binding domain (SBD) (Figure 2.1.A). The SBD contains a beta-sheet region (SBD_β), including the hydrophobic substrate-binding cleft, and an alpha helical lid (SBD_α). Hsp70s populate two major conformations that are dictated by the nucleotide bound in the NBD. In the ATP-bound conformation, the NBD and SBD_β are docked, the linker is bound to the NBD, and the SBD_α lid is open to expose the SBD_β substrate-binding cleft[20]. After ATP is hydrolyzed, the NBD and SBD_β undock, and the SBD_α lid closes onto the SBD_β substrate-binding cleft[21]. The ADP-bound conformation typically favors client binding, in which a client can be trapped between the SBD_β substrate-binding cleft and SBD_α lid[20]. BiP, like other Hsp70s, is negatively charged, much of which is contributed by the SBD (Figure 2.1.A).

A range of neurodegenerative diseases are associated with the formation of protein aggregates and fibrils, and it is important to understand how Hsp70-type chaperones differentiate whether the client protein is in an oligomeric or monomeric state. In some cases Hsp70s bind clients with much higher affinity when the client is oligomeric. For example, human Hsp70 binds tau fibrils with low nanomolar affinity and tau monomers with micromolar affinity[35]. In contrast, human Hsp70 binds α-synuclein fibrils and monomers with comparable low micromolar affinities[37]. Interestingly, while Hsp70 does not show a notable affinity difference for α-synuclein monomers versus fibrils, the Hsp70 co-chaperone DNAJB1 binds α-synuclein fibrils with ~100-

fold higher affinity than the monomers[37]. As discussed later, the seemingly disparate findings about preferential chaperone recognition of tau and α-synuclein fibrils can be rationalized by electrostatics, which we have found to be a dominant driving force that favors BiP binding proIGF2 and E-peptide oligomers.

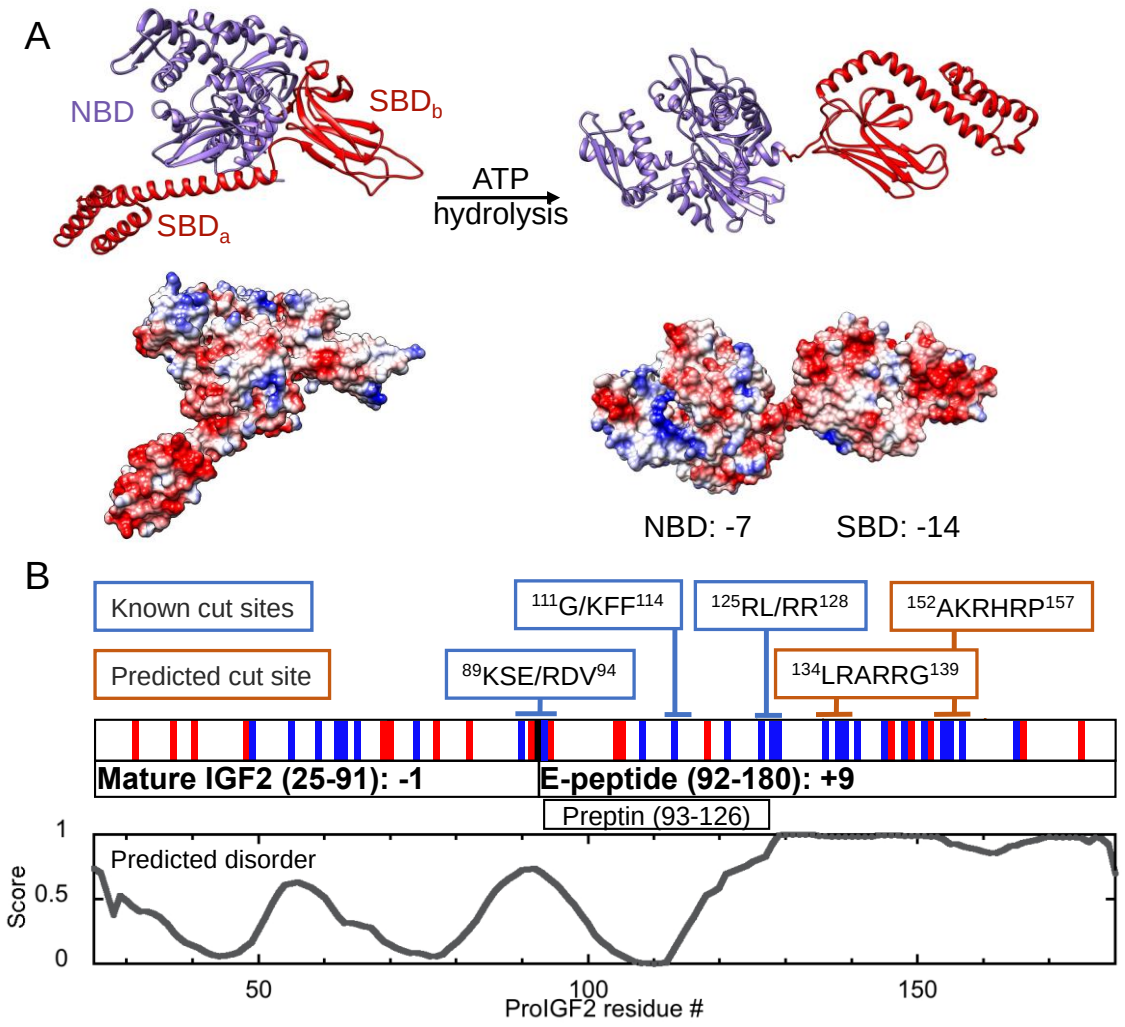

Figure 2.1. A. BiP's two major conformations are shown in ribbon and surface, with calculated electrostatic potential coloring (red for negative charge and blue for positive charge)[106]. BiP's ATP-bound conformation has NBD and SBD docked (PDB: 5E84), while BiP's ADP-bound conformation has the domains undocked (BiP homology model, PDB: 2KHO)[20,21]. The net charges of the NBD and SBD are noted below the ADP conformation. **B.** Known and predicted endoprotease processing sites on proIGF2. "/" indicates known cut site within sequence. Predicted sites are based on furin protease motif, "xBxBB/x", where x is an uncharged and B is a basic (Arg or Lys) amino acid[107]. Amino acid sequences shown in boxes are from *Mus musculus* proIGF2. Red and blue lines correspond to acidic (Asp and Glu) and basic (Lys and Arg) proIGF2 residues, respectively. Disorder for proIGF2 amino acid sequence was predicted by PONDR[108].

ProIGF2 is the pro-protein of insulin-like growth factor (IGF) 2, which is a member of the insulin family of hormones, and is a mitogen for fetal and placental cell growth[109]. ProIGF2 is targeted to the ER via an N-terminal (24 residue) ER-signaling sequence that is cleaved upon entrance to the ER. Following the signal sequence is the 67 residue mature hormone region and 89 residue positively-charged E-peptide (Figure 2.1.B). Folded, α-helical mature IGF2 contains three disulfide bonds, whereas the E-peptide is predicted to be mostly disordered and has minimal secondary structure[34]. Once folded, proIGF2 is translocated from the ER to the Golgi for further processing[91]. ProIGF2 is modified by N-acetylgalactosamine likely in the cis-Golgi, and sialic acid addition and oligosaccharide maturation in the trans-Golgi[91]. Modified proIGF2 is proteolytically cleaved twice by the proprotein convertase PC4: first to the intermediate form (residues 25-126) and then to mature IGF2 (25-91) (Figure 2.1.B)[110,111]. The second PC4 cleavage liberates the hormone preptin (93-126)[92]. Preptin, which has minimal structure[112], is cosecreted with insulin and amylin and increases glucose-mediated insulin secretion from pancreatic β-cells[113]. An intermediate cleavage product (25-111) has also been detected in bovine serum[114]. The positively-charged cleavage motifs confer a net charge of +9 to the E-peptide, while mature IGF2 has a net charge of -1.

Previous work demonstrated that proIGF2 forms dynamic oligomers, where the E-peptide region is necessary for oligomerization[34]. While the biological role of proIGF2 oligomerization is not known with certainty, many peptide hormones oligomerize to promote efficient trafficking through the secretory pathway and storage in granules[115]. BiP and the ER Hsp90 paralog Grp94 regulate the assembly of proIGF2 oligomers while exerting only a minimal influence on the folding of proIGF2[34]. It was left unknown where and how BiP and Grp94 interact with proIGF2. For example, whether BiP and Grp94 compete for binding sites on proIGF2 or whether they recognize

different areas, and how tightly these chaperones interact with proIGF2 oligomers. Here, by dissecting the mechanism by which BiP recognizes proIGF2 oligomers, we discover that electrostatics play a central role. Given the available data in the literature, electrostatics provide a plausible explanation of why Hsp70 chaperones preferentially bind some aggregated clients, such as tau, but not other clients such as α-synuclein.

2.3 Results

2.3.1. BiP Binds E-peptide Oligomers with High Affinity

We first utilized dynamic light scattering (DLS) to quantify the size of proIGF2 and E-peptide oligomers and the range of conditions in which oligomers are formed. ProIGF2 oligomers are larger than E-peptide oligomers and in both cases their size increases with protein concentration (Figure 2.2.A). In these experiments proIGF2 was maintained in a reduced and non-native state by the reducing agent TCEP. We only evaluated the size of proIGF2 oligomers at concentrations of 1μM and below, because at higher concentrations proIGF2 forms larger particles (Figure 2.2.B) that are beyond the range of accurate size determination by DLS. As a comparison, E-peptide oligomers and mature IGF2 scatter less light even at concentrations up to 5μM (Figure 2.2.B). For proIGF2, oligomerization is slower at pH 6 versus at pH 7.5 (Figure 2.2.C-D), so the first experiments were performed at this lower pH condition.

Because the hydrodynamic radius (R_H) of proIGF2 and E-peptide oligomers are in the range of hundreds of nanometers (Figure 2.2.A), much larger than BiP (R_H ~ 3nm[34]), we reasoned that the binding of BiP to these oligomers could be measured by fluorescence polarization (FP). Specifically, if BiP preferentially binds monomers or small oligomers then a negligible increase in polarization is expected, due to the small size of the proIGF2 monomer (17 kDa) relative to BiP

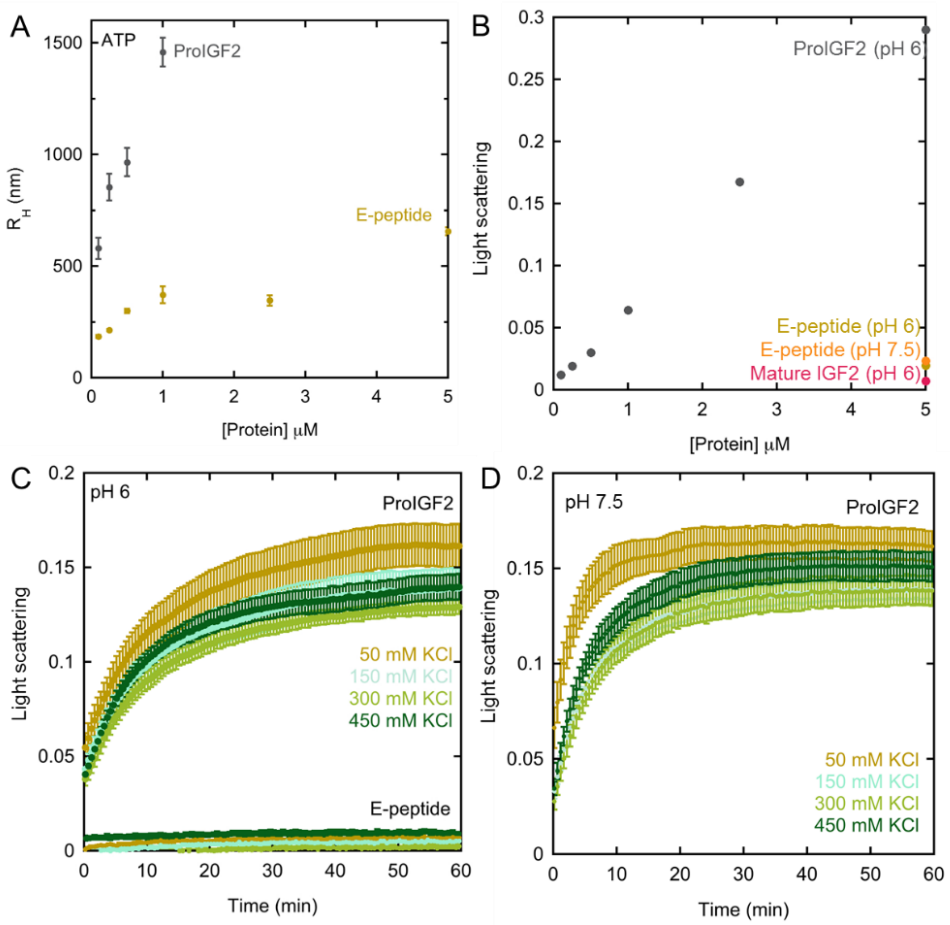

Figure 2.2. A. Mean hydrodynamic radius (R_H) of proIGF2 and E-peptide oligomers as measured by DLS. **B.** Concentration-dependent light-scattering (LS) data with proIGF2 shown with 5μM E-peptide and mature IGF2. **C.** LS data with 2μM proIGF2 and E-peptide at pH 6 and increasing salt concentrations. Rates of proIGF2 LS at pH 6 with increasing KCl are 0.072±0.001, 0.076±0.001, 0.080±0.003, and 0.091±0.001 min^{-1}. **D.** LS data with proIGF2 at pH 7.5 and increasing salt concentrations. Rates of proIGF2 LS at pH 7.5 with increasing KCl are 0.23±0.02, 0.12±0.01, 0.12± 0.01, and 0.14±0.01 min^{-1}. Light scattering data was collected at 320nm with a background subtraction of 700nm. Error bars indicate SEM for 3 replicates.

(70 kDa), whereas if BiP preferentially binds large oligomers then a large change in polarization is anticipated (Figure 2.3.A). Figure 2.3.B shows that BiP binds both proIGF2 and E-peptide oligomers, whereas no FP change is observed for mature IGF2. BiP binding to proIGF2 and E-peptide oligomers is observed under both ATP (Figure 2.3.B) and ADP (Figure 2.4) conditions. The larger amplitude of FP change for proIGF2 versus E-peptide is consistent with the larger size of proIGF2 oligomers measured by DLS. Also, in both cases the FP signal increases with protein concentration similar to the increasing size of E-peptide and proIGF2 oligomers as measured by

DLS. The isolated BiP NBD has only weak interactions with proIGF2 (Figure 2.4), indicating a minimal contribution from this region.

The above FP assay cannot yield a binding affinity because the FP signal is determined by the oligomer size, however, given that large FP changes are observed at sub-micromolar concentrations of proIGF2 and E-peptide, the FP data suggests sub-micromolar affinity. To determine BiP affinity for oligomers, we utilized a FRET assay measuring the conformation of BiP's SBD (Figure 2.3.C). This BiP_{SBD} FRET assay produces low FRET efficiency in the ATP-bound, lid-open state and high FRET efficiency in the ADP-bound and lid-closed state[116,117]. ProIGF2, E-peptide, and mature IGF2 were assayed with BiP_{SBD} FRET in the presence of ATP. BiP_{SBD} FRET increases upon binding proIGF2 and E-peptide oligomers, indicating lid closure (Figure 2.3.D). Lid closure has been observed when BiP binds a fully unfolded peptide region of a client[20] and indeed the E-peptide is intrinsically disordered and does not fold[34]. In contrast, large proteins that can fold have been found to maintain an open lid conformation[116,118]. No lid-closure is observed in the presence of mature IGF2. The FRET change for E-peptide can be fit with a binding curve (Figure 2.3.D, solid line) yielding an apparent binding affinity of ~100nM, approximately 100-fold higher affinity than is typical for BiP binding a monomeric peptide under ATP conditions. Because E-peptide oligomers form a distribution of different sizes, one needs to interpret the measured affinities as the effective binding of BiP to a distribution of oligomer sizes.

The BiP_{SBD} FRET assay is an indirect measure of client binding, and one potential confounding factor is BiP ATP hydrolysis influencing the conformation. The BiP ATPase rate indeed increases in the presence of the E-peptide (Figure 2.5.A), suggesting a contribution from ATP hydrolysis to the affinities measured by BiP_{SBD} FRET. To determine this contribution we utilized the BiP mutation T229A[20] which suppresses ATP hydrolysis both for BiP alone and in the

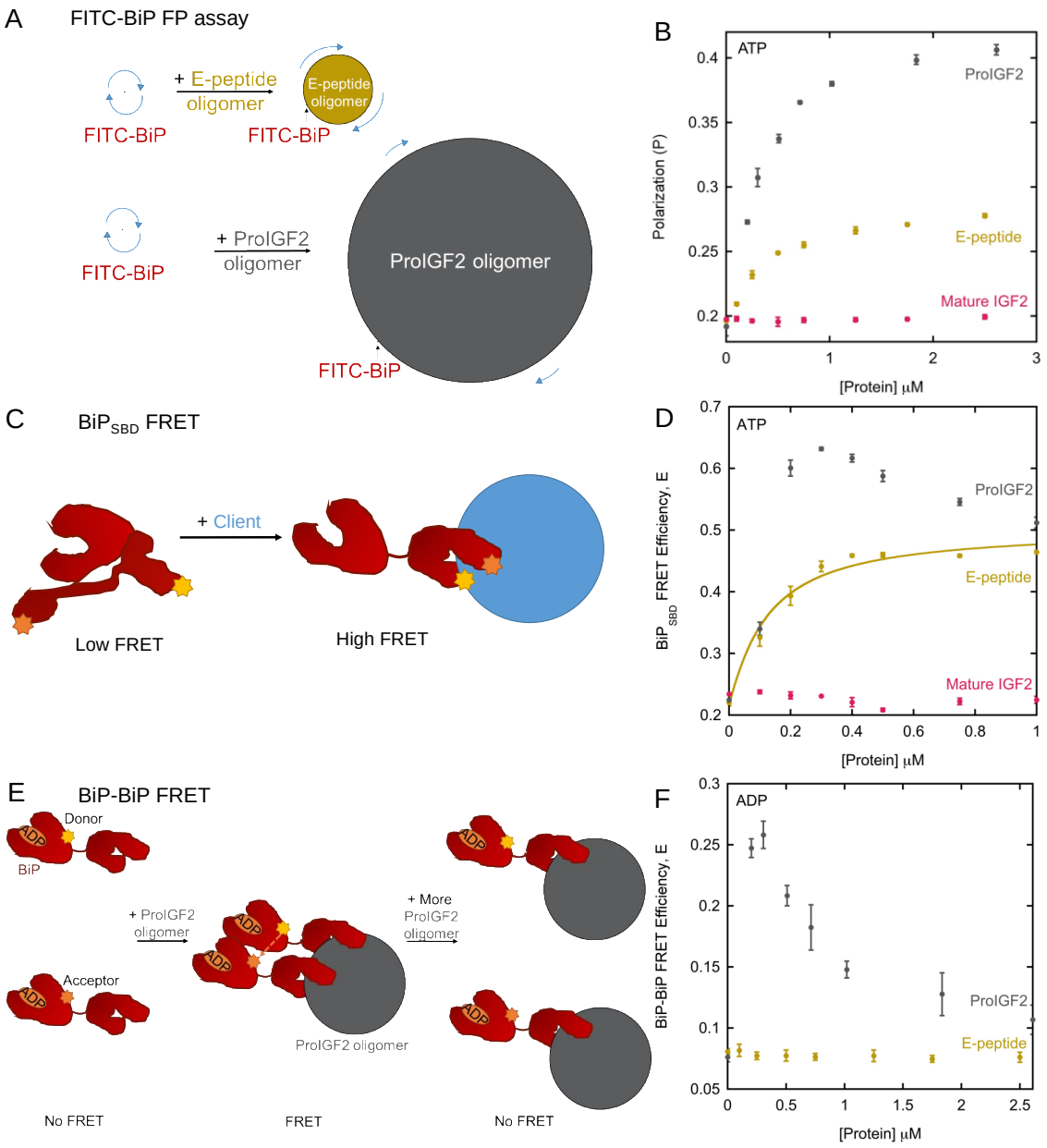

Figure 2.3. A. Schematic of FITC-BiP FP assay. The size of BiP is shown relative to the R_H values for E-peptide oligomers and proIGF2 oligomers when at a concentration of 1μM. Longer blue arrows indicate faster tumbling and shorter arrows indicate slower tumbling. **B.** FP data for FITC-BiP binding to proIGF2, E-peptide, and mature IGF2 in the presence of ATP. **C.** Schematic of BiP_{SBD} FRET where BiP's lid-open conformation produces low FRET efficiency (E) and BiP's lid-closed and client-bound conformation produces high FRET efficiency. Donor and acceptor labels can be present in both locations on the SBD due to labeling protocol, but only one of each is shown for clarity. BiP and oligomer sizes are not to scale. **D.** BiP_{SBD} FRET data for proIGF2, E-peptide and mature IGF2 in the presence of ATP. Solid line is a fit to Equation 4, with $K_D = 0.098 \pm 0.010$μM. **E.** Schematic of BiP-BiP FRET assay with BiP separately-labeled with either donor or acceptor fluorophore. BiP and oligomer sizes are not to scale. **F.** BiP-BiP FRET data for proIGF2 and E-peptide in the presence of ADP. Error bars are the SEM for three replicates.

presence of E-peptide (Figure 2.5.A). BiP_{SBD} FRET measurements with the T229A variant yield a 2.5-fold decrease in the measured affinity compared to wild-type (Figure 2.5.B) indicating that ATP hydrolysis by BiP makes only a modest contribution to the observed binding affinity of E-peptide oligomers. However, it should be noted that the T229A mutation may have additional influences on E-peptide oligomer binding to BiP beyond the reduction in ATPase activity. The measured binding affinity under ATP conditions should be interpreted as an effective binding constant with multiple contributing factors. The T229A mutation provides two additional insights. First it demonstrates that the E-peptide can drive BiP into the lid-closed conformation even in the absence of significant ATP hydrolysis. This behavior is expected because the lid-closed state has a higher client affinity than the lid-open state. Second, the results with T229A demonstrate that the observed high-affinity of BiP to E-peptide oligomers is not confounded by spurious ATP hydrolysis leading to a lid-closed conformation with no bound client.

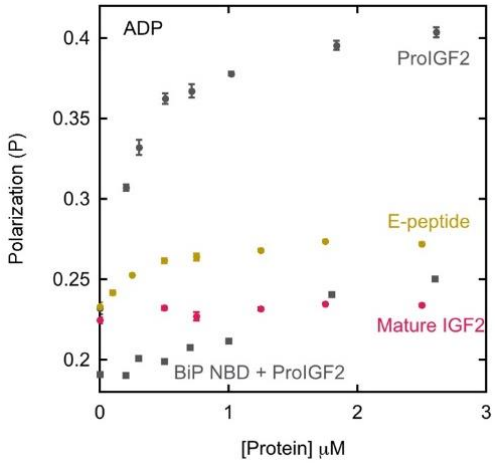

Figure 2.4. FP data with FITC-BiP and proIGF2, E-peptide and mature IGF2 (circles) and FITC-BiP NBD binding proIGF2 (squares) in ADP conditions. Error bars indicate SEM for 3 replicates.

We next sought to measure the affinity of BiP to E-peptide oligomers when BiP is in the lid-closed ADP conformation. Measuring BiP affinity under ADP conditions is challenging because BiP is maintained uniformly in the high-FRET lid-closed state, so no change in FRET

efficiency is observed (Figure 2.6). Therefore, we utilize a mixture of ADP and ATP to enable a change of FRET to be measured and balance the BiP equilibrium between the lid-open and lid-closed states. This should reduce the energetic cost of shifting the BiP conformational equilibrium and make the measured affinity more closely reflect the affinity in the lid-closed ADP conformation. Commercial stocks of ADP contain ~2% ATP (see Figure 1 in Liu et al.[119]), which we remove by a pretreatment with hexokinase (HK, see Methods). In experiments with this residual ATP present (termed "ADP, no HK") or with an additional 5% added ATP, we can measure BiP affinity to E-peptide oligomers under predominantly ADP conditions. In both cases, the measured BiP affinity to E-peptide oligomers is in the range of 10-20nM (Figure 2.6). The roughly ten-fold higher affinity of BiP for E-peptide oligomers under ADP versus ATP conditions is similar to the nucleotide dependence observed for other Hsp70s binding peptides[38,120]. Similar to ATP conditions, the measured binding affinity under ADP conditions should also be interpreted as an effective binding constant with multiple contributing factors. Nevertheless the apparent affinity for BiP to E-peptide oligomers is strikingly high and not characteristic of peptide binding affinities.

Unlike the BiP_{SBD} FRET data with E-peptide oligomers in Figure 2.3.D, which can be fit to a binding curve, for proIGF2 oligomers the FRET efficiency first rises above 0.5 and then falls back to a saturating value close to that observed for the E-peptide. Due to the fluorophore labeling scheme (Methods) the maximum FRET efficiency is 0.5 for a BiP monomer. However, if BiP monomers are positioned closely on an oligomer then FRET efficiencies above 0.5 could arise from an additional contribution from FRET between BiPs. We developed a FRET assay to detect when BiPs are in close proximity ("BiP-BiP FRET", Figure 2.3.E). BiP-BiP FRET reaches a maximum at 0.3μM proIGF2, indicating multiple BiP's are occupying a single proIGF2 oligomer,

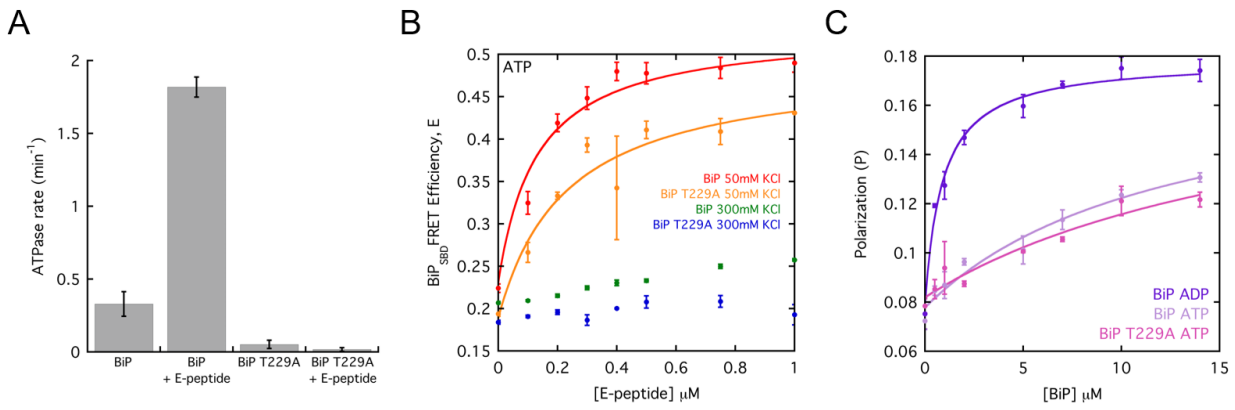

Figure 2.5. A. ATPase measurements for BiP T229A compared to wild-type with and without 2.5 μM E-peptide. **B.** Salt dependence of BiP T229A binding E-peptide oligomers as compared to wild-type (from Figure 2.3.D) as measured by the BiP_{SBD} FRET assay under ATP conditions. Solid lines are fit to equation 3. Apparent K_D value for BiP T229A is 0.25±0.06 μM, and for wild-type is 0.098±0.010 μM. **C.** FP assay with FITC-labeled site 1 binding BiP T229A compared to wild-type. Solid lines are a fit to equation 1. Under ATP conditions K_D of BiP T229A is 20±3 μM and K_D of wild-type is 13±2 μM (data same as Figure 2.8.A). All error bars are SEM of at least three replicates.

and higher concentrations of proIGF2 decrease FRET efficiency (Figure 2.3.F). At higher concentrations of proIGF2, with the same concentration of BiP, single BiPs will occupy different proIGF2 oligomers leading to the FRET efficiency decrease. BiP-BiP FRET is not observed in experiments with the E-peptide (Figure 2.3.F). The confounding effect of BiP-BiP FRET prevents the lid conformation from being known with confidence in experiments with proIGF2.

Overall, we conclude that the E-peptide is well-suited for studying BiP's high affinity binding to an oligomerized client. Unlike proIGF2, E-peptide oligomers are not confounded by BiP-BiP FRET, making the BiP_{SBD} FRET assay a powerful tool for measuring BiP affinity to oligomers. Furthermore, whereas proIGF2 experiments are performed at low pH to limit the formation of very large oligomers that strongly scatter light, E-peptide oligomers are well behaved at both low and high pH values (Figure 2.2.B) and BiP binds with comparable affinity at both pH 6.0 (K_D of 98±10 nM) and pH 7.5 (K_D of 130±10 nM) under ATP conditions.

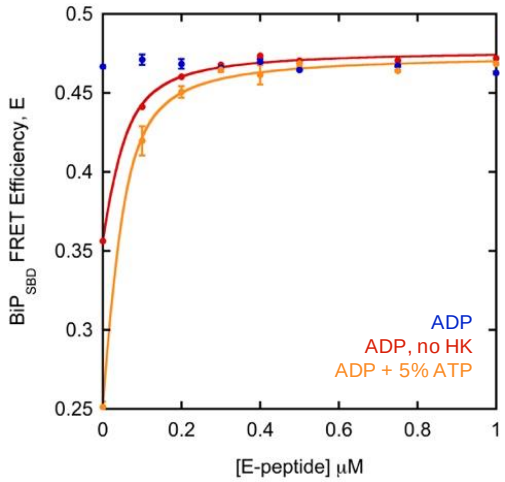

Figure 2.6. BiP_{SBD} FRET efficiency in the presence of E-peptide with HK-treated ADP (blue), ADP without an HK treatment (red, K_D = 15±5 nM) and ADP + 5% ATP (yellow, K_D = 19±4 nM). Solid lines are fit to equation 4. Error bars indicate SEM for at least 3 replicates.

2.3.2. Identification of BiP Binding Sites on ProIGF2

BiP binding sites can be predicted from primary sequence[121] and three potential sites are on the E-peptide (Figure 2.7.A, labeled 1, 2, and 3). Binding site 1 resides within the preptin region. All peptide constructs were labeled with FITC for FP measurements (Methods) and maintained at a low concentration (50nM) in BiP binding experiments to suppress oligomerization. Indeed, in the absence of BiP, sites 1-3 all have similar low polarization values of ~0.07 (Figure 2.8.A-C) that are characteristic of monomeric peptides.

BiP binds all three binding-site peptides and mature IGF2 with low micromolar affinity in the presence of ADP, and approximately 10-fold weaker affinity in the presence of ATP (Figure 2.7.B, Figure 2.8.A-D). Site 1 has the highest affinity for BiP (K_D ~ 1μM under ADP conditions), a much weaker binding than is observed for E-peptide oligomers (K_D ~ 10-20nM). While this difference in affinity could plausibly be explained if site 1 is not a complete BiP binding site, we confirmed that site 1 is complete by constructing E-peptide fragments centered at site 1, that are extended in the N-terminal direction (residues 92-120) and in the C-terminal direction (residues

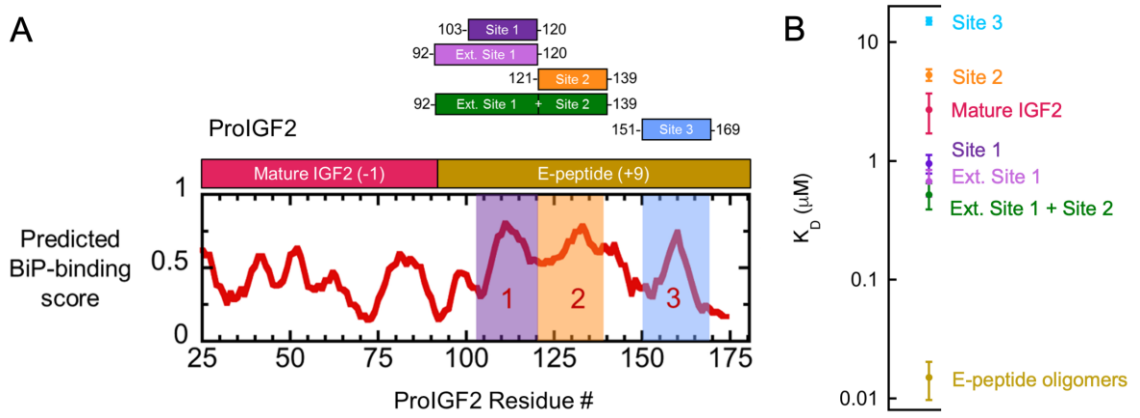

Figure 2.7. A. BiP-binding sites predicted by BiPPred[121]. Color shading indicates FITC-labeled peptide binding sites 1 (purple), 2 (orange), and 3 (blue). **B.** Affinities of monomeric E-peptide fragments (from Figure 2.8) and the oligomeric E-peptide (from Figure 2.6). Measurements performed under ADP conditions. Error bars are the SEM for at least three replicates.

92-139). Both "extended fragments" and site 1 bind BiP with similar affinity under ADP conditions (Figure 2.7.B, Figure 2.8.E-F). Because the 92-139 fragment contains both site 1 and site 2, we can exclude the possibility that the high affinity of BiP to E-peptide oligomers is due to an avidity effect from these two closely spaced BiP binding sites. This is consistent with the absence of BiP-BiP FRET on the E-peptide (Figure 2.3.F).

Site 1 can outcompete site 2 in binding to BiP under ADP conditions, with characteristically slow displacement kinetics (Figure 2.9.A). We conclude that both site 1 and site 2 bind within the BiP SBD cleft but site 1 is the dominant BiP binding region. The binding of site 1 to T229A BiP exhibits only a two-fold decrease in affinity under ATP conditions, indicating that ATP hydrolysis makes only a modest contribution to the binding of this peptide (Figure 2.5.C). We utilized the slow displacement kinetics of site 2 (Figure 2.9.A) to test whether BiP also binds E-peptide oligomers within the BiP SBD cleft. If BiP binds E-peptide oligomers within the BiP SBD cleft, BiP must first release site 2 before subsequently binding to the E-peptide oligomer, and the displacement kinetics should be slow. If BiP binds E-peptide oligomers outside the SBD cleft no such slow displacement will be observed. E-peptide oligomers show slow displacement

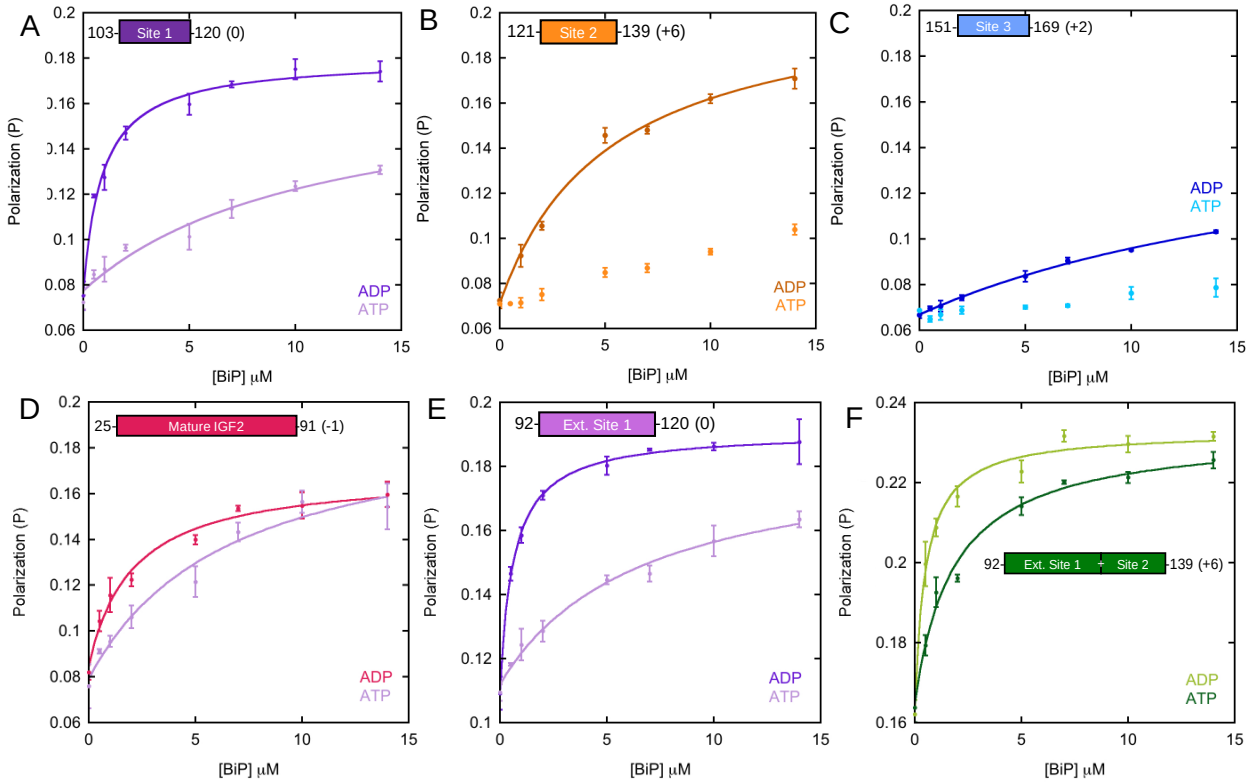

Figure 2.8. FP BiP binding assay with FITC-labeled E-peptide fragments. Solid lines indicate fit to equation 1, in cases where K_D values can be determined. **A.** BiP affinity for site 1 is: 0.95±0.17 μM and 13±2 μM, under ADP and ATP conditions respectively. K_D under ATP conditions is determined using same maximum amplitude as ADP condition. **B.** BiP affinity for site 2 is 5.3±0.6 μM under ADP conditions. **C.** BiP affinity for site 3 is 15±1 μM under ADP conditions. **D.** BiP affinity for $IGF2^{1\ Cys}$ is: 2.7±1.0 and 9.7±4.5 μM, under ADP and ATP conditions respectively. **E.** BiP affinity for extended site 1 is: 0.67±0.17 μM and 8.0±3.8 μM, under ADP and ATP conditions respectively. **F.** BiP affinity for extended site 1&2 is: 0.52±0.13 μM and 1.9±0.6 μM, under ADP and ATP conditions respectively. All error bars indicate SEM for three replicates.

kinetics that are similar to that of site 1 (Figure 2.9.B) indicating that BiP binds E-peptide oligomers within the SBD cleft in a manner similar to site 1.

Grp94 has minimal binding for sites 1-3 and mature IGF2 under both ATP and ADP conditions (Figure 2.10), demonstrating that these sites are specific to BiP. Interestingly, site 1 binds non-specifically to BSA whereas sites 2&3 do not bind BSA (Figure 2.11), suggesting that BiP's preferential binding to site 1 may serve a biological role in preventing non-specific interactions with this region.

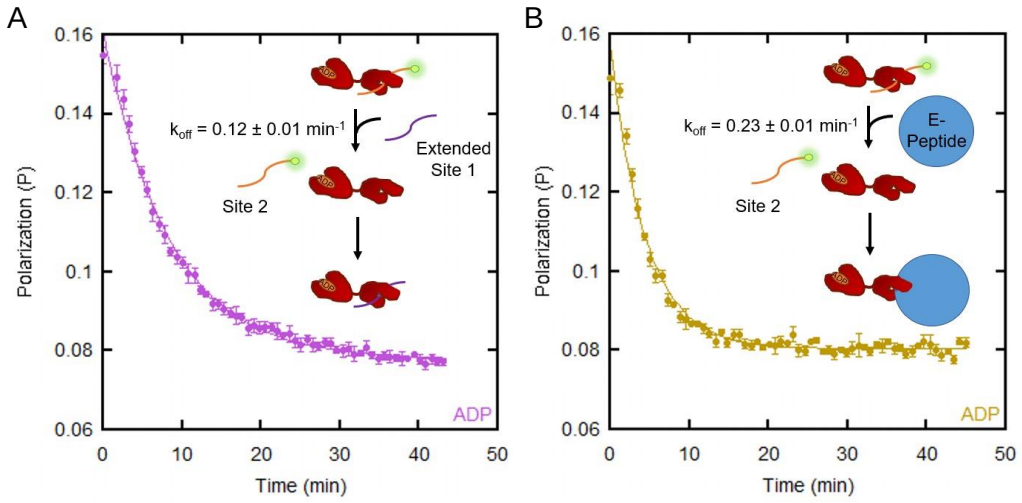

Figure 2.9. Binding competition experiments. 50nM FITC-labeled site 2 was prebound to 5.3μM BiP under ADP conditions. **A.** Competition with 10μM of extended site 1. **B.** Competition with 5.3μM of oligomerized E-peptide. Solid lines are a fit to an exponential decay. Error bars are the SEM for three replicates.

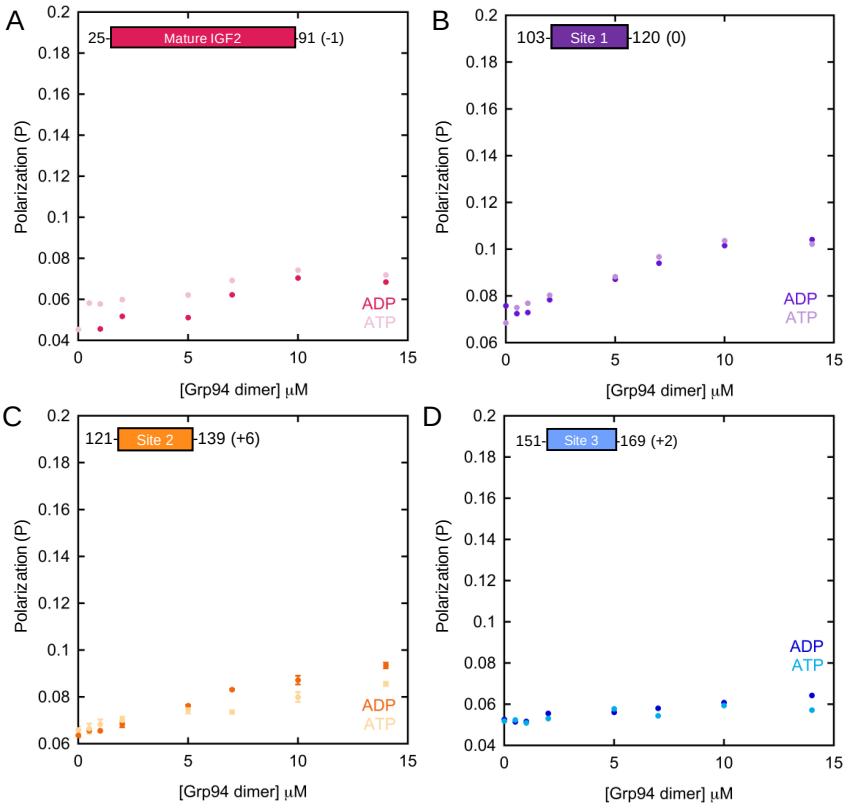

Figure 2.10. FP assay with FITC-labeled peptides and mature IGF2 (1 cysteine mutant) in the presence of Grp94 and ADP or ATP. Error bars indicate SEM for 3 replicates, where present. Y-axis is identical to Figure 2.8 for comparison against results with BiP.

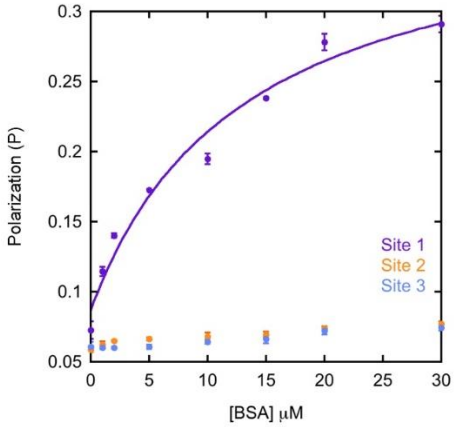

Figure 2.11. FP assay with FITC-labeled site 1, 2, or 3 binding BSA. Solid line indicates fit to equation 1 (K_D: 13±2 μM). Error bars indicate SEM of 3 trials.

2.3.3. Electrostatic Steering Enhances BiP Affinity for E-peptide Oligomers

The charge difference between BiP and both proIGF2 and the E-peptide (Figure 2.1) suggests that high affinity binding might have an electrostatic contribution. If true, BiP affinity for proIGF2 and E-peptide oligomers should be salt dependent due to charge screening. The affinity of BiP for E-peptide oligomers as measured by BiP_{SBD} FRET is indeed highly salt dependent, where increasing the salt concentration weakens BiP's affinity for E-peptide oligomers under both ADP and ATP conditions (Figure 2.12.A, Figure 2.13.A-B). In the presence of ATP, fitting the highest salt concentration data requires fixing the saturating FRET efficiency value and therefore these K_D values are not as well defined and should be interpreted cautiously (these data are marked with an asterisk in Figure 2.12.A). While salt-dependent affinities cannot be measured for BiP and proIGF2 because of BiP-BiP FRET (Figure 2.3.F), the FP assay described in Figure 2.3.A shows a loss of binding between BiP and proIGF2 oligomers with increasing salt (Figure 2.13.C).

The strong salt dependence of BiP binding E-peptide oligomers is observed with different salts (KCl, NaCl and KI, Table 2.1), as expected for electrostatic screening rather than a specific ionic interaction. ProIGF2 and E-peptide light scattering is minimally salt-dependent (Figure

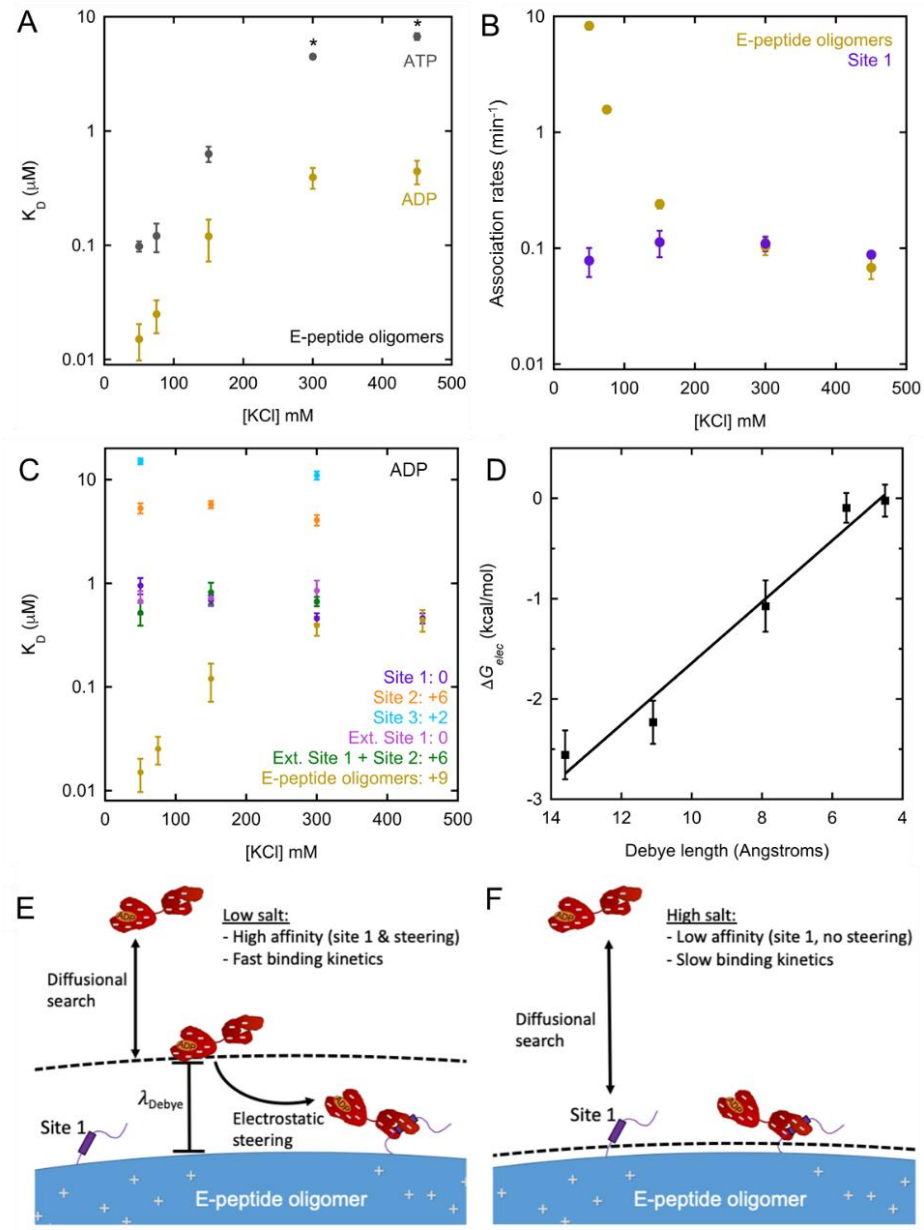

Figure 2.12. A. Salt-dependent affinity measurements for BiP binding E-peptide as measured by BiP_{SBD} FRET in the presence of ADP or ATP. Individual binding curves shown in Figure 2.13.A-B. Asterisks indicate lower confidence of fitting. **B.** Salt-dependent association rates for BiP and 0.1μM E-peptide as measured by BiP_{SBD} FRET under ADP conditions. Association rates for site 1 and 0.1μM BiP was determined by FP (Methods). **C.** BiP affinities for E-peptide fragments and the oligomeric E-peptide in the presence of ADP. The E-peptide oligomer data is the same as in Figure 2.12.A. Individual binding curves for the peptide fragments are shown in Figure 2.14. Net charge of each fragment is indicated next to name. **D.** Electrostatic contribution to BiP's binding of E-peptide oligomers, as calculated by ΔG°_{elec}= -RTln($K_{D,site\ 1}/K_{D,E\text{-}peptide\ oligomers}$), versus the Debye length, in the presence of ADP. Error bars in panel D are the propagated uncertainty from panel C, all other error bars are the SEM for at least three replicates. The $K_{D,site\ 1}$ value at 50mM KCl is used to calculate ΔG°_{elec} at both 50 and 75mM KCl. Line indicates linear fit (ΔG°_{elec} intercept: 1.4±0.3 kcal/mol and slope: -0.31±0.03 kcal/mol*Å). **E-F.** Schematic model of BiP binding E-peptide oligomers at low **(E)** and high salt **(F)**.

2.2.C-D), suggesting that oligomer size changes cannot explain the strong salt-dependent binding of BiP to both proIGF2 and E-peptide. The strong salt-dependent affinity of BiP for E-peptide oligomers is equally evident for the ATPase-inactive T229A variant (Figure 2.5.B), indicating that the strong salt-dependence of BiP binding E-peptide oligomers cannot be attributed to salt-dependent changes in BiP ATPase activity.

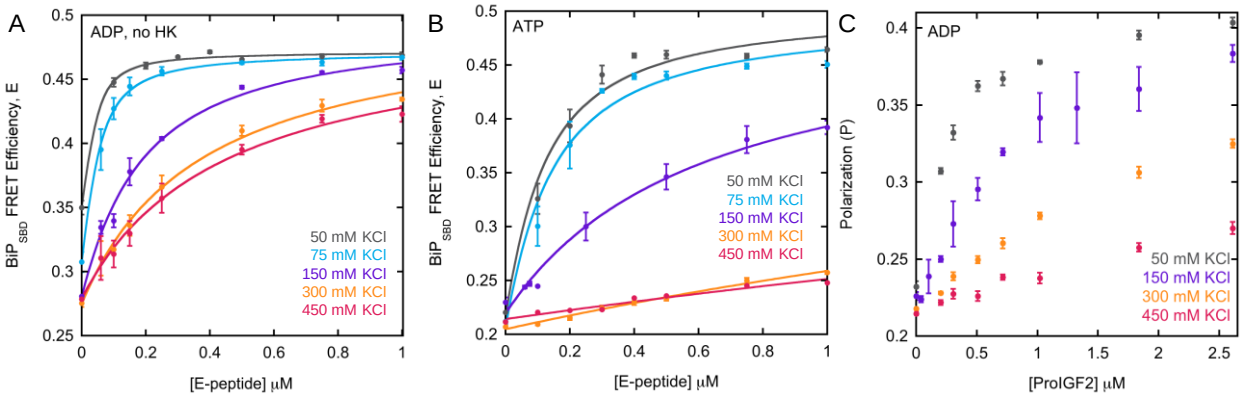

Figure 2.13. A. Salt-dependence of BiP_{SBD} FRET assay with E-peptide oligomers and non-HK treated ADP. Fit values of binding affinities are shown in Figure 2.12.A. Solid lines for 50, 75, and 150mM KCl are a fit to equation 4, and lines for 300 and 450mM KCl are a fit to equation 3. **B.** Salt-dependence of the BiP_{SBD} FRET assay with E-peptide oligomers under ATP conditions. Fit values of binding affinities are shown in Figure 2.12.A. Solid lines for 50 and 75mM KCl are a fit with equation 4, and 150, 300, and 450mM KCl data are fit with equation 3 and a maximum FRET efficiency set to 0.5. K_D data from 300 and 450 mM KCl have a lower confidence of fitting. **C.** BiP binding proIGF2 oligomers as a function of increasing KCl concentration using FP assay with FITC-labeled BiP, in the presence of ADP. Error bars indicate the SEM for at least 3 replicates.

Given the dramatic influence of salt on the affinity of BiP to E-peptide oligomers, we questioned whether electrostatic steering, which is characterized by salt-dependent association rates leading to salt-dependent binding affinities, is the underlying cause. At low salt, BiP binding is indeed accelerated and we performed the measurements at 10°C to slow the rates such that they can be accurately quantified. Figure 2.12.B shows salt-dependent association rates between BiP and E-peptide in which association kinetics decrease by ~100-fold between 50 to 450mM KCl, whereas BiP binds the site 1 peptide with no notable salt-dependence. Collectively, the above results indicate that electrostatic steering enhances BiP affinity for proIGF2 and E-peptide

oligomers. One final feature to note is that the binding rates of BiP to site 1 and to E-peptide oligomers converges at high salt. As discussed next, a similar convergence is observed in the context of BiP's binding affinity to E-peptide oligomers.

2.3.4. Two Energetic Contributions to BiP Binding to E-peptide Oligomers

BiP binds sites 1-3 with minimal salt-dependence (Figure 2.12.C, Figure 2.14.A-C), even though binding sites 2 and 3 are positively charged. This lack of salt dependence is also observed for the extended fragments centered at site 1 (residues 92-120 and 92-139, Figure 2.14.D-E), although modest salt-dependent changes are observed in the FP amplitude. Because BiP exhibits a minimal salt-dependence for binding sites 1-3, we conclude that the strong salt-dependence is unique to BiP binding E-peptide oligomers.

Importantly, BiP's affinity for E-peptide oligomers at high salt matches that of all the peptide fragments that include site 1 (Figure 2.12.C). This is consistent with a model in which two energetic contributions enable BiP to bind the E-peptide oligomers with high affinity. The first contribution is from BiP binding site 1, and the second contribution is from the electrostatic attraction between BiP and the E-peptide oligomer. When the electrostatic contribution is screened by increasing the salt concentration, BiP's affinity for E-peptide oligomers converges to the affinities of all peptide constructs that contain site 1 (see 450mM KCl data in Figure 2.12.C). However, we note that the affinities measured by FP and SBD FRET are not necessarily expected to be identical because the SBD FRET assay produces an apparent binding affinity due to the multiple contributing factors, as discussed earlier.

The data in Figure 2.12.C enables the electrostatic contribution to binding to be determined at any salt concentration. For example, under ADP conditions and at 50mM KCl BiP binds E-

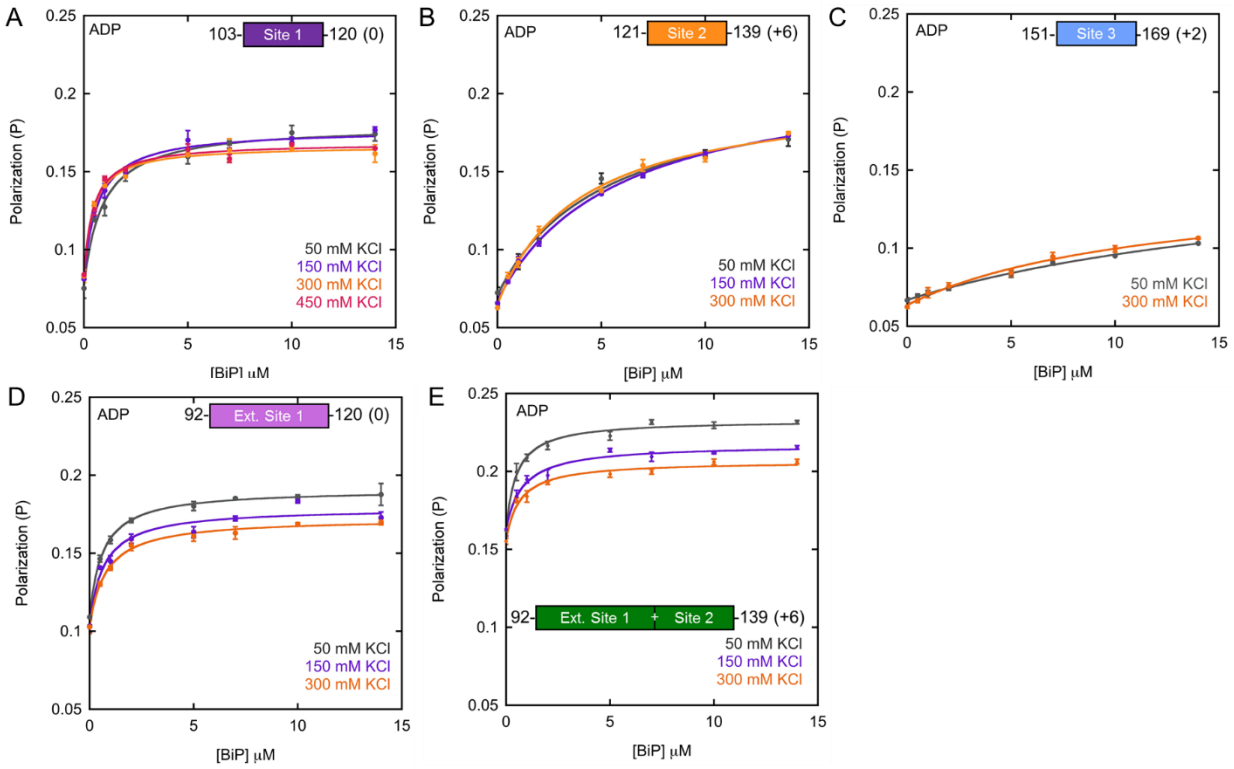

Figure 2.14. FP salt-dependence data in the presence of ADP for BiP binding fluorescently-labeled E-peptide fragments **(A)** site 1, **(B)** site 2, **(C)** site 3, **(D)** extended site 1, and **(E)** extended site 1 + site 2. Error bars indicate SEM for at least 3 trials. Data shown in **(B)** and **(C)** were completed in the presence of BSA.

peptide oligomers with ~60-fold higher affinity than to site 1 (K_D = 0.015±0.005 µM compared to K_D = 0.95±0.17 µM). A similar analysis under ATP conditions shows that electrostatic attraction provides a ~130-fold enhancement of affinity of BiP to E-peptide oligomers at 50mM KCl (Figure 2.15). While the influence of salt has a dramatic influence on BiP binding oligomers, only minor effects are observed for BiP binding the monomeric site 1 peptide. For example, increasing salt provides a slight enhancement of site 1 binding under ADP conditions (K_D of 0.95±0.17 µM at 50mM KCl versus 0.46±0.05 µM at 450mM KCl), and no notable salt-dependent affinity changes are observed under ATP conditions (Figure 2.15).

Theoretical predictions (see Chapter 9 in Physical Biology Of The Cell[122]) and experiments on viral capsids[123] provide a framework for understanding the quantitative influence of salt on

electrostatic screening around large macromolecular assemblies such as E-peptide oligomers. In particular, the free energy contribution of electrostatics should vary linearly with the Debye length (λ_D, the characteristic distance over which electrostatic interactions are screened). Higher salt decreases λ_D, for example at 50mM KCl λ_D is ~14Å which decreases to ~4Å at 450mM KCl. Figure 2.12.D shows the electrostatic contribution to BiP's binding to E-peptide oligomers versus λ_D, which indeed exhibits the predicted linear relationship. While other factors may also contribute to the binding of BiP to E-peptide oligomers, our data is consistent with a model in which two energetic factors predominate (Figure 2.12.E-F). The first is the hydrophobic interaction between BiP and site 1 within the SBD cleft, which has the characteristic affinity of ~1μM and minimal salt dependence. The second is the electrostatic contribution that causes electrostatic steering of BiP to E-peptide oligomers. The capture distance at which BiP experiences electrostatic steering depends on λ_D which in turn depends on the salt concentration.

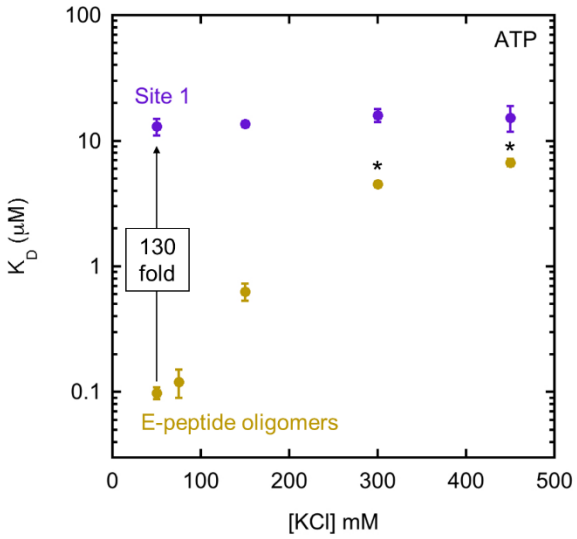

Figure 2.15. Influence of salt on BiP's affinities for E-peptide oligomers and site 1 under ATP conditions. K_D data for site 1 measured by FP. K_D data for E-peptide is measured by BiP_{SBD} FRET and is same as Figure 2.12.A and Figure 2.13.B. Error bars are the SEM for at least three replicates. Asterisks indicate lower confidence of fitting, as described in Figure 2.13.B.

2.3.5. Enhanced Binding of BiP to E-peptide Oligomers is Driven by Widely Dispersed Charges Across the E-peptide Sequence

E-peptide oligomers provide a favorable electrostatic contribution for BiP binding despite the fact that the primary binding site on the E-peptide (site 1) has no net-charge. This indicates that charges distal from site 1 are responsible for the enhanced affinity, but it is not clear whether a specific group of charges are responsible or whether the collective charges across the E-peptide all contribute. Recall that the E-peptide has clusters of positively charged residues at conserved endoprotease cut sites (Figure 2.1.B). Therefore, we designed a series of truncations to successively remove each of these +3 charge clusters to determine whether a single charge cluster dominates or whether each cluster contributes equally (Figure 2.16.A). In these experiments BiP is maintained at a low concentration, and the E-peptide constructs are titrated to enable

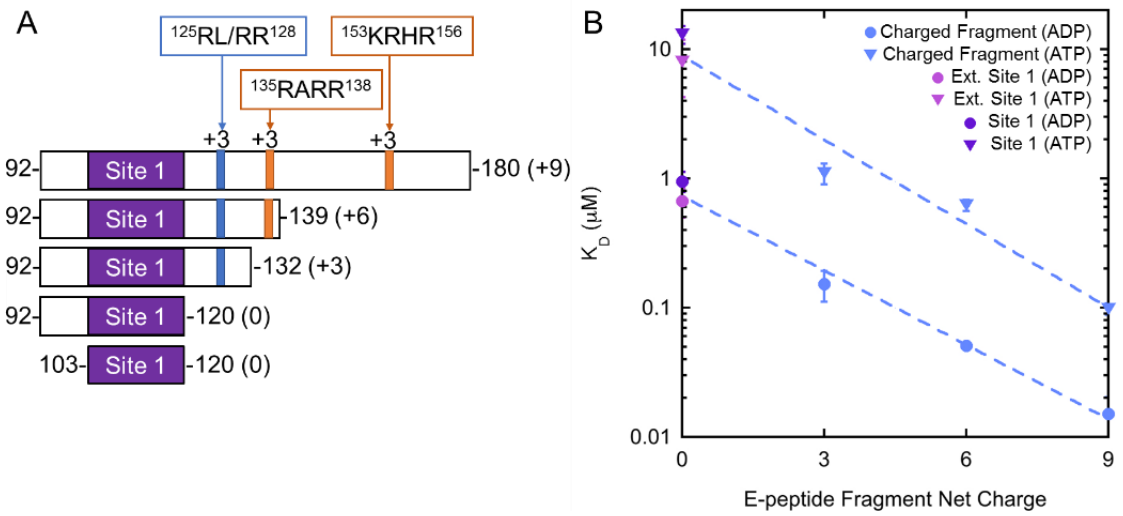

Figure 2.16. A. E-peptide and E-peptide truncations where net charge and endoprotease cut sites are indicated for each construct. **B.** BiP's K_D for each E-peptide fragment listed in panel A, versus the fragment's net charge. K_D data is from BiP_{SBD} FRET, except for Ext. Site 1 and Site 1 which are from FP data. Error bars indicate SEM for 3 replicates, and error bars may be smaller than data point. Dashed lines indicate a logarithmic fit (K_D intercepts: 0.73±0.10 μM (ADP); 8.9±2.6 μM (ATP)). Slopes are: $10^{-(0.19 \pm 0.01)x}$ (ADP); $10^{-(0.22 \pm 0.03)x}$ (ATP), where *x* is the net charge of the E-peptide fragment and the uncertainty is from the fitting error. Individual binding curves for charged fragments are shown in Figures 2.8, 2.13 and 2.17.

oligomerization. Figure 2.16.B shows a progressive enhancement of BiP affinity for E-peptide constructs with progressively positive net charge. This trend (dashed lines, Figure 2.16.B) shows a convergence of the high affinity binding of BiP to E-peptide oligomers to the low affinity site 1 binding as the net charge on E-peptide constructs is reduced. This convergence is conceptually similar to the convergence in oligomer and site 1 affinities with increasing salt (Figure 2.12.C).

As one final control, we constructed full-length E-peptide variants in which the three charge-clusters are progressively mutated to alanine residues (Figure 2.18.A). Similar to the truncation variants discussed above, the charge reduction variants of full-length E-peptide show a progressive loss of affinity for BiP as measured by SBD FRET (Figure 2.18.B). Decreasing the E-peptide net charge did not notably change the oligomer size (all constructs had R_H values in the range of 100-200nm as measured by DLS when at 500nM). We conclude that the electrostatic driving force that enhances BiP binding to E-peptide oligomers is from charges that are widely dispersed across the E-peptide sequence.

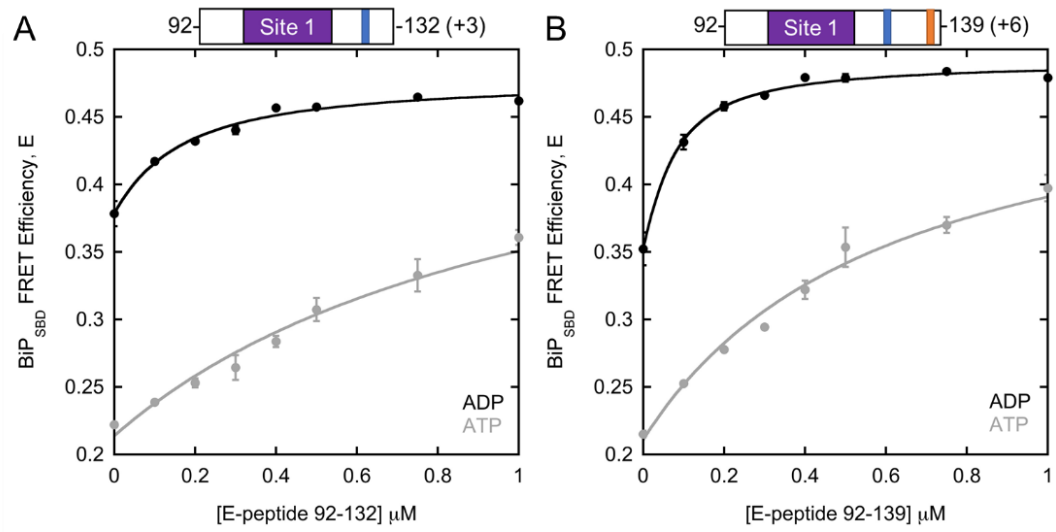

Figure 2.17. E-peptide fragments with +3 charge **(A)** and +6 charge **(B)** binding to BiP as measured with the BiP_{SBD} FRET assay in the presence of ADP or ATP. Error bars indicate SEM of 3 trials and may be smaller than data points themselves. ADP data was fit to Equation 4, and ATP data was fit to Equation 3 with a maximum FRET efficiency set to 0.5.

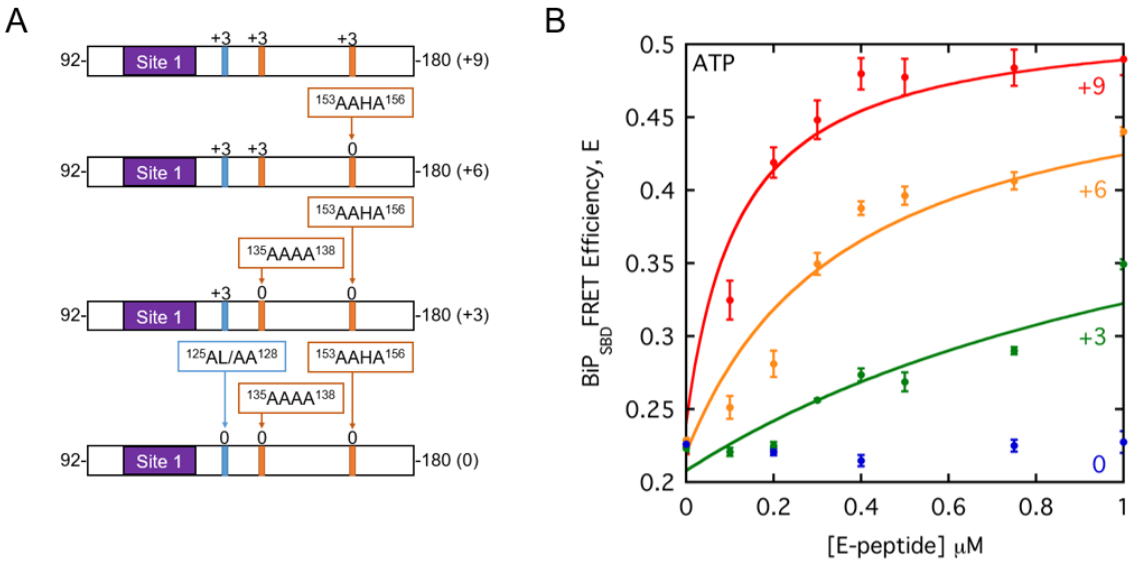

Figure 2.18. A. E-peptide and reduced charge E-peptide mutants. Net charge is indicated for each construct. Endoprotease cut sites and corresponding net charge reducing mutations are shown in blue and orange, as in Figure 2.1.B. **B.** BiP binding to E-peptide and reduced charge variants as measured by BiP_{SBD} FRET under ATP conditions. Data and fit for +9 E-peptide is the same as Figure 2.3.D. Solid lines for the +6 and +3 charge E-peptide variants are a fit to Equation 3 with a maximum FRET efficiency set to 0.5. Apparent K_D values for BiP binding the +6 and +3 E-peptide variants are 0.35 ± 0.01μM and 1.44 ± 0.04μM, respectively. All error bars are SEM of three replicates.

2.4 Discussion

The action of Hsp70-type chaperones on aggregates, oligomers, and fibrils is a crucial aspect of cellular homeostasis, the adaptive response to environmental stress, and the progression of age-related diseases[124]. However, heterogeneity of aggregates, oligomers, and fibrils imposes technical challenges in determining how Hsp70s recognize oligomeric client states versus the monomeric peptide fragments that are often used as model systems to study Hsp70:client binding. Here, by dissecting the mechanism by which BiP recognizes proIGF2 and E-peptide oligomers, we discover that electrostatic attraction is a powerful driving force that drives BiP to preferentially bind oligomeric client states. BiP binds E-peptide oligomers with nanomolar apparent affinity, but binds the monomeric constituent peptides with micromolar affinity. In this regard, BiP interacts very differently with proIGF2 oligomers compared to the well-studied C_H1 domain in which BiP

binds full-length C_H1 (K_D of 4.2μM) with similar affinity to its constituent peptide motif (K_D of 12μM)[116,125]. The predominant BiP binding site on proIGF2 is located at the preptin hormone region of the E-peptide (site 1, Figure 2.7.A), a region that does not fold[126]. This again contrasts with the BiP recognition of C_H1, in which the BiP binding site is buried after C_H1 folds and forms a disulfide-linked complex with C_L[125]. One final difference is that binding of BiP to E-peptide oligomers drives BiP into the lid-closed state, whereas the binding of C_H1 to BiP does not produce lid-closure[116].

A strong electrostatic driving force causes BiP to preferentially bind oligomers. This is evident in the salt-dependent association rate of BiP binding E-peptide oligomers but not for the monomeric site 1 fragment (Figure 2.12.B). Such salt-dependent association kinetics are characteristic of electrostatic steering between large highly charged complexes, as with the positively charged multimeric Von Willebrand factor binding its negatively charged receptor glycoprotein Ibα[127]. In this case, the association kinetics span approximately two orders of magnitude between 80 to 500mM salt[127], a similar magnitude as what we observe for BiP binding E-peptide oligomers (Figure 2.12.B). Similar to the binding kinetics, salt-dependent affinity is observed for BiP binding E-peptide oligomers but not to the constituent monomeric peptides (Figure 2.12.C). The energetic contribution from electrostatics varies linearly with the Debye length (Figure 2.12.D) as predicted theoretically[122]. The electrostatic affinity enhancement, spanning approximately two orders of magnitude is a collective property of the E-peptide net charge rather from a distinct set of charges (Figure 2.16.B, Figure 2.18).

The electrostatic explanation for BiP's high affinity for oligomers provides an explanation for why other Hsp70s recognize specific aggregated client proteins with high affinity. Figure 2.19 is a compilation of previously measured Hsp70 affinities for monomeric and aggregated clients,

evaluated by the predicted net charge of the client (data and references are in Table 2.2). Hsp70s bind peptides with a maximal affinity of ~1μM. Even engineered peptides that are designed to have high affinity for Hsp70, such as the Javelin sequence, only reach ~1μM[128]. A similar upper limit appears to apply to Hsp70 binding negatively charged clients such as α-synuclein (net charge of -9) for both monomers and fibrils (K_D ~10μM)[37].

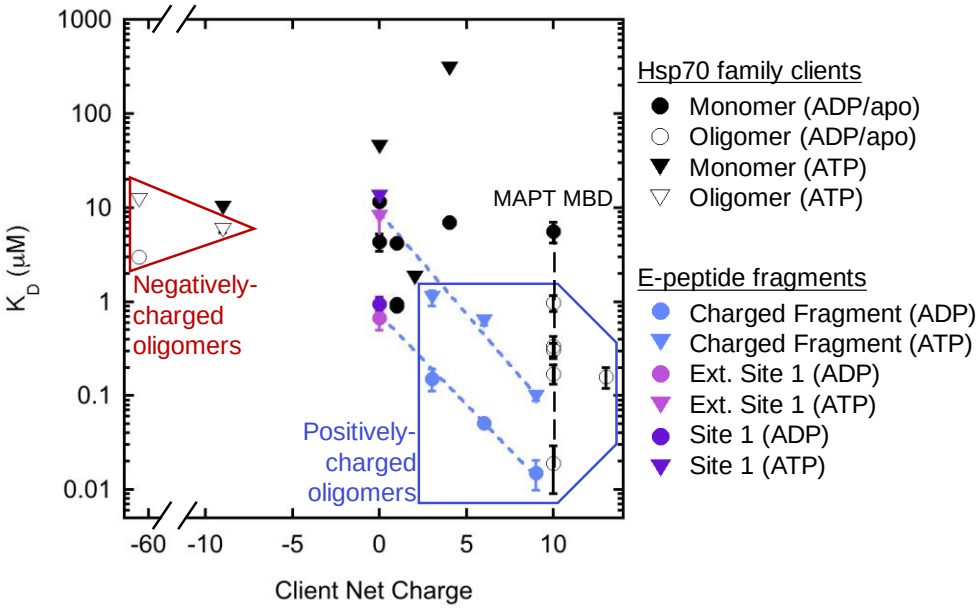

Figure 2.19. Compilation of Hsp70 and BiP affinities for monomeric and oligomeric clients, sorted by net charge. See Table 2.2 for data and references. Black dashed line indicates MAPT MBD K_D values with increasing size (1-2mer to fibril[35]). K_D data for E-peptide, E-peptide truncations, and associated blue dashed lines are from Figure 2.16.

To our knowledge the only reported instances of metazoan Hsp70s binding with much higher affinity than ~1μM is in the case of aggregates of positively charged clients. For example, the binding of cytosolic Hsp70 (net charge -11) to MAPT MBD (net charge +10) is directly proportional to the oligomer size, with larger oligomers yielding higher affinities (Figure 2.19, black dashed line). Hsp70 binds MAPT MBD fibrils with ~10nM affinity[35], a value comparable to BiP affinity to E-peptide oligomers. A fast association rate is observed between Hsp70 and MAPT MBD[35] suggesting that electrostatic steering is at work, similar to our findings with BiP

and E-peptide oligomers (Figure 2.12.B). The affinity of BiP to E-peptide oligomers, as well as E-peptide truncations with different net charges (blue diagonal dashed lines, Figure 2.19) all fall within the range of values measured for other positively charged clients. Finally, electrostatics provides an explanation for why Hsp70 binds the negatively charged α-synuclein fibrils with similar affinity to α-synuclein monomers, whereas the positively charged DNAJB1 binds α-synuclein fibrils with ~100-fold higher affinity compared to the monomers[37].

The data in Figure 2.19 is restricted to metazoan Hsp70s, however experiments with the bacterial Hsp70 homolog DnaK (net charge -30) suggest that this mechanism also applies. Specifically, DnaK has been reported to bind positively charged IAPP oligomers in the pM-range[129]. However, the affinity of DnaK for oligomers may not be directly comparable to metazoan Hsp70 data in Figure 2.19, because DnaK can bind monomeric peptides with substantially higher affinity than is observed for metazoan Hsp70s (Table 2.3).

The hypothesis that electrostatics target Hsp70s to positively charged oligomeric clients, provides predictions for future experiments. For example, the MAPT 3R and 4R isoforms, which also have a positive net charge, exhibit high affinity binding to Hsp70 (Table 2.2) but their oligomerization state has not been determined[130]. The electrostatic explanation predicts that MAPT 3R and 4R isoforms should be oligomeric. In the case of IGF proteins, electrostatics should favor the binding of BiP to oligomeric states of proIGF1 (net charge +18), but not proinsulin (net charge -3). One additional area for future investigation is to determine the role of oligomer size heterogeneity on BiP affinity. While Hsp70 affinity for the MAPT MBD is proportional to the oligomer size (Figure 2.19, black dashed line) more detailed measurements are needed to determine if a similar relationship holds for BiP binding to E-peptide and proIGF2 oligomers.

The preferential binding of BiP for oligomeric clients has implications for how the ER responds to stress. One model for the unfolded protein response (UPR) activation involves BiP binding to the luminal portion of key transmembrane proteins that are held inactive when BiP is bound[131]. In this model, when the concentration of unfolded protein gets sufficiently high BiP favors binding the client proteins rather than the UPR transmembrane proteins. Our findings suggest that oligomerized clients within the ER would displace BiP from the UPR receptors due to the high affinity of BiP towards oligomers. This suggests that the UPR may be initiated by protein oligomerization or aggregation independent of a large change in the concentration of unfolded proteins. Given that BiP works within a system of ER chaperones, one future direction is to examine the role of electrostatics for other chaperones binding E-peptide and proIGF2 oligomers. Grp94 and the J-protein ERdj3, both of which are negatively charged, are particularly interesting candidates.

[Salt] mM	**NaCl, K_D (μM)**	**KI, K_D (μM)**	**KCl, K_D (μM)**
50	0.0047 ± 0.0022	0.021 ± 0.003	0.015 ± 0.005
300	0.29 ± 0.03	0.51 ± 0.10	0.39 ± 0.08

Table 2.1. BiP dissociation constants for E-peptide using BiP_{SBD} FRET assay with different salts, NaCl, KI, and KCl, in the presence of ADP.

Client	**Hsp70**	**K_D (μM)**	**Monomer?**	**Net charge**	**Nucleotide**	**Ref**
C_H1 domain	BiP	4.2±0.4	Yes	+1	ADP	[125]
HTFPAVL peptide	BiP	11.6±0.6	Yes	0	ADP	[116]
MAPT MBD Fibril	Hsp70	0.02±0.01	No	+10	none	[35]
MAPT MBD 10mer+	Hsp70	0.17±0.04	No	+10	none	[35]
MAPT MBD 6-10mer	Hsp70	0.34±0.09	No	+10	none	[35]
MAPT MBD 3-5mer	Hsp70	0.97±0.19	No	+10	none	[35]
MAPT MBD 1-2mer	Hsp70	5.6±1.4	Yes	+10	none	[35]
MAPT 3R*	Hsc70	0.31±0.05	*	+10	none	[130]
MAPT 4R*	Hsc70	0.16±0.04	*	+13	none	[130]

α-synuclein fibril	Hsp70	5.8±0.4	No	-9	ATP	[37]
α-synuclein monomer	Hsp70	~10	Yes	-9	ATP	[37]
NR peptide^	BiP	0.95	Yes	+1	none	[132]
leukocyte antigen B*2702-derived peptide Bw4	Hsp70	1.8	Yes	+2	ATP	[133]
NLLRLTGW^ (Javelin 1)	Hsp70	0.9	Yes	+1	ADP	[128]
Faf1 peptide^ (FYQLALT)	Hsc70	4.3±0.9	Yes	0	ADP	[120]
Faf1 peptide^ (FYQLALT)	Hsc70	37-51	Yes	0	ATP	[120]
Clathrin[#]	Hsp70	3	No	-64	90% ADP, 10% ATP	[38]
Clathrin[#]	Hsp70	12	No	-64	ATP	[38]
Cytochrome *c* peptide[@] (IFAGIKKKAERADLIA YLKQATAK)	Hsp70	7	Yes	+4	90% ADP, 10% ATP	[38]
Cytochrome *c* peptide[@]	Hsp70	300	Yes	+4	ATP	[38]

Table 2.2. Compilation of Hsp70 family dissociation constants towards client proteins. *Oligomerization state for MAPT 3R and 4R not stated. [#] Clathrin sequence from *B. taurus* and net charge calculated with one heavy chain and one light chain A. Net charge calculated with one heavy chain and one light chain B is -58. [@] Peptide from *C. livia* sequence. ^ indicates synthetic client sequences. All other client sequences are from *H. sapiens*. Peptide clients are assumed to be monomeric.

Client	**K_D (μM)**	**Monomer?**	**Net charge**	**Nucleotide**	**Ref**
Peptide pp*	0.06	Yes	+4	ADP	[134]
Peptide pp*	2.2	Yes	+4	ATP	[134]
human telomere repeat binding factor 1 (hTRF1) 377-430	1.4±0.2	Yes	+10	ADP	[135]
human telomere repeat binding factor 1 (hTRF1) 377-430	18±3	Yes	+10	ATP	[135]
Islet amyloid polypeptide (*H. sapiens*)	~pM	No	+2	apo	[129]
σ^{32} peptide (Q132-Q144) (*E. coli*)	0.078	Yes	+5	apo	[136]
σ^{32} (*E. coli*)	5	Yes	-6	apo	[137]

Table 2.3. Representative DnaK dissociation constants towards client proteins. *CALLQSRLLLSAPRRAAATARA, derivative of chicken mitochondrial aspartate aminotransferase signal sequence.

2.5 Methods

Bioinformatics

Predicted BiP-binding motifs on proIGF2 were calculated with BiPPred[121]. BiPPred calculates a predicted BiP-binding score for a 7-residue motif, and an average BiPPred score for each residue is calculated and plotted in Figure 2.7.A. Net charge is calculated from sum of –(Asp + Glu) + (Lys + Arg) residues.

Protein Purification

6-his tagged BiP was purified via Ni-NTA affinity chromatography, and 6-his tag was cleaved with TEV. Subsequent Ni-NTA affinity chromatography removed 6-his tag and TEV, anion-exchange chromatography removed nucleotide bound to BiP, and BiP was buffer exchanged with size-exclusion chromatography. BiP was stored in 25mM Tris pH 7.5, 50mM KCl, 1mM DTT, and 2% glycerol.

ProIGF2, E-peptide, E-peptide 92-139, E-peptide 92-120, and mature IGF2 were purified from inclusion bodies. E-peptide, E-peptide 92-139, and E-peptide 92-120 contained an N-terminal 6-histidine tag and cysteine mutation at Ser95 for FITC labeling. Briefly, inclusion bodies were washed and insoluble protein was denatured in an 8M urea, 25mM Tris buffer containing reducing agent TCEP. Protein was purified by ion-exchange chromatography and/or Ni-NTA affinity chromatography in denaturing conditions. Proteins used in FP assays were labeled with FITC-maleimide. Proteins were stored denatured in buffer containing 8M urea.

BiP-binding sites 1 and 3 were synthesized by Alan Scientific (Gaithersburg, MD) and site 2 was synthesized by Genscript (Piscataway, NJ). All peptides were N-terminally labeled with

FITC via an amino hexanoic acid linker. For FITC-Mature-1cys, mature IGF2 was mutated to remove all cysteines except Cys70, which was labeled with FITC.

Fluorescence Polarization

50nM FITC-labeled BiP D27C or BiP NBD D27C was incubated with buffer containing 25mM MES pH 6.0, 50/150/300 mM KCl, 1mM $MgCl_2$, 1mM nucleotide (ADP or ATP), 0.5mg/mL BSA, and 1mM DTT until polarization values reached equilibrium, for about 30 minutes, at 37°C. Experiments were also conducted in the absence of BSA, when noted. Clients were added directly from the purified stock in 8M urea, except proIGF2 (diluted out of denaturant 1:10 in 50mM MES pH 6.0, 2mM TCEP and incubated 20-30 minutes). Fluorometer setup had an excitation wavelength at 492nm and emission wavelength at 520nm with 6nm slit widths, and 1s integration time.

FP experiments containing FITC-labeled BiP-binding site peptides used 50nM of labeled peptides, except for FITC-Mature-1cys (57.5nM). For ATP experiments, FITC-labeled peptide was added to increasing concentrations of BiP pre-incubated for 20 minutes in a buffer containing 25mM buffer (MES or Tris), 50/150/300 mM KCl, 1mM $MgCl_2$, 1mM ATP, 0.5mg/mL BSA, and 1mM DTT at 37°C. For ADP experiments, contaminating ATP was removed from 1mM ADP with 0.005 units hexokinase, 1mM glucose, and 5mM $MgCl_2$ via an incubation for 1 hour at 37°C. Increasing concentrations of BiP was then incubated with HK-treated ADP mixture for 30 minutes in buffer containing 25 mM MES, 50/150/300/450 mM KCl, and 1 mM DTT, after which FITC-labeled peptide was added. FITC-peptide binding experiments with BSA were carried out by first equilibrating increasing concentrations of BSA in 25 mM MES pH 6.0, 50 mM KCl, 1 mM $MgCl_2$, 1 mM ADP, and 1 mM DTT for 30 minutes. Then, 50 nM of FITC-labeled peptide was added to

each concentration of BSA. For all FP experiments, 30 minute time point was used in calculating the K_D. Polarization measurements for FITC-E-peptide 121-139 were taken with excitation at 493nm, emission at 522nm, 5nm slit widths, and a 1s integration time. Polarization measurements with FITC-E-peptide 103-120 and FITC-E-peptide 151-169 used 493nm excitation wavelength, 518nm emission wavelength, and 6nm slit widths. FP experiments with FITC-E-peptide 92-120 or FITC-E-peptide 92-139 had an excitation wavelength of 492nm and emission wavelength of 522nm.

K_D values were calculated using the single-site binding equation,

$$P = \frac{a[x]}{K_D + [x]} + c \quad (1)$$

where *P* is polarization, *a* is the polarization amplitude, *c* is the polarization value in the absence of added protein, and *x* is the concentration of added protein. Association kinetics for 0.1μM BiP to site 1 (Figure 2.12.B) was determined by a linear extrapolation of association kinetics measured over the complete range of BiP concentrations from Figure 2.8.A. All titrations to determine K_D values were from multiple separate experiments each with a different concentration of added protein.

FRET

For the BiP-BiP FRET assay, in separate reactions, BiP was labeled with donor (AlexaFluor 555 C2 maleimide) or acceptor (AlexaFluor 647 C2 maleimide) fluorophores. 25nM donor-labeled BiP and 25nM acceptor-labeled BiP were incubated until FRET efficiency reached equilibrium, about 20-30 minutes, in buffer containing 25mM MES pH 6.0, 50mM KCl, 1mM ADP, 0.5mg/mL BSA, and 1mM DTT at 37°C. ADP was pretreated with 0.005 units hexokinase, 1mM glucose, and 5mM $MgCl_2$ for 1 hour at 37°C. Clients were added in the same manner used

in FP experiments. Fluorometer setup had donor excitation wavelength at 532nm, donor emission wavelength at 567nm, and an acceptor emission wavelength at 668nm, and 6nm slit widths. FRET efficiency (*E*) was calculated by the donor (*D*) and acceptor (*A*) emission fluorescence:

$$E = \frac{A}{D + A} \tag{2}$$

For the BiP_{SBD} FRET assay, a previously described BiP double mutant G518C and Y636C was simultaneously labeled with donor and acceptor fluorophores, AlexaFluor 555 C2 maleimide and AlexaFluor 647 C2 maleimide, respectively[116]. In the BiP_{SBD} FRET assay, the value of the FRET efficiency is limited to a value of 0.5 because at most only 50% of the BiP molecules can be labeled with one donor and one acceptor fluorophore. BiP was diluted to 50nM into buffer containing 25mM MES pH 6.0, 50/150/300/450 mM KCl, 1mM $MgCl_2$, 1mM ATP, 0.5mg/mL BSA, and 1mM DTT. Experiments with ADP contained 1 mM ADP. If indicated, hexokinase-treated ADP was incubated as above experiments. Experiments with 5% ATP had 1mM ADP and 0.05mM ATP and were completed at 50mM KCl. Fluorometer setup had a donor excitation wavelength at 532nm, donor emission wavelength at 567nm, and acceptor emission wavelength at 668nm, 4nm slit widths, and 0.5s integration time. K_D values were calculated using a single-site binding equation,

$$E = \frac{a[x]}{K_D + [x]} + c \tag{3}$$

where *a* is the FRET efficiency amplitude, *c* is the FRET efficiency value in the absence of client, and *x* is the concentration of added protein. K_D values < 0.2μM were determined via

$$E = c + a\frac{[B + x + K_D] - \sqrt{[B + x + K_D]^2 - 4[B]x}}{2[B]} \tag{4}$$

where *x* is the concentration of E-peptide, K_D is the dissociation constant between BiP and client, and *B* is the concentration of BiP_{SBD} FRET-labeled protein used in experiments.

Light Scattering

ProIGF2 and E-peptide were assayed for light scattering with an absorbance at 320nm at 25°C. Background was subtracted at 700nm. 2μM of each protein was prepared in buffer containing 25mM MES pH 6.0, 1mM $MgCl_2$, mM ATP, 0.3 mM TCEP. Immediately before assay, proIGF2 was diluted out of urea into buffer containing 50mM MES pH 6 and 2mM TCEP.

Dynamic Light Scattering

DLS data was obtained using an ALV DLS/SLS-5022F system (ALV-Laser Vertriebsgesellschaft m.b.H.) coupled with a 22 mW HeNe Laser (JDS Uniphase Corporation). E-peptide and proIGF2 were diluted into 50mM MES pH 6.0, 50mM KCl, 2mM TCEP, 1mM $MgCl_2$, and 1mM ATP. Light scattering signals from the protein samples were monitored at a 90° scattering angle. Each data point was collected and averaged from 10 rounds of 20s measurements, at 25°C and at 630nm. Each individual measurement gave an associated intensity correlation function, which was then transferred to a size-distribution function, attaining the hydrodynamic radius R_H[138].

ATPase Assay

ATPase activity was measured by depletion of NADH via an enzyme-linked assay with pyruvate kinase and lactate dehydrogenase. 2μM BiP was assayed in 25mM MES pH 6.0, 50mM KCl, 1mM $MgCl_2$, 1mM ATP, 1mM DTT, 0.5mM NADH, 0.5mM PEP, 0.1μM pyruvate kinase, 0.1μM lactate dehydrogenase, and 2.5μM client protein at 37°C. NADH depletion was monitored at an absorbance of 340nm. ATPase rates reported are an average of 3 measurements, and the error is the SEM.

CHAPTER 3: Structural Analysis and Client Binding Studies of BiP and Grp94

AUTHOR CONTRIBUTIONS

Deans, E. and Huang, B. designed, conducted and analyzed the smFRET experiments. Gelles, J. and Friedman, L.J. provided assistance and feedback for smFRET experiments. Deans, E. and Huang, B. designed and performed the analytical size exclusion chromatography experiments. Huang, B. designed and performed the Grp94 ATPase and Grp94 bulk FRET experiments. Wei, W.S. performed the dynamic light scattering measurements. Deans, E. designed and performed all other experiments. Deans, E. and Street, T. conceived the idea of the project and wrote this chapter.

3.1 Abstract

Mounting evidence indicates Hsp70/Hsp90 pairs have a conserved chaperoning function. The Hsp90/Hsp70/Hop/GR loading structure provides new structural insights into cytosolic Hsp70/Hsp90 coordinated function. However, the relevance of these insights are unclear for Hsp70/Hsp90 systems that lack Hop (bacterial Hsp70/Hsp90 and those in organelles). It is also unclear whether the loading structure, in which a monomeric client is bound, is relevant to the way in which BiP and Grp94 assist the oligomerizing client proIGF2. Here, we examine three questions raised by the loading structure for the BiP/Grp94/proIGF2 system. What is the functionally relevant stoichiometry of BiP on Grp94? How does BiP-bound client get correctly positioned between the Grp94 arms to be trapped by Grp94 closure? Can BiP and Grp94 form a ternary complex with a monomeric state of proIGF2?

3.2 Introduction

Recall from Chapter 1 that Wang and colleagues proposed a mechanism for Hsp70/Hsp90 client transfer[13]. Hop and a scaffolding Hsp70 (Hsp70S) bind Hsp90 first (Figure 3.1, step 1). The SBD of Hsp70S is not visible in the loading complex structure indicating it is likely dynamic (double arrow in Figure 3.1). The partially unfolded client, GR, is delivered to the Hop/Hsp70S/Hsp90 complex by a second Hsp70 (Hsp70C), forming the loading complex (step 2). The α-helical lid of Hsp70C is not visible in the loading structure and therefore not shown in Figure 3.1. NEF activity promotes Hsp70C to release GR and exit the complex (step 3). Asymmetric Hsp90 ATP hydrolysis is proposed to drive the release of Hsp70S and Hop (step 4). Finally, after a number of additional steps, the Hsp90 arms open and folded GR is released (step 5).

This chapter is organized around three questions raised by the loading complex mechanism that can be addressed with the BiP/Grp94 system:

1) What is the functionally relevant stoichiometry of BiP on Grp94?
2) How does BiP-bound client get correctly positioned between the Grp94 arms to be trapped by Grp94 closure?
3) Can BiP and Grp94 form a ternary complex with a monomeric state of proIGF2?

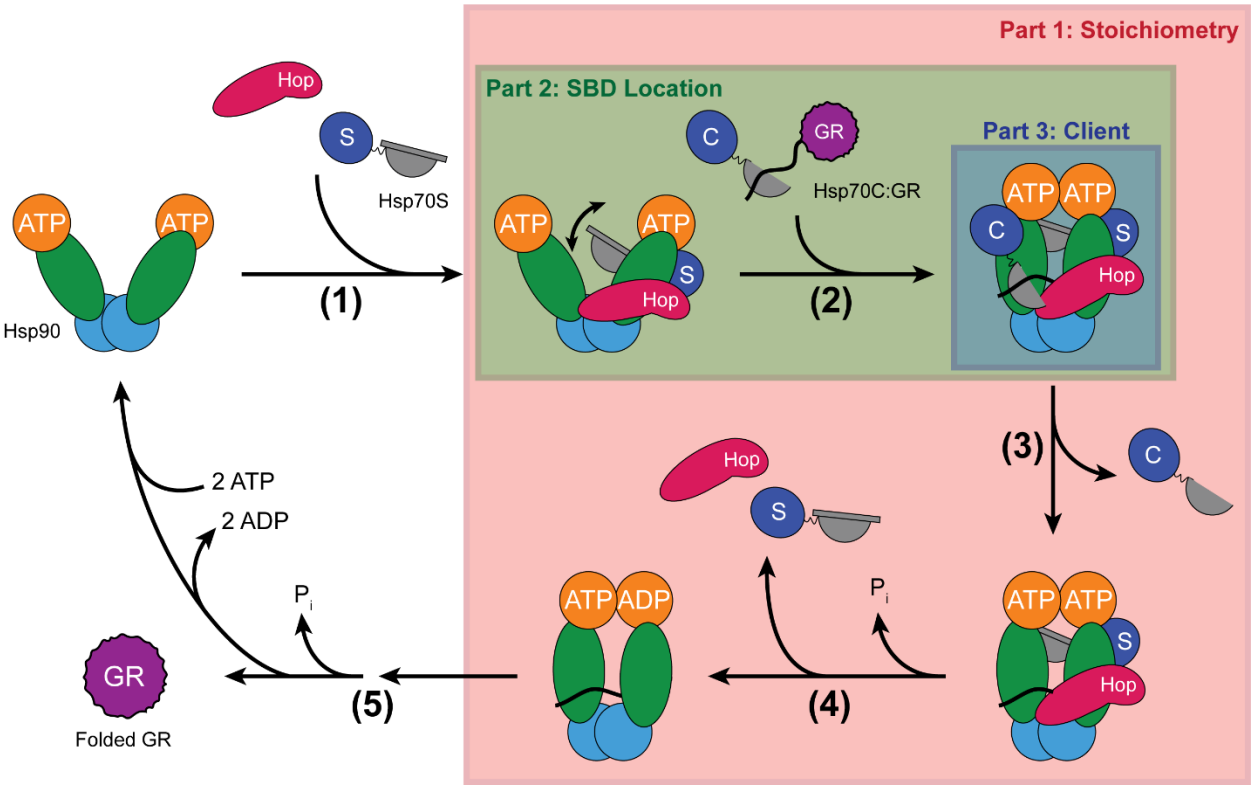

Figure 3.1. Proposed mechanism of Hsp70/Hsp90 client transfer, adapted from Wang et al. (2022)[13]. (1) Hop and Hsp70S bind to the open conformation of Hsp90. (2) Hsp70C delivers partially unfolded GR to Hsp90, forming the client-loading complex. (3) Hsp70C hands off client to Hsp90 and NEF activity promotes Hsp70C release from the complex. (4) ATP hydrolysis from one Hsp90 arm drives the release of Hsp70S and Hop. (5) Hsp90 closes and, upon re-opening, folded GR is released.

3.2.1 Part 1: Stoichiometry of Hsp70 on Hsp90?

Figure 3.1 proposes that two Hsp70s are necessary to stabilize each Hsp90 arm into the proper orientation for client delivery. Specifically, a client-free Hsp70S binds to Hsp90 first, followed by Hsp70C bound to GR. This mechanism predicts that Hsp90 will not close when a single Hsp70 and Hop is bound. In contrast, a 1:1:1 stoichiometry between the Hsp90 dimer, Hsp70, and Hop was observed both *in vitro* and in rabbit reticulocyte lysate[139,140]. While complexes with two Hsp70s bound to an Hsp90 dimer were observed *in vitro*, these complexes required two Hop monomers be bound to Hsp90 in order to form and were unable to bind other co-chaperones[139]. The functionally relevant stoichiometry of Hsp70 on Hsp90 is an open question.

The observation of BiP-dependent acceleration of Grp94 closure was made under conditions that allow one or two BiPs to bind Grp94[80]. As a result, it is unclear whether two BiPs are required for Grp94 closure (Figure 3.2 model 1, based on the proposed mechanism of GR loading by Hsp90/Hsp70/Hop), or whether a single client-bound BiP is sufficient to induce Grp94 closure and subsequent client transfer (Figure 3.2 model 2). If only one BiP is sufficient to induce Grp94 closure, it raises a new question about whether the conformation of Grp94 bound to one BiP is similar or different than the conformation of Grp94 bound to two BiPs (question mark in Figure 3.2 model 2). If both one or two BiPs can promote Grp94 closure, then it raises a question about whether the different stoichiometries could serve different functional or biological purposes.

The mechanism of GR loading by Hsp90/Hsp70/Hop proposes that Hsp70S and Hop are released by Hsp90 ATP hydrolysis on the same arm in which Hsp70S is bound (Figure 3.1, step 4). However, there was no data to indicate if Hsp90 ATP hydrolysis occurs specifically on the arm in which Hsp70 is bound or whether hydrolysis can occur on both arms.

Cooperative binding between BiP and Grp94 has been proposed based on results from a Grp94 FRET assay, in which a single bound BiP pushes Grp94 towards the C' state and the second BiP binds tightly to the C' state[80]. However, this cooperativity is contingent on a single BiP being able to drive Grp94 towards the C' state, and this requirement had not been experimentally tested in previous work. Since the proposed BiP binding cooperativity on Grp94 comes from the high affinity C' state, anything which promotes full closure of Grp94, such as ATP, will remove the binding cooperativity. Consequently, even if the cooperative binding of BiP is indeed correct, the biological relevance of this cooperativity may be limited under ATP conditions if a single bound BiP is capable of accelerating ATP-dependent closure of Grp94.

A key experimental tool for testing questions about BiP:Grp94 stoichiometry is the Grp94 K467A mutation, which abolishes BiP binding[12]. A 1:1 stoichiometry between BiP and the Grp94 dimer can be achieved with Grp94 heterodimers containing a wild-type and K467A mutant arm.

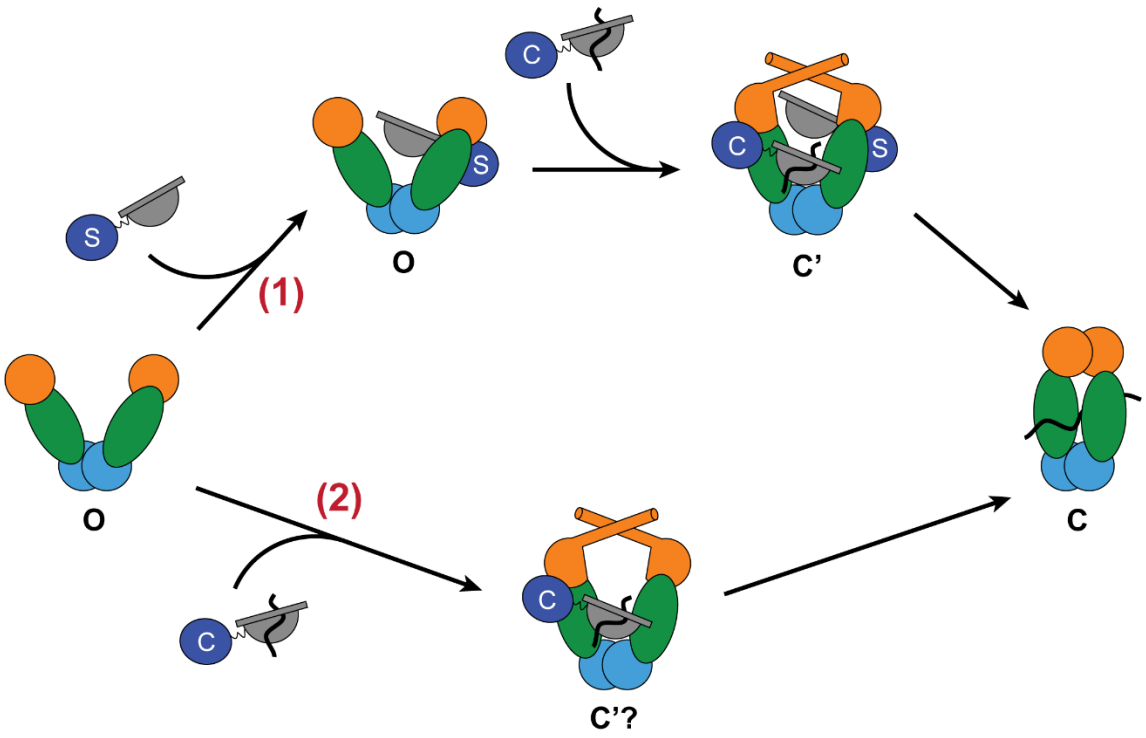

Figure 3.2. Models of BiP-dependent Grp94 closure acceleration. Model 1 depicts two BiPs being required for C' state stabilization and acceleration of Grp94 closure as proposed by the loading complex structure. Model 2 depicts a single BiP being sufficient for C' state stabilization and acceleration of Grp94 closure. Open (O), C', and closed (C) Grp94 conformational states are labeled underneath the corresponding cartoons.

3.2.2 Part 2: How Does a BiP-Bound Client Get Correctly Positioned Between the Grp94 Arms to be Trapped by Grp94 Closure?

As discussed in Chapter 1, the Hsp70 SBD is conformationally heterogenous when in the client-bound ADP-state. This likely is relevant for client transfer to Hsp90 because the Hsp70-bound client could be presented to Hsp90 in a wide variety of configurations. The loading complex proposes that Hsp70C delivers GR to Hsp90 (Figure 3.1, step 2), but minimally contributes to the positioning of GR in the binding cleft. Instead, Hop simultaneously binds GR and Hsp90α to

stabilize and guide the client into the binding cleft (Figure 3.3.A-B). However, genetic knockouts of *Hop* in mammalian cells minimally perturb client stability[141], and no Hop-like protein is expressed in bacteria, the ER, mitochondria, or chloroplasts, all of which have functional Hsp70/Hsp90 systems. This raises a question of how Hsp70 positions clients onto Hsp90 in the absence of Hop.

One possibility is that the Hsp70 SBD can guide the client by binding directly to Hsp90, but the loading complex structure provides little insight into how this could occur. The Hsp70C SBD is shown bound to GR in the loading complex but the SBD structure is low-resolution with no visible α-helical lid, and the SBD on Hsp70S was also not visible. Additionally, the extensive contacts of Hop and the globular region of GR on either side of the Hsp90 binding cleft could block possible SBD binding sites (Figure 3.3.C).

If the Hsp70 SBD can bind to Hsp90, the Hsp90 CTD amphipathic helix would be a candidate for the contact point. The amphipathic helix is a conserved region that is important for client binding and chaperone function[54]. In the loading complex, Hop guides GR to the Hsp90 binding cleft by binding the amphipathic helix via two key residues (W606 and M614, Figure 3.3.D).

BiP/Grp94 is an ideal pair to study the role of the SBD in client positioning given a previously reported two-fold difference in Grp94 affinity between BiP and the BiP NBD[12], suggesting the BiP SBD may provide stabilizing contacts to the BiP:Grp94 complex. Indeed, as discussed later, I used binding affinity measurements to show that the BiP SBD makes a stabilizing contact to the Grp94 CTD on the same arm in which BiP is bound.

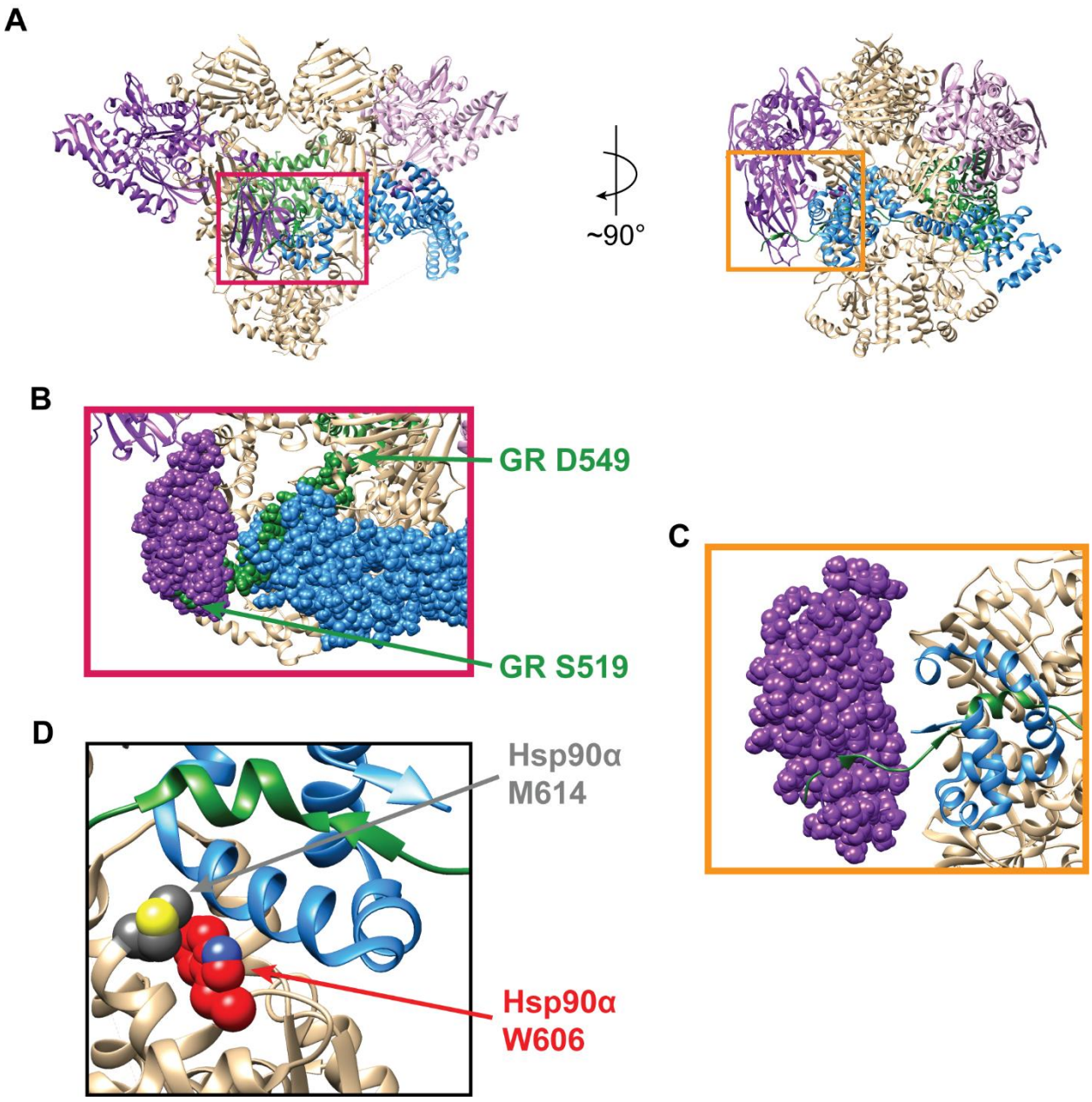

Figure 3.3. A. Front (left) and side (right) view of the Hsp90:Hsp70:Hop:GR loading complex structure (PDB: 7KW7). Hsp90 is shown in tan, Hsp70C in purple, Hsp70S in pink, Hop in blue, and GR in green. **B.** Hop binding and stabilizing GR within the Hsp90 binding cleft. The unfolded region of GR is simultaneously bound by the Hsp70C SBD, Hop, and Hsp90 in a C-to-N orientation. **C.** The Hsp70C SBD does not interact with Hsp90 or Hop. **D.** Position of W606 (red) and M614 (gray) on the Hsp90α amphipathic helix.

3.2.3 Part 3: Can BiP and Grp94 Form a Ternary Complex with a Monomeric State of proIGF2?

30 residues of the unfolded region of GR (residues 519-549) in the loading structure spans the Hsp70C SBD binding cleft, to Hop, and through the Hsp90 arms (Figure 3.3.B). A model client for BiP/Grp94 mechanistic analysis would need to be at least 30 residues to reach the Grp94 binding cleft while simultaneously bound to BiP. Further, to date, all high-resolution structures of full-length Hsp90 bound to a client show a monomeric and unfolded client in the binding cleft[13,52,53]. These criteria pose a problem for the current client of BiP/Grp94, proIGF2, which meets the criteria for length, but forms large, dynamic oligomers[34]. GR is known to form homodimers and tetramers when not in complex with Hsp70/Hsp90[142,143], and may form higher order oligomers similar to the closely-related mineralcorticoid receptor[144]. However, the observed GR oligomeric states are small compared to that of proIGF2. Because of this, it remains unclear if GR and proIGF2 use their respective Hsp70/Hsp90 systems in a similar way. For example, it is not known if BiP and Grp94 can even form a ternary complex with a monomer of proIGF2. I set out to answer this question by designing a large monomeric fragment of proIGF2.

Small peptide clients characteristically bind in the lid-closed state of BiP, however less is known about the mode of binding to larger clients. For example, a large fragment of the C_H1 client was proposed to bind BiP in an open-lid state, as determined by FRET measurements in which the donor and acceptor fluorophores produce low FRET efficiency in the lid-open state and high FRET efficiency in the lid-closed state[116]. Further, binding of the large antibody domain C_H3 decelerates BiP ATPase activity[145]. These observations suggest that BiP binds large clients in a lid-open, ATP-like conformation. If this is the case, interface I on the BiP NBD would not be accessible, preventing BiP from binding Grp94. The loading complex provides little insight into how Hsp70s could bind larger clients since Hsp70C is simultaneously bound to Hsp90α and GR, but the SBD

lid is not resolved. A large, monomeric proIGF2 construct could also be utilized to address this question.

3.3 Results

3.3.1 Part 1: Stoichiometry of BiP on Grp94

The proposed GR loading mechanism raises three issues about BiP:Grp94 stoichiometry: 1) Although BiP accelerates ATP-dependent closure of Grp94[80], the BiP stoichiometry needed to achieve closure acceleration is not known. 2) It is not known whether BiP stimulates Grp94 ATP hydrolysis specifically on the arm in which BiP is bound, or whether ATP hydrolysis can occur on both arms. 3) It is unclear whether Grp94 adopts different conformations when one or two BiPs are bound. This section examines BiP:Grp94 stoichiometry using three assays: Grp94 ATP turnover rate, kinetic Grp94 FRET, and equilibrium Grp94 FRET. The data in this section was collected by Bin Huang, but is relevant for my results with the BiP SBD and new client construct, which were primarily measured under conditions in which only one BiP can bind the Grp94 dimer.

Grp94 ATPase was measured for homodimers (WT/WT) where BiP can bind both dimer arms, and for heterodimers (WT/K467A) where BiP can only bind one arm (see Methods for procedure of calculating heterodimer ATPase). In the absence of BiP, K467A homodimers (K467A/K467A) and WT/K467A heterodimers have a similar ATPase as WT/WT (Figure 3.4.A), indicating the K467A mutation does not kinetically perturb the conformational cycle of Grp94. BiP stimulates WT/WT and WT/K467A ATPase to a similar extent, indicating a single BiP bound is sufficient for maximal ATP turnover by Grp94.

Grp94 heterodimers with E103A (a hydrolytically inactive variant[96]) on one arm and K467A on the other arm (E103A/K467A) force BiP to bind to a Grp94 arm that is incapable of hydrolyzing ATP. BiP enhances the ATPase of WT/K467A and E103A/K467A to a similar extent

(Figure 3.4.A), which excludes a model where BiP enhancement of hydrolysis can only occur on the Grp94 arm in which BiP is bound.

ATP turnover by Grp94 depends on closure and opening rates. To determine the influence of BiP stoichiometry on Grp94 closure, we constructed FRET-labeled K467A variants (donor and acceptor fluorophores at residue 91) and utilized a previously established bulk FRET assay to measure the rate of ATP-dependent closure[80,85]. The K467A/K467A homodimer has a closure rate comparable to WT/WT Grp94 and, as expected, no closure acceleration from the BiP NBD (Figure 3.4.B). In contrast, a single bound BiP is sufficient to accelerate ATP-dependent Grp94 closure (see WT/K467A+ATP+NBD in Figure 3.4.B). The BiP-induced acceleration of closure is slower for WT/K467A versus WT/WT, but the interpretation is complicated. Specifically, at low micromolar BiP concentrations the observed closure kinetics are rate-limited by the binding of BiP to Grp94, as has been discussed in a previous publication[80]. Because the WT/WT homodimer has two BiP binding sites and the WT/K467A has only one site, the rate of BiP binding to the WT/K467A construct should be slower.

BiP accelerates WT/WT arm closure more than for WT/K467A (Figure 3.4.B), whereas BiP stimulates Grp94 ATPase of WT/WT and WT/K467A to a similar extent (Figure 3.4.A). This might seem like a discrepancy, but it is the expected result. This is because BiP acceleration of Grp94 arm closure makes the ATPase cycle rate-limited by arm opening, and this step is not influenced by BiP[80].

The above results answer questions 1 and 2 from the start of this section. Specifically, a single BiP can accelerate ATP-dependent closure of Grp94, which results in ATP hydrolysis on either or both Grp94 arms in a manner that is not specific to the arm in which BiP is bound.

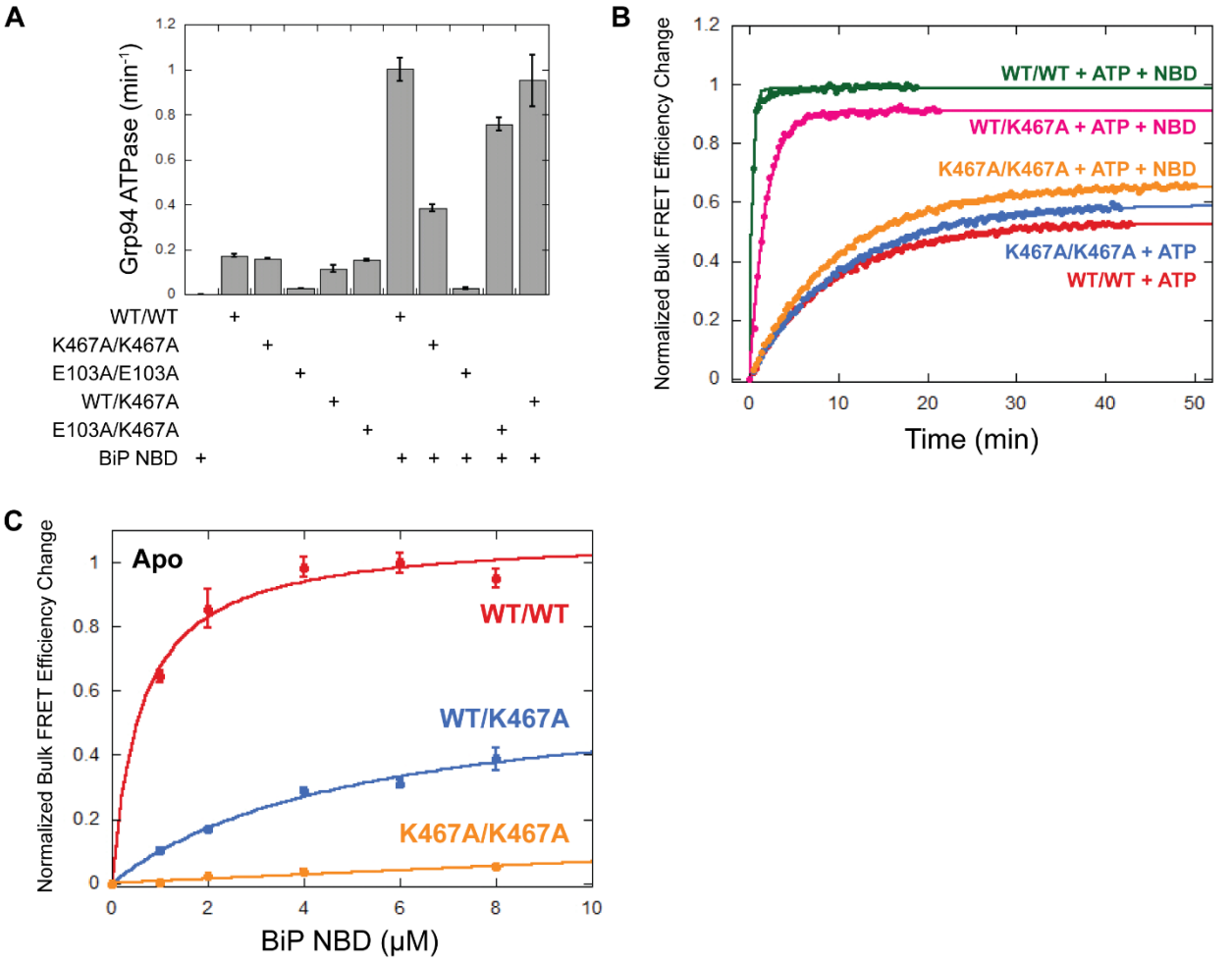

Figure 3.4. A. ATPase activity of wild type Grp94 and various mutants with and without 6μM of a hydrolytically inactive BiP NBD variant. ATPase values for Grp94 heterodimers were calculated using Equation 1. **B.** Grp94 bulk FRET efficiency measuring ATP-dependent closure with or without 2μM BiP NBD. Solid lines are fit with a single exponential. Closure rates with BiP NBD: WT/WT: 3.34 ± 0.18 min^{-1}; K467A/K467A: 0.10 ± 0.01 min^{-1}; WT/K467A: 0.58 ± 0.05 min^{-1}. Closure rates without BiP NBD: WT/WT: 0.10 ± 0.01 min^{-1}; K467A/K467A: 0.08 ± 0.01 min^{-1}. **C.** Grp94 bulk FRET efficiency changes in the presence of variable concentrations of BiP NBD and the absence of nucleotide. WT/WT and WT/K467A solid lines are fit to Equation 4 (WT/WT $K_{D,app}$ = 0.61±0.05μM; WT/K467A $K_{D,app}$ = 5.20±0.94μM), K467A/K467A solid line is a linear fit. Error bars are the SEM for at least three measurements.

We next examined whether Grp94 adopts different conformations when either one or two BiPs are bound (question 3). Recall from Chapter 1 that the stabilization of the Grp94 C' state by BiP was measured previously by smFRET in the absence of ATP, in which saturating concentrations of BiP push the Grp94 conformational equilibrium towards the C' state[80]. At saturating conditions two BiPs would be bound, leaving open the possibility that Grp94 adopts a

conformation different from the C' state when only one BiP is bound. Figure 3.4.C shows bulk FRET measurements of WT/WT and WT/K467A Grp94 constructs with variable concentrations of the BiP NBD, which show a difference in saturating FRET efficiency. Of note, the apparent K_D values reported in Figure 3.4.C are concentrations of BiP NBD which alter the conformation of Grp94 and do not directly report on BiP NBD/Grp94 binding affinity. Either Grp94 adopts a conformation different from the C' state when a single BiP is bound, or Grp94 adopts the C' state but the population is lower. Bulk FRET measurements cannot distinguish between those possibilities, so we constructed WT/K467A heterodimers for smFRET measurements (see Methods).

Figure 3.5 compares smFRET efficiency histograms for WT/WT and WT/K467A Grp94 with 2μM BiP. This concentration of BiP is over ten-fold above the K_D (0.16±0.06μM, Figure 3.6) and thus represents a saturating condition. For WT/WT, the majority of Grp94 is in the C' state (ε = ~0.9, Figure 3.5.A), whereas when only one BiP can bind Grp94, the C' state is less populated than the open state (ε = ~0.2, Figure 3.5.B). These results cannot exclude the possibility that subtle structural differences may exist between the open and C' states of Grp94 when bound to one versus two BiPs, and the presence of other low-population states. For example, the smFRET efficiency histogram for WT/K467A has a shoulder at $\varepsilon \sim 0.4$ (red arrow in Figure 3.5.B). This shoulder could correspond to an intermediate conformation of Grp94 which is populated when only one BiP is bound, perhaps similar to the Grp94 conformations that accumulate with the Hsp990 and XL888 inhibitors as discussed in Chapter 4. However, a previous analysis of the influence of the BiP NBD on the shape of Grp94 smFRET efficiency histograms shows signal averaging that can also produce intermediate FRET efficiency values[80]. Overall, we conclude that a binding stoichiometry of one versus two BiPs per Grp94 dimer yields a roughly similar set of Grp94 conformations (open

and C'), but a different conformational equilibrium in which the binding of two BiPs increases the Grp94 C' population.

Collectively, our results show that a stoichiometry of one BiP per Grp94 dimer is sufficient to stabilize the C' state and accelerate ATP-dependent closure, resulting in ATP hydrolysis on either or both arms of Grp94. This finding differs from the proposed mechanism from Wang and colleagues (Figure 3.1) and is consistent with model 2 from Figure 3.2. Given that both one or two BiPs can promote Grp94 closure, it raises a question about whether these different stoichiometries serve different functional or biological purposes. In the Discussion I will describe a possible connection between ER stress and the stoichiometry of BiP on Grp94. The 1:1 stoichiometry is the framework against which I will examine the role of the BiP SBD and client binding to the BiP/Grp94 system.

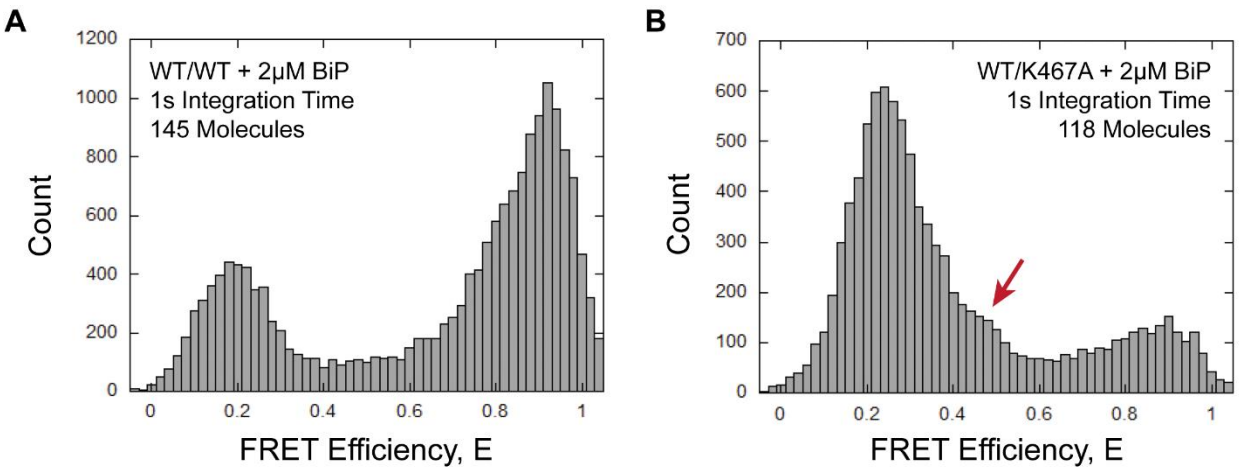

Figure 3.5. A. smFRET efficiency histogram for WT/WT Grp94 homodimers with 2μM BiP in the absence of nucleotide. **B.** smFRET efficiency histogram for WT/K467A Grp94 heterodimers with 2μM BiP in the absence of nucleotide. smFRET data collected at an integration time of 1s (520μW at 532nm, 150μW at 633nm).

3.3.2 Part 2: The BiP SBD Stabilizes the BiP/Grp94 Complex

The loading structure shows Hop stabilizing and guiding GR in the Hsp90α binding cleft, raising the question of how this is done in Hsp70/Hsp90 systems which lack a Hop-like protein

(bacterial, ER, and mitochondrial). In the ER system, the BiP SBD may play a Hop-like role by directly binding Grp94 to position clients since removal of the SBD from BiP results in ~7-fold weaker binding to Grp94 (Figure 3.6). In this assay, FITC-BiP and FITC-BiP NBD are held constant at a low concentration (50nM) which results in FP values from a single BiP bound per Grp94 dimer. As discussed in the introduction, previous measurements of BiP binding Grp94 reported only a two-fold decrease in affinity due to the removal of the SBD[12]. While the experimental conditions differ, a notable factor contributing to the 7-fold change reported here is the removal of contaminating ATP from ADP stocks via hexokinase-treatment (HK-ADP, see Methods). HPLC estimates commercial stocks of ADP contain ~2% ATP[119], which BiP will preferentially bind.

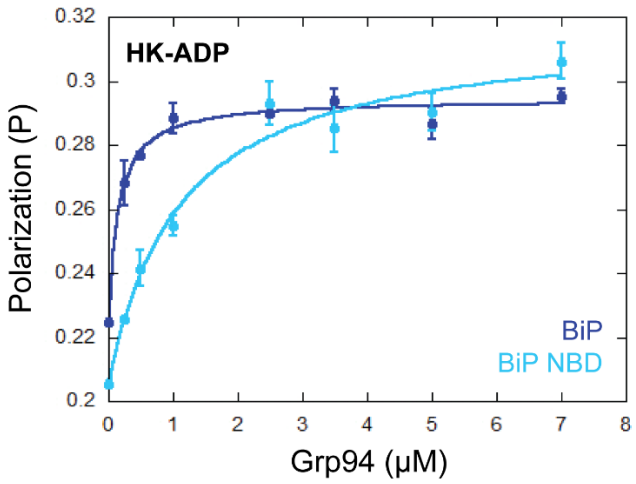

Figure 3.6. FP Grp94 binding assay with FITC-BiP (dark blue) and FITC-BiP NBD (light blue). Grp94 affinity for BiP is 0.16±0.06μM and Grp94 affinity for BiP NBD is 1.12±0.16μM. Solid lines are fit to Equation 7. Error bars are the SEM of three measurements.

The 7-fold difference in Grp94 affinity for full-length BiP versus the NBD suggests that the SBD forms a stabilizing contact somewhere on the Grp94 dimer. To identify the domain of Grp94 that interacts with the BiP SBD, I compared the binding affinity of BiP and the BiP NBD to different Grp94 constructs (Figure 3.7.A). The first Grp94 construct contains only the NTD and

MD (NM Grp94) and lacks the ability to dimerize via the CTD. BiP and the BiP NBD bind the NM fragment of Grp94 with comparable affinity. The second Grp94 construct contains the CTD but cannot dimerize due to the removal of a key α-helix in the dimerization interface (see Methods). Size exclusion chromatography shows this construct elutes later than wild-type Grp94, indicating it is monomeric (Figure 3.7.B). BiP binds this monomeric Grp94 with four-fold higher affinity than the BiP NBD. We conclude that the BiP SBD forms a stabilizing contact to the CTD of Grp94 on the same arm in which BiP is bound.

Recall from the introduction that the amphipathic helix is a candidate for the SBD binding site on the Grp94 CTD since this is a Hop contact point in the loading complex structure. Mutation of the amphipathic helix residues that interact with Hop in the structure (W654 and M662 in Grp94) only modestly weaken BiP binding affinity (Figure 3.7.A). The modest decrease in BiP binding affinity indicates the SBD either binds the Grp94 CTD in a different location, binding is

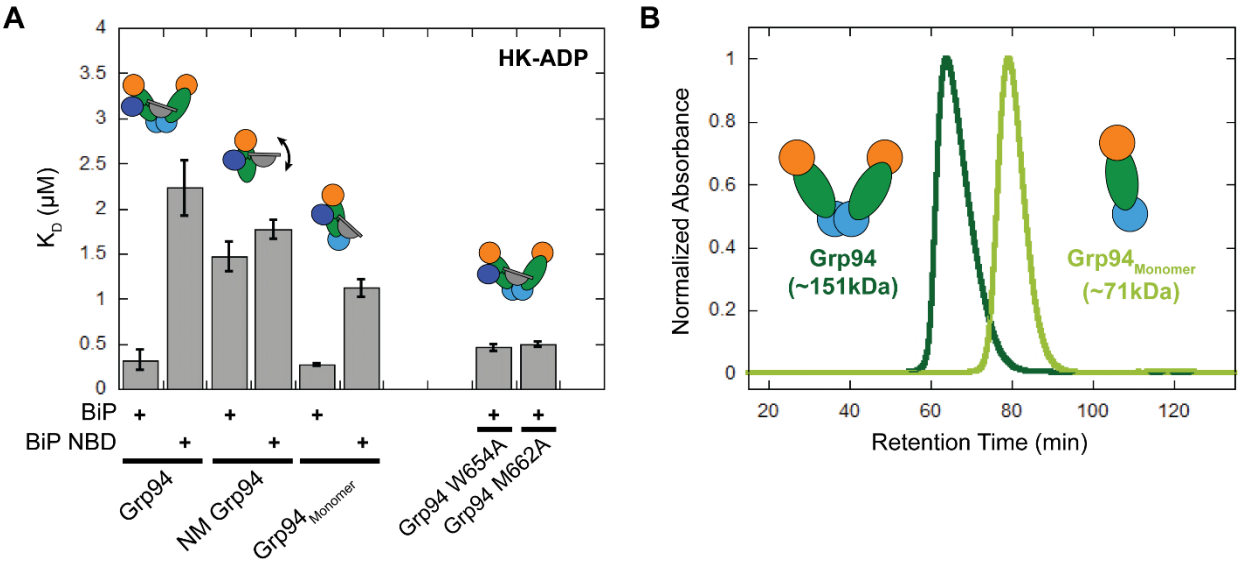

Figure 3.7. A. Binding affinities of BiP and BiP NBD for various Grp94 constructs. Affinity values are reported in Grp94 monomer concentration where applicable. Error bars are the SEM of three measurements. **B.** Size exclusion chromatography elution profile of Grp94 (dark green) and $Grp94_{Monomer}$ (light green).

dispersed across the amphipathic helix, or there is more than one SBD interaction site on Grp94. More work is needed to determine the specific Grp94 residues that interact with the BiP SBD.

Binding of the BiP SBD to the Grp94 CTD differs from what is observed in the loading structure. However, binding measurements cannot determine whether the SBD is docked with one predominant location on the Grp94 CTD or with a wide ensemble of orientations. I utilized smFRET to address this question. I designed a FRET pair that includes a donor-labeling site on the Grp94 CTD and an acceptor-labeling site on the BiP SBD_{β} region to track the position of the BiP SBD relative to the Grp94 CTD in real time ($Grp94_D$/BiP SBD_A, see Methods). A key element of the experimental design is using a Grp94 heterodimer construct in which BiP can only bind to one arm (WT/K467A), so that the FRET signal only can arise from a single BiP. Specifically, one Grp94 arm contains the donor label and the other arm contains the K467A mutation and the SNAP-biotin linkage needed for attachment to the TIRF microscope slide (Methods). Acceptor-labeled BiP is incubated with ADP and Grp94 prior to imaging and the $Grp94_D$/BiP SBD_A complexes are tethered at a low density to a PEG/PEG-biotin derivatized microscope slide coated with streptavidin (Figure 3.8.A, see Methods).

Individual $Grp94_D$/BiP SBD_A complexes exhibit two distinct FRET states (Figure 3.8.B). The smFRET data shown in Figure 3.8.B was collected with alternating excitation, which enables continuous monitoring of whether BiP is bound by measuring the direct acceptor excitation. One state (~64% of the population) has a high mean FRET efficiency (ε=0.73) and the other (~36%) has a low FRET efficiency (ε=0.40). Both states have a comparable width of FRET efficiency values suggesting the conformational heterogeneity within each state is similar. The use of WT/K467A heterodimers should ensure that the bimodal FRET efficiency histogram does not arise from a mixture of one and two BiPs being bound, but as an additional test we evaluated the direct

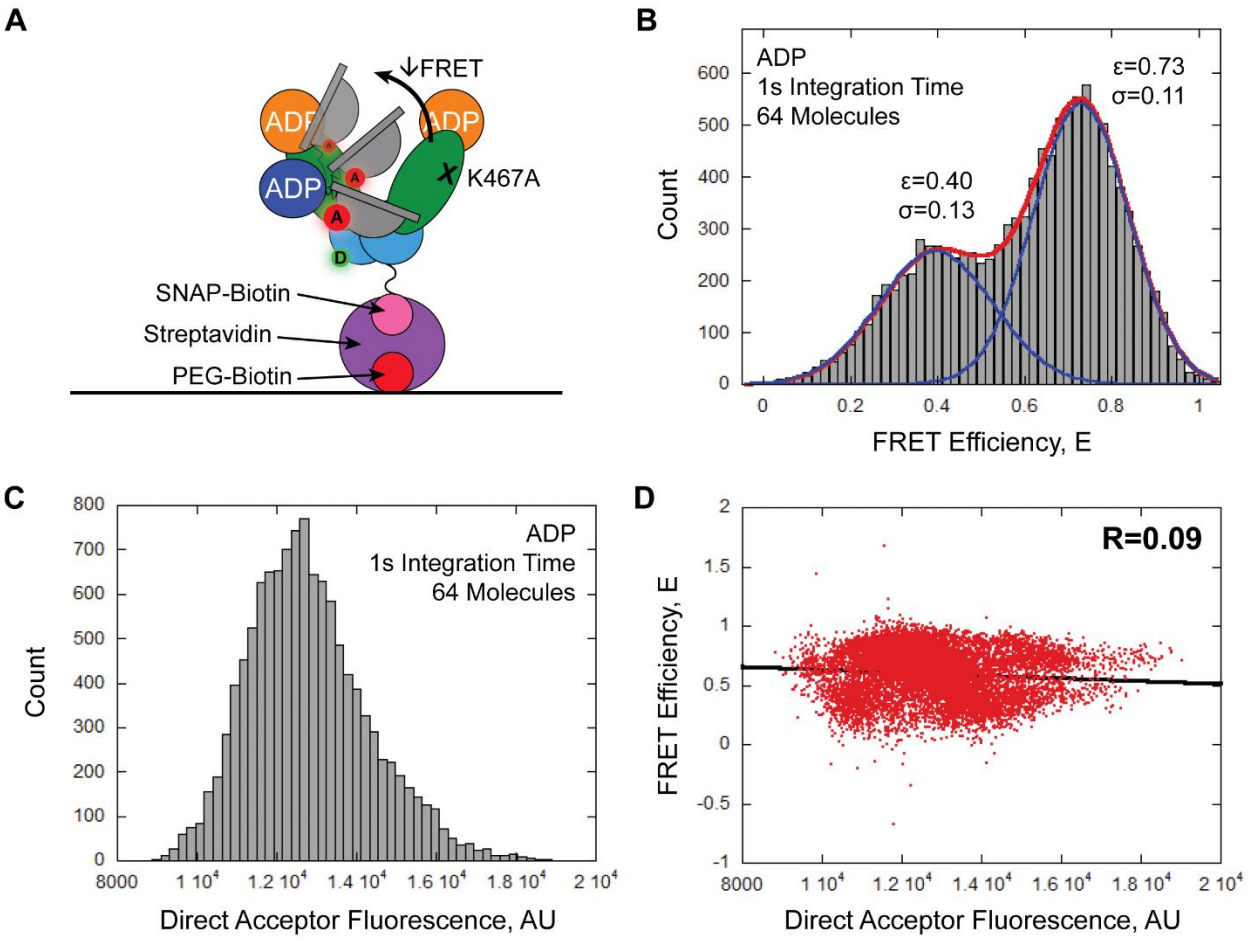

Figure 3.8. A. Cartoon of $Grp94_D$/BiP SBD_A smFRET experimental setup. **B.** smFRET efficiency histogram for $Grp94_D$/BiP SBD_A under ADP conditions. Solid lines are fit with Equation 6. Fit values of the mean FRET efficiencies (ε) and standard deviation (σ) are reported next to the corresponding Gaussian curve. Data was collected with alternating excitation (650μW at 532nm, 150μW at 633nm). **C.** Direct acceptor fluorescence intensity histogram for BiP SBD_A from the measurements shown in panel B. **D.** FRET efficiencies from panel B plotted against corresponding acceptor fluorescence intensity from panel C. Black solid line is a linear fit with correlation coefficient (R).

acceptor fluorescence intensity of BiP. A unimodal acceptor fluorescence distribution is observed, with no correlation between the direct acceptor fluorescence and FRET efficiency (Figure 3.8.C-D), indicating that the two FRET states come from only one bound BiP with two configurations of the SBD.

No clear examples of interconversion between the two SDB FRET states are observed, indicating that SBD conformational changes could be occurring at a timescale comparable to the 1s integration time. Measurements with shorter data integration times and higher time resolution

address this question. Individual traces at both 250ms and 65ms integration times reveal BiP SBD_A can interconvert between the high and low FRET states (Figure 3.9.E-F). If the SBD is converting between the two FRET states at a timescale of ~1s, there will also be visible effects to the FRET efficiency histograms at shorter integration times. The FRET states should decrease in width (σ) as the conversions are no longer being averaged together to appear as intermediate FRET values (E~0.5-0.6). This is, indeed, what we observe. The FRET efficiency histograms at 250ms and 65ms integration times show the low FRET state decreases in width, indicating the two states are more resolved compared to the 1s integration time data (Figure 3.9.D). Additionally, the FRET efficiency histograms at 250ms and 65ms show a low FRET signal ($\varepsilon<0.2$) which is not present in the 1s integration time data (Figure 3.9.A-B). This FRET signal will be discussed in further detail later.

Shorter integration times can also lead to different effects on FRET efficiency histograms when there are dynamics within a FRET state. One possibility is that a FRET state at longer integration times could be the average of two or more subpopulations. This would occur if the SBD subpopulations interconvert at a faster timescale than the measurement integration time. If this is the case, new FRET states should be resolved with shorter integration times. The smFRET measurements at both 250ms and 65ms integration times exhibit comparable FRET states as the 1s integration data (ε~0.7 and ε~0.35) with no additional peaks visible (Figure 3.9.A-B and D), indicating no additional subpopulations.

Another possibility is the SBD is not bound to Grp94 and instead the SBD FRET states arise from localized dynamic movement. If the SBD is not bound to Grp94, its movement would be confined to a specific area due to the flexible linker which connects the SBD to the stably bound NBD (Figure 3.8.A). If the dynamic movement of the SBD within this confined area occurs on a

timescale faster than the measurement integration time, the resulting FRET signal would be the average of an ensemble of SBD locations. Less averaging of SBD locations would occur at faster integration times, which would increase the FRET state broadness (σ). The width of the high FRET state remains consistent at all integration times while the width of the low FRET state modestly decreases with faster sampling (Figure 3.9.D). An additional test of localized dynamic movement is to fit both FRET states with the same σ value. The σ values shown in Figure 3.9.D are from fits which allowed both FRET states to have floating values. If neither FRET state exhibits peak widening at faster integration times, both states can be fit with the same σ value and have a comparable quality fit to those in Figure 3.9.D. The high and low FRET states in Figures 3.9.A-B were fit with the same σ values, and exhibit a comparable quality fit to those with floating values. Further, the high and low FRET states are populated to a similar degree at all integration times tested (Figure 3.9.D). Our results suggest the BiP SBD adopts two stable configurations on Grp94.

The smFRET data shown in Figure 3.9.A-B was collected with continuous excitation. Unlike the alternating excitation experiments in Figure 3.8, continuous excitation does not allow us to monitor BiP by direct acceptor excitation, which creates ambiguity about whether BiP is continuously bound during the experiment. To ensure our data does not include instances of BiP SBD_A photobleaching or BiP dissociation prior to $Grp94_D$ photobleaching, only molecules which had a corresponding BiP SBD_A signal at the beginning and end of imaging were analyzed. However, this does not eliminate other possibilities such as blinking of the acceptor fluorophore or BiP re-binding to Grp94 after dissociating. As a result, we expect to see low donor only FRET signal from Grp94 in the FRET efficiency distributions. Donor fluorophores have weak emission light at the same wavelength as acceptor fluorophore emission, resulting in a low apparent FRET signal. We measured the Grp94 signal alone (Figure 3.9.C) and fixed the mean FRET efficiency

(ε) and standard deviation (σ) parameters in a third Gaussian (ε=0.1) to account for this added low FRET signal (Figure 3.9.A-B).

Collectively, our results indicate that the BiP SBD is converting between two stable configurations on Grp94, and the interconversions occur on a timescale of ~1s since they appear to be averaged out in the 1s integration time data. More work is needed to understand BiP SBD docking on Grp94, specifically the interaction regions on both chaperones, as well as how client proteins effect these interactions.

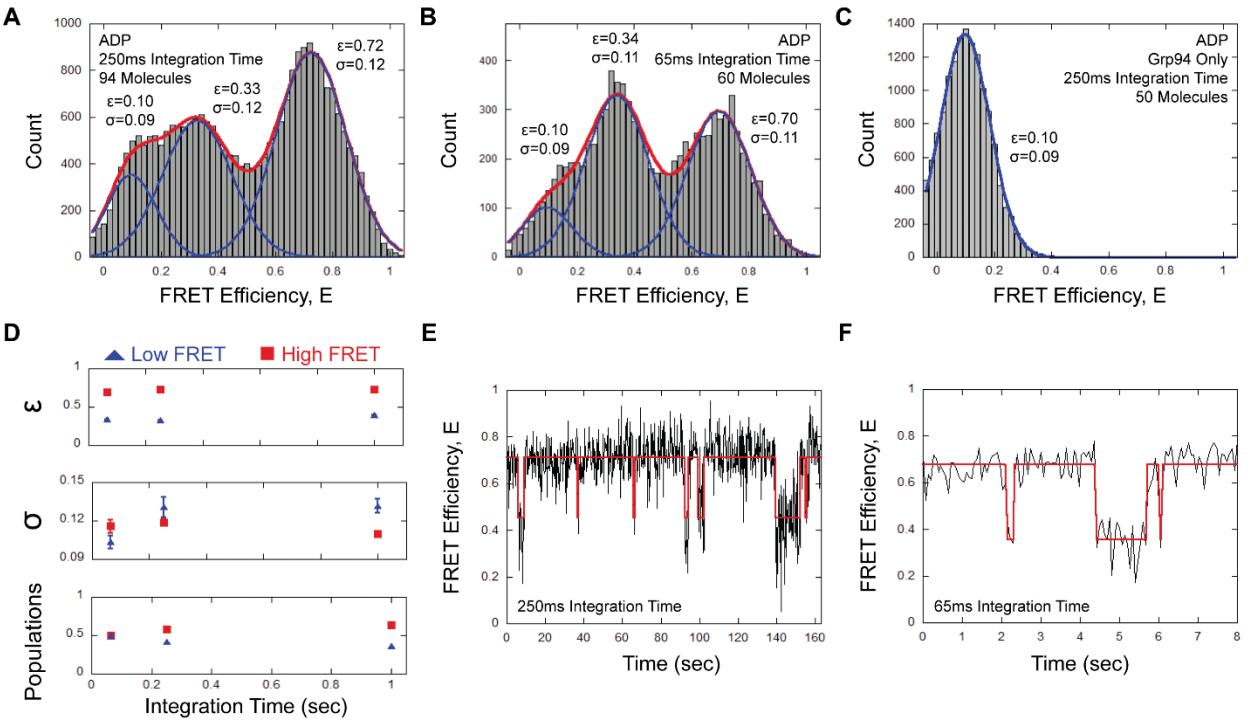

Figure 3.9. A-B. smFRET efficiency histograms for $Grp94_D$/BiP SBD_A with ADP measured with integration times of 250ms (**A**, 2.6mW at 532nm) and 65ms (**B**, 10.4mW at 532nm). **C.** smFRET efficiency histogram for $Grp94_D$ only with ADP measured with an integration time of 250ms (2.6mW at 532nm). Solid lines are fit with Equation 6. Fit values of the mean FRET efficiencies (ε) and standard deviation (σ) are reported next to the corresponding Gaussian curve. **D.** Comparison of the ε values (top), σ values (middle), and populations (bottom) for the low FRET (blue triangles) and high FRET (red squares) configurations of the SBD at different integration times. Error bars are the fitting error. **E-F.** Example smFRET traces from measurements in panel A (**E**) and B (**F**) showing BiP SBD_A interconversion between high and low FRET states. Red solid lines are from ebFRET[146,147] to show transitions between each FRET state and are for visual purposes only.

3.3.3 Part 3: BiP Can Bind a Monomeric Fragment of proIGF2

The loading structure shows monomeric GR in the Hsp90α binding cleft. While GR can form dimers and tetramers, these oligomeric states are small compared to proIGF2 dynamic oligomers. The differences in oligomeric states between GR and proIGF2 raises the question if these two clients use their respective Hsp70/Hsp90 systems in a similar way. The first step in addressing this question is to determine if BiP can bind to a large monomeric fragment of proIGF2 and form a stable ternary complex with Grp94. An ideal proIGF2 fragment for mechanistic analysis with BiP/Grp94 would need to be unfolded, monomeric, include the primary BiP binding site ("site 1" from Chapter 2), and be long enough to reach the Grp94 binding cleft while simultaneously bound to BiP. These criteria disqualify E-peptide, mIGF2 and all of the E-peptide fragments discussed in Chapter 2. I designed a proIGF2 truncation which removes the E-peptide region past site 1 (proIGF2$_{25\text{-}120}$, Figure 3.10.A). ProIGF2$_{25\text{-}120}$ is a single cysteine construct which prevents the mIGF2 region from forming the disulfide bonds necessary to fold. The remaining cysteine (C70) allows for fluorescent labeling of the client. I tested this construct to see if it fits the necessary criteria for BiP/Grp94 mechanistic analysis.

To examine the oligomeric state of proIGF2$_{25\text{-}120}$, we performed analytical size exclusion chromatography (SEC). The elution profile of proIGF2$_{25\text{-}120}$ shows two peaks, which suggests a modest level of self-association (Figure 3.10.B-C). Purified proIGF2$_{25\text{-}120}$ has no visible contaminating proteins on an SDS PAGE gel (Figure 3.10.B inset), indicating the sample is pure and the two elution peaks are solely due to proIGF2$_{25\text{-}120}$. The ratio between these two peaks is only weakly concentration dependent and no additional elution peaks with lower retention times are observed at higher concentrations of proIGF2$_{25\text{-}120}$. When compared to the elution profiles of protein standards, the retention time for both proIGF2$_{25\text{-}120}$ peaks are close to the expected molecular weight (Figure 3.10.D, molecular weight of proIGF2$_{25\text{-}120}$ indicated by dashed line).

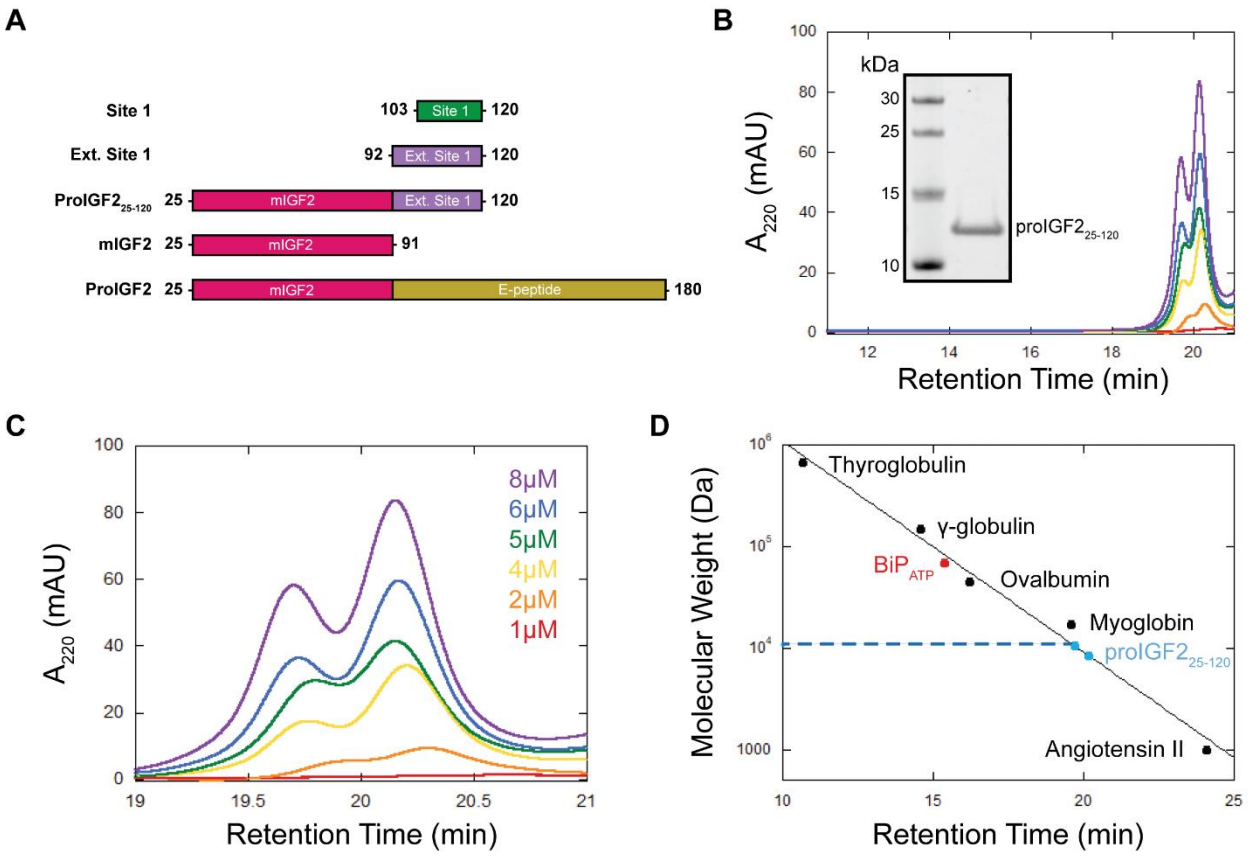

Figure 3.10. A. ProIGF2 client fragments. Color shading indicates BiP binding sites previously determined in Chapter 2: E-peptide (yellow), mIGF2 (pink), site 1 (green), and extended site 1 (Ext. Site 1, purple). **B-C.** SEC elution profile of various concentrations of FITC-proIGF2$_{25-120}$. (*Inset*) SDS PAGE gel of purified proIGF2$_{25-120}$. **D.** Calibration curve of molecular weight versus retention time of standard proteins (black). Positions of proIGF2$_{25-120}$ (blue) and BiP$_{ATP}$ (red) are indicated. Dashed line indicates actual molecular weight of proIGF2$_{25-120}$.

Overall, our SEC results indicate proIGF2$_{25-120}$ adopts different oligomeric states or configurations. The two peaks could be modest self-association, or expanded and collapsed configurations of proIGF2$_{25-120}$ which run differently by SEC.

ProIGF2 and E-peptide cannot be analyzed by SEC because they form large oligomers that interact with the resin. Dynamic light scattering (DLS) measurements can quantify the mean hydrodynamic radius (R_H) of proIGF2 and E-peptide oligomers. At a concentration of 1μM, proIGF2 oligomers have an R_H value of 1120±80nm, E-peptide oligomers have an R_H value of 330±50nm, whereas proIGF2$_{25-120}$ produces so little light scattering that an R_H value cannot be

determined reliably. Overall, we conclude that proIGF2$_{25\text{-}120}$ does not form the large oligomers characteristic of proIGF2 and E-peptide and is primarily monomeric when at low micromolar concentrations.

We next examined BiP binding to proIGF2$_{25\text{-}120}$ by SEC. In the absence of client, BiP has different elution times when under ATP (BiP$_{ATP}$: 15.8 minutes) and ADP (BiP$_{ADP}$: 13.4, 14.1, 14.8, and 15.6 minutes) conditions (Figure 3.11.A). The BiP$_{ATP}$ elution is approximately what would be predicted according to the standard curve in Figure 3.10.D, whereas the earlier elution of BiP$_{ADP}$ is consistent with the expanded ADP conformation and BiP oligomerization. Contaminating ATP was not removed from ADP stocks prior to SEC measurements and the BiP$_{ADP}$ peak at 15.6 minutes is likely BiP bound to ATP. To monitor client binding to BiP we used FITC-labeled site 1 and proIGF2$_{25\text{-}120}$ which enables client elution to be tracked by absorption at 495nm while simultaneously monitoring BiP by the absorption at 280nm. The site 1 peptide (17 residues) is a control because it is too short for the binding of two BiPs. If a BiP:proIGF2$_{25\text{-}120}$ complex elutes at the same retention time as BiP:site 1, this would indicate that a single BiP is bound to proIGF2$_{25\text{-}120}$. Conversely, if the BiP:proIGF2$_{25\text{-}120}$ complex elutes at a retention time similar to a BiP dimer, then this would indicate two BiPs are bound to proIGF2$_{25\text{-}120}$. The BiP:proIGF2$_{25\text{-}120}$ and BiP:site 1 retention times are similar and no additional elution peaks with lower retention times are observed (Figure 3.11.B). The retention times of BiP:proIGF2$_{25\text{-}120}$ and BiP:site 1 are both similar to monomeric BiP (Figure 3.11.C), indicating a single BiP is binding proIGF2$_{25\text{-}120}$.

FP measurements of FITC-labeled proIGF2$_{25\text{-}120}$ show that BiP binds this client with low micromolar affinity under ADP conditions, and only a ~1.5-fold reduction in affinity under ATP conditions (Figure 3.12.A). This modest reduction in affinity is not what is observed for other site

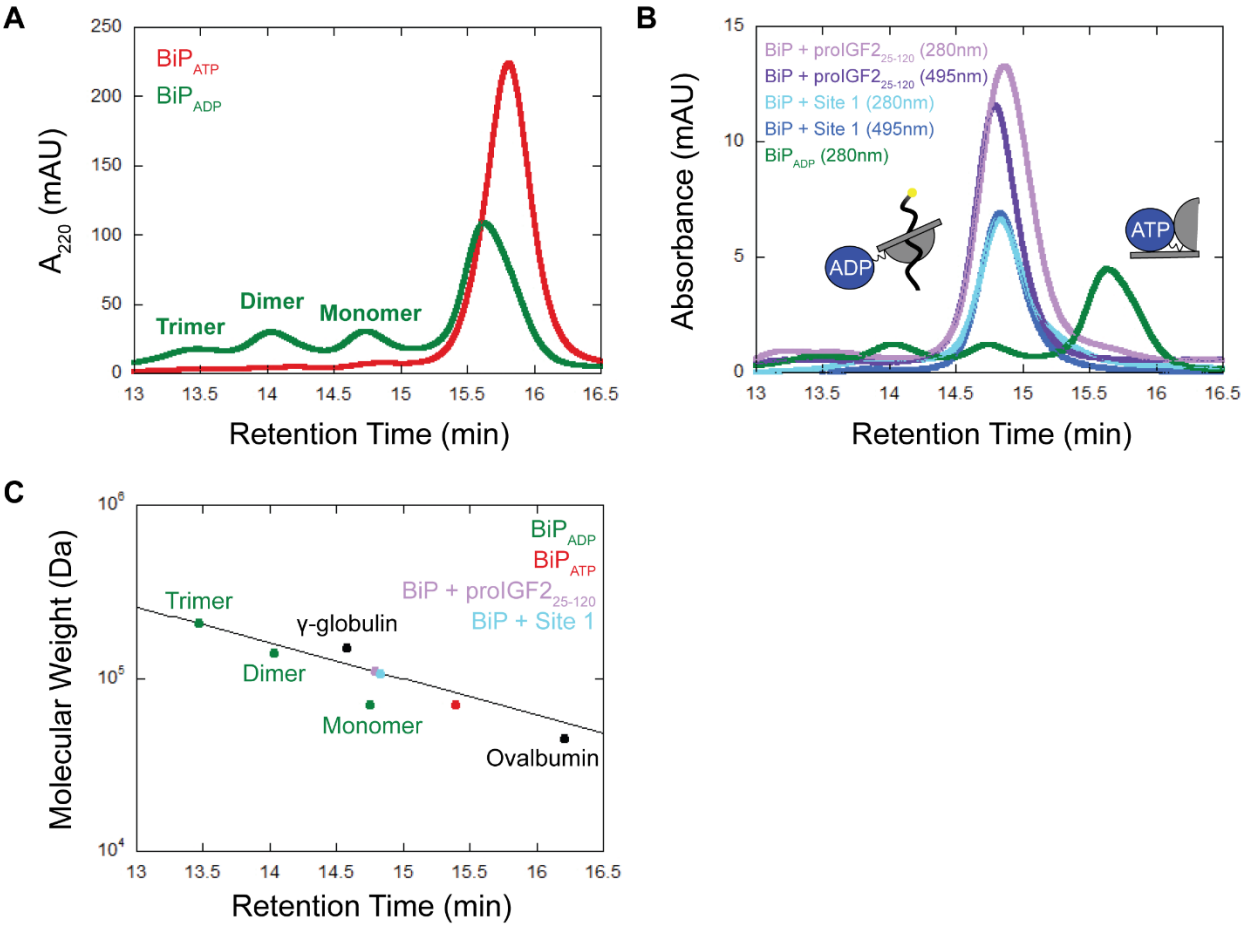

Figure 3.11. A. SEC elution profile of 5μM BiP with 0.1mM ATP (red) and 1mM ADP (green). Oligomeric states of ADP-bound BiP are labeled. **B.** Overlaid elution profiles of BiP (green), BiP + 5μM FITC-proIGF2$_{25\text{-}120}$ (dark purple and light purple), and BiP + 5μM FITC-site 1 (dark blue and light blue) under ADP conditions. **C.** Calibration curve of molecular weight versus retention time of standard proteins (black). Positions of BiP$_{ADP}$ oligomeric states (green), BiP$_{ATP}$ (red), BiP + FITC-proIGF2$_{25\text{-}120}$ (purple) and BiP + FITC-Site 1 (light blue) are indicated. Standard protein and BiP$_{ATP}$ data are the same as Figure 3.10.D.

1 constructs. ATP reduces BiP affinity for ext. site 1 by ~3-fold and the reduction for site 1 is ~6-fold (Figure 3.12.B-C). All three site 1 constructs have comparable BiP affinities under ADP conditions, but progressively weaker affinity under ATP conditions as the clients become shorter in length (Figure 3.12.D). This trend suggests that the ATP state of BiP may make weak transient interactions on multiple sites across the proIGF2$_{25\text{-}120}$ client that provide a modest enhancement of affinity. In contrast, the ADP state of BiP appears to only bind to site 1, resulting in the comparable BiP/client affinities observed under ADP conditions.

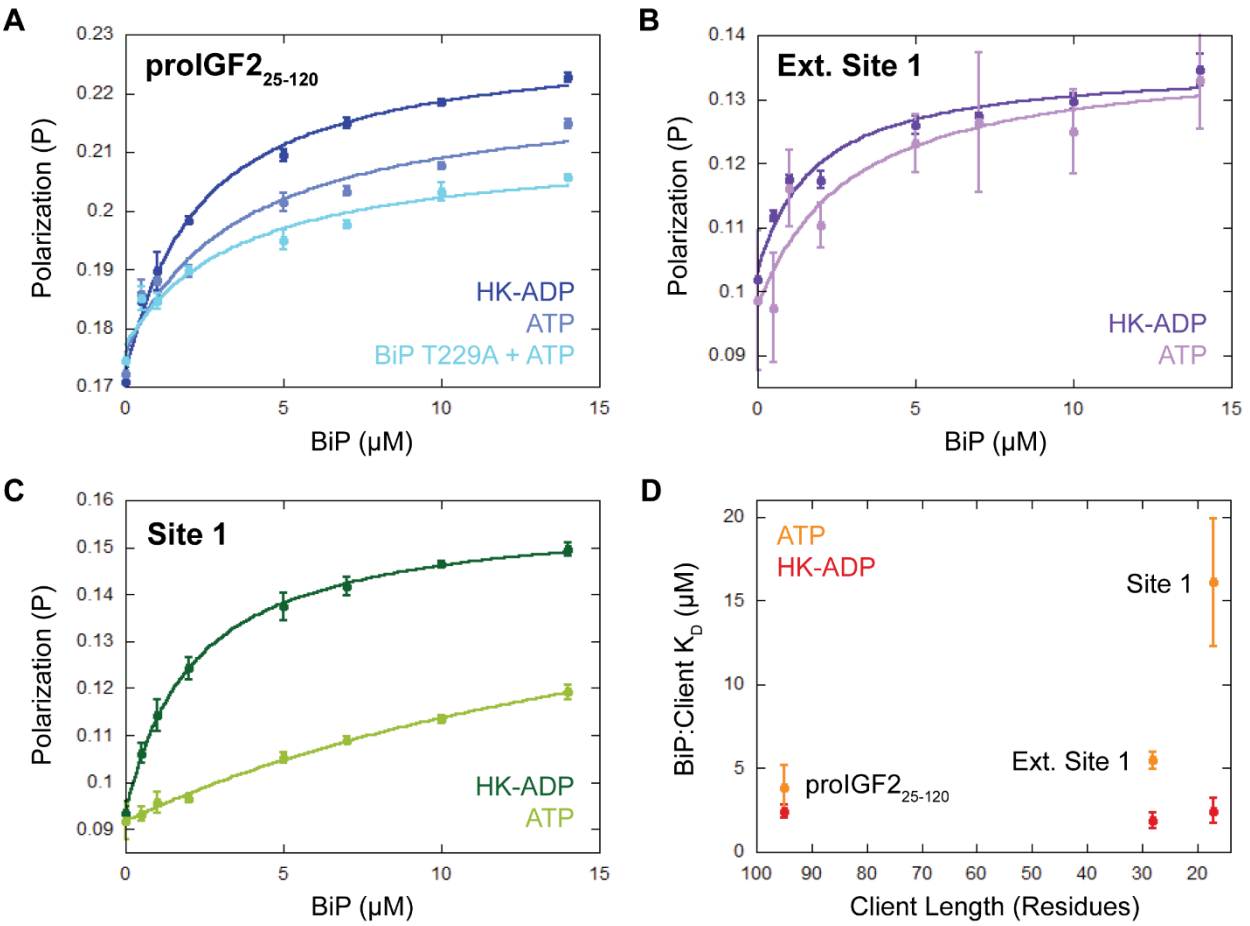

Figure 3.12. A-C. FP BiP binding assay with FITC-labeled clients. Solid lines are fit to Equation 7. (**A**) BiP affinity for proIGF2$_{25\text{-}120}$ is 2.5±0.4μM and 3.8±1.4μM under HK-ADP and ATP conditions respectively. Under ATP conditions the K_D of a hydrolytically inactive BiP mutant, BiP T229A, is 3.5±0.6μM. (**B**) BiP affinity for Ext. Site 1 is 1.9±0.5μM and 5.5±0.5μM under HK-ADP and ATP conditions respectively. (**C**) BiP affinity for Site 1 is 2.5±0.7μM and 16±3.8μM under HK-ADP and ATP conditions respectively. **D.** BiP affinities for clients of decreasing size under HK-ADP and ATP conditions. Client constructs include: proIGF2$_{25\text{-}120}$ (95 residues), ext. site 1 (28 residues), and site 1 (17 residues). Error bars are the SEM of three measurements.

ProIGF2$_{25\text{-}120}$ increases BiP ATPase (Figure 3.13.A), whereas removal of the site 1 region from proIGF2$_{25\text{-}120}$ results in no ATPase stimulation. To examine the contribution of BiP ATP hydrolysis to proIGF2$_{25\text{-}120}$ binding, we utilized the hydrolytically inactive BiP mutant, T229A[20] (Figure 3.12.A). Under ATP conditions the binding of BiP T229A to proIGF2$_{25\text{-}120}$ is only marginally weaker than for wild-type BiP. This suggests that BiP's relatively high affinity for proIGF2$_{25\text{-}120}$ under ATP conditions results from transient interactions with regions away from site

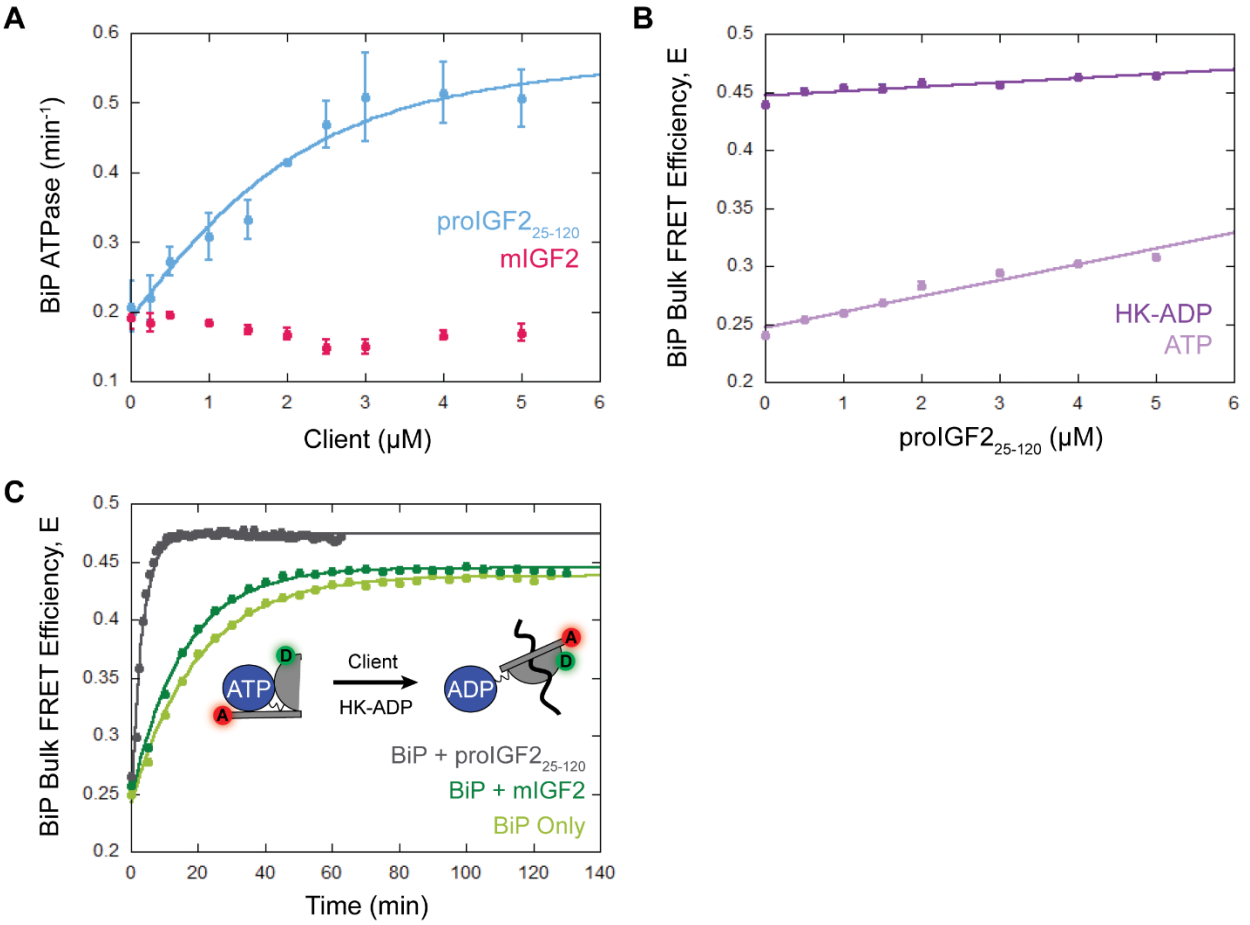

Figure 3.13. A. BiP ATPase rates with increasing concentration of proIGF2$_{25\text{-}120}$ and mIGF2. Solid line is a fit to Equation 2. **B.** BiP bulk FRET assay measuring lid closure with variable concentrations of proIGF2$_{25\text{-}120}$ under ADP and ATP conditions. Solid lines are linear fits. **C.** BiP bulk FRET assay measuring lid closure with and without client. Solid lines are a fit to a single exponential (closure rate with 5μM proIGF2$_{25\text{-}120}$: 0.3±0.01min^{-1}; 5μM mIGF2: 0.06±0.01min^{-1}; without client: 0.05±0.01min^{-1}). Closure is initiated by first equilibrating BiP with 0.1mM ATP and flushing in 1mM HK-ADP and client. Error bars are the SEM of three measurements. Errors on closure rates are the fitting error. (*Inset*) Cartoon shows schematic of BiP conformations and fluorophore positions.

1 and only when BiP encounters the site 1 region does the chaperone use ATP hydrolysis to bind proIGF2$_{25\text{-}120}$.

In the absence of a client protein, the BiP lid closes upon ATP hydrolysis, but some large clients (such as C_H1^{116}) appear to prevent lid closure. To determine the effect of proIGF2$_{25\text{-}120}$ on the BiP lid, we utilized the same FRET pair discussed in the introduction (Figure 3.13.C inset). An increase in FRET is observed under ATP conditions, indicating that BiP favorably binds

proIGF2$_{25\text{-}120}$ in a lid-closed state compared to a lid open state (Figure 3.13.B). The stabilization of the closed lid state is also evident in kinetic measurements where BiP lid closure is accelerated ~6-fold by proIGF2$_{25\text{-}120}$ whereas the removal of the site 1 region from proIGF2$_{25\text{-}120}$ results in no lid closure acceleration (Figure 3.13.C). With this framework for BiP binding proIGF2$_{25\text{-}120}$ in place, I next examined the BiP/Grp94/proIGF2$_{25\text{-}120}$ ternary complex.

3.3.4 proIGF2$_{25\text{-}120}$ Forms a Ternary Complex with BiP/Grp94

We first examined the binding of BiP and Grp94 to FITC-labeled proIGF2$_{25\text{-}120}$ with FP measurements. These measurements were performed under ADP conditions to focus specifically on the initial binding of BiP to Grp94 and client positioning prior to ATP-dependent closure of Grp94. Only the "ADP conformation" of BiP can bind to Grp94[12] and ADP prevents Grp94 conformational cycling, so the ADP condition enables measurements of the initial binding between BiP:client and Grp94. Grp94 has minimal affinity for proIGF2$_{25\text{-}120}$ as measured by FP (Figure 3.14.A), suggesting that the primary means of client delivery to Grp94 would be from BiP. The FP values are substantially larger for BiP/Grp94/proIGF2$_{25\text{-}120}$ compared to BiP/proIGF2$_{25\text{-}120}$, which is expected for the larger size of the ternary complex. The formation of a ternary complex relies the site 1 region of proIGF2$_{25\text{-}120}$ since FITC-labeled mIGF2 exhibits minimal binding to BiP and Grp94 and no ternary complex formation (Figure 3.14.B). The apparent affinity of proIGF2$_{25\text{-}120}$ to BiP/Grp94 is modestly reduced as compared to binding just BiP, but this should be interpreted cautiously because the FP signal likely has contributions from both BiP/client and BiP/Grp94/client species over the experimental concentration range.

BiP binding to proIGF2$_{25\text{-}120}$ exhibits slow binding kinetics (Figure 3.14.C). The kinetics of BiP/proIGF2$_{25\text{-}120}$ binding appear to saturate at BiP concentrations above 10μM, and the

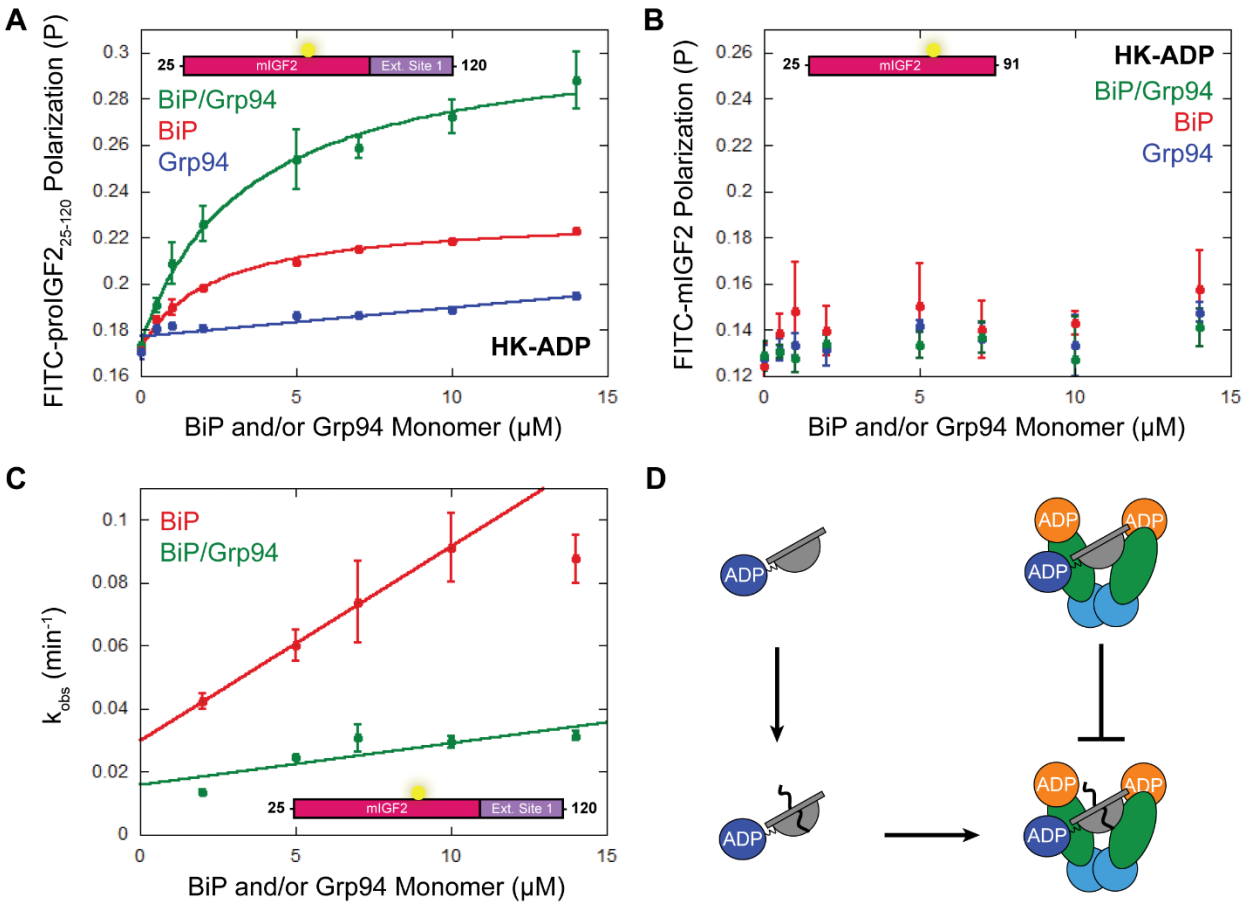

Figure 3.14. A. FP of FITC-labeled proIGF2$_{25-120}$ with varying concentrations of BiP (red), Grp94 (blue), and BiP and Grp94 (green). BiP/Grp94 data fit to Equation 7 ($K_{D,app}$ = 3.7±0.7μM). BiP only data is the same as in Figure 3.12.A (K_D = 2.5±0.4μM). Grp94 only data is a linear fit. **B.** FP of FITC-labeled mIGF2 with varying concentrations of BiP (red), Grp94 (blue), and BiP and Grp94 (green). **C.** Binding kinetics of FITC-labeled proIGF2$_{25-120}$ with varying concentrations of BiP (red) and BiP and Grp94 (green). Solid lines are linear fits (BiP: k_{on}=0.006±0.001μM^{-1}min^{-1}, k_{off}=0.030±0.002min^{-1}; BiP and Grp94: k_{on}=0.0013±0.0002μM^{-1}min^{-1}, k_{off}=0.016±0.001min^{-1}). Error bars are the SEM of at least two replicates. **D.** BiP is unable to bind client when in complex with Grp94. Instead, BiP binds client first, then BiP:client binds Grp94 to form a ternary complex.

microscopic rate constants (k_{on} and k_{off}) were determined from k_{obs} values at or below this concentration. The binding kinetics could be saturating due to binding being dependent on a BiP conformational change, such as lid opening, or the monomer concentration of BiP saturating at higher concentrations due to oligomerization. Regardless, the association and dissociation rate constants for BiP/proIGF2$_{25-120}$ binding are roughly similar to the rates reported for BiP binding the C_H1 domain[116] (k_{on}=0.001±0.0002μM^{-1}min^{-1}; k_{off}=0.01±0.002min^{-1}).

The association rate of proIGF2$_{25\text{-}120}$ slows ~5-fold upon the addition of Grp94 (Figure 3.14.C). In these experiments, BiP, Grp94, and proIGF2$_{25\text{-}120}$ are added at the same time. The association rate of BiP/proIGF2$_{25\text{-}120}$ is much slower than that of BiP/Grp94, so BiP/Grp94 will form complexes prior to client binding to BiP. The decrease in association rate for BiP/Grp94/proIGF2$_{25\text{-}120}$ in Figure 3.14.C indicates BiP is unable to bind client when in complex with Grp94 and instead that BiP must bind client prior to binding Grp94 (Figure 3.14.D). Therefore, we next designed an FP assay to measure the binding affinity of BiP:client to Grp94.

To measure binding of BiP:client to Grp94 we utilized a previously described FITC-labeled BiP construct[12]. Because BiP (~70kDa) is larger than proIGF2$_{25\text{-}120}$ (~11kDa) a minimal FP contribution from the client is expected, and, indeed, this is what is observed (see zero point in Figure 3.15.A). In the absence of client, BiP and Grp94 bind with sub-micromolar affinity, as has been described previously[12]. In the presence of proIGF2$_{25\text{-}120}$, the affinity between BiP and Grp94 decreases (Figure 3.15.A).

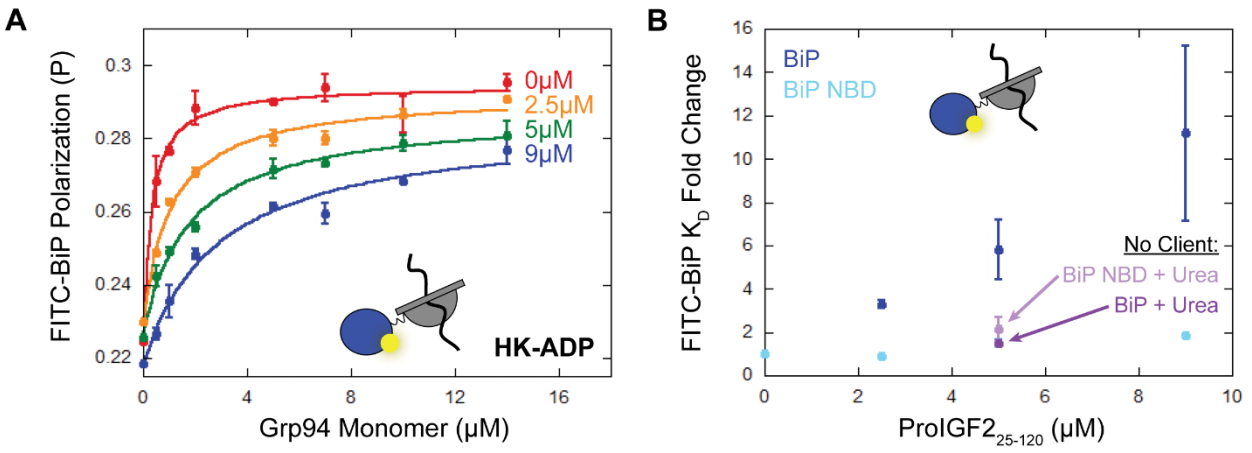

Figure 3.15. A. FP of FITC-labeled BiP with varying concentrations of Grp94, each with different concentrations of proIGF2$_{25\text{-}120}$: 0μM (red, K_D=0.3±0.1μM), 2.5μM (orange, $K_{D,app}$=1.1±0.1μM), 5μM (green, $K_{D,app}$=1.9±0.4μM), and 9μM (blue, $K_{D,app}$=3.6±1.3μM). Solid lines are a fit to Equation 7. K_D values are reported in Grp94 monomer concentration. Error bars are the SEM of three replicates. **B.** Fold reduction of BiP binding affinity from panel A. Binding affinities for FITC-BiP and Grp94 (dark purple) and FITC-BiP NBD and Grp94 (light purple) without client but with matching urea concentrations are indicated. Error bars are the propagated error from three replicates.

The reduction of BiP affinity to Grp94 in the presence of proIGF2$_{25\text{-}120}$ could have many contributions. One possible contribution is that non-specific binding between proIGF2$_{25\text{-}120}$ and Grp94 interferes with BiP NBD binding to Grp94. We tested this possibility by measuring the binding of the isolated BiP NBD to Grp94 with the same concentrations of proIGF2$_{25\text{-}120}$ as used with full-length BiP. ProIGF2$_{25\text{-}120}$ has a minimal influence on BiP NBD binding affinity (Figure 3.15.B), so we can exclude this possible confounding factor. A second potential factor is that proIGF2$_{25\text{-}120}$, which is purified from an inclusion body, is stored in denaturant and therefore experiments performed with proIGF2$_{25\text{-}120}$ introduce urea into the buffer conditions (see Methods). We can also exclude this as a confounding factor because the addition of urea equivalent to 5μM proIGF2$_{25\text{-}120}$ has only a modest influence on both BiP/Grp94 and BiP NBD/Grp94 affinity (purple data points in Figure 3.15.B). More work is needed to determine the cause of the reduced BiP affinity to Grp94 due to proIGF2$_{25\text{-}120}$.

We next examined the conformation of Grp94 in BiP/Grp94/proIGF2$_{25\text{-}120}$ ternary complexes. Figure 3.16 compares smFRET efficiency histograms for WT/K467A Grp94 heterodimers and 2μM BiP, with and without 5μM proIGF2$_{25\text{-}120}$. This concentration of proIGF2$_{25\text{-}120}$ is two-fold over the K_D (2.5±0.4μM), therefore the majority of BiP will be bound to client. In the presence of proIGF2$_{25\text{-}120}$, the C' state population is reduced (Figure 3.16.B). This shift in the Grp94 conformational equilibrium is expected due to the loss of BiP affinity when bound to proIGF2$_{25\text{-}120}$. The presence of proIGF2$_{25\text{-}120}$ decreases BiP/Grp94 affinity ~6-fold so 2μM BiP is roughly at the apparent K_D. A higher concentration of BiP and proIGF2$_{25\text{-}120}$ in similar smFRET experiments may help top clarify what conformation of Grp94 is favored when bound to both BiP and client.

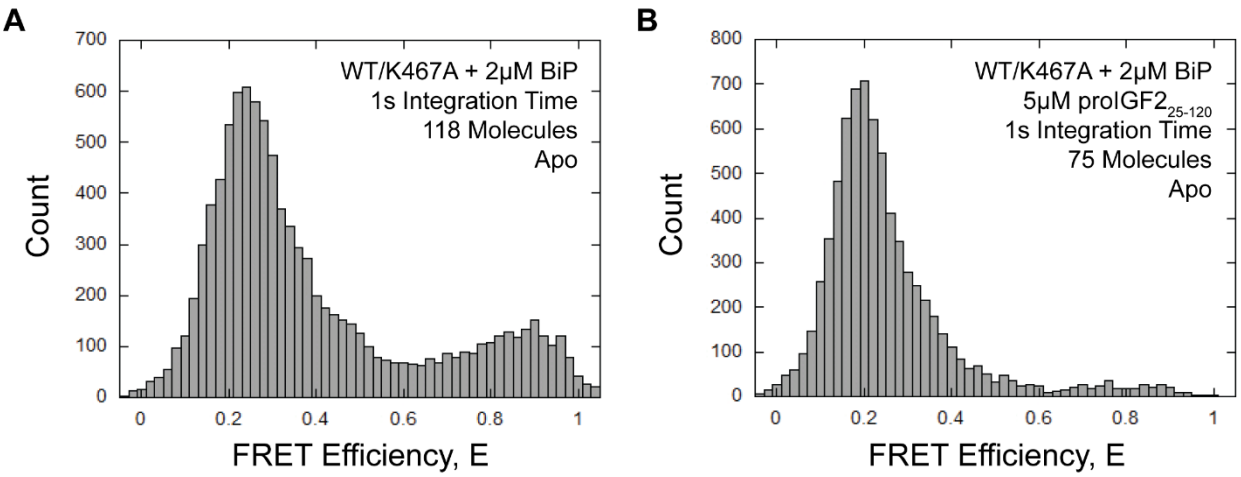

Figure 3.16. smFRET efficiency histograms for WT/K467A Grp94 heterodimers in the absence (**A**) and presence (**B**) of 5μM proIGF2$_{25\text{-}120}$. Data in panel A is the same as Figure 3.5.B. Data collected at an integration time of 1s (520μW at 532nm, 150μW at 633nm).

3.4 Discussion

Mounting evidence indicates Hsp70/Hsp90 pairs have a conserved chaperoning function that is dependent on a conserved interaction interface that enables the two chaperones to function as a concerted unit[8–12]. The structural and mechanistic details of the joint chaperoning function remain an active area of research. The loading structure provided new structural insights into cytosolic Hsp70/Hsp90 coordinated function and validated previous observations made with other Hsp70/Hsp90 pairs. For example, the loading structure validates not only the interacting domains but also the specific residues responsible for bridging Hsp70 and Hsp90 at interface I. Additionally, the loading structure confirms that Hsp70 and Hsp90 can only associate when Hsp70 is in the ADP conformation. Beyond this, it is unclear how relevant the mechanistic insights from the loading structure are to other Hsp70/Hsp90 systems, specifically systems which lack Hop (bacterial Hsp70/Hsp90 and those in organelles). Here, we examined questions raised by the loading structure for the BiP/Grp94/proIGF2 system.

3.4.1 Part 1: Stoichiometry of BiP on Grp94

The proposed client loading mechanism (Figure 3.1) raised three questions about BiP:Grp94 stoichiometry. The first question is what BiP stoichiometry is necessary to accelerate ATP-dependent closure of Grp94. The loading structure shows two Hsp70s symmetrically bound to Hsp90α[13], but the observation of BiP accelerating Grp94 closure was made under conditions which allowed one or two BiPs to bind Grp94[80]. By using a Grp94 heterodimer in which only one BiP can bind (WT/K467A), we discover a single BiP is sufficient to accelerate Grp94 closure (Figure 3.4.A-B).

The second question is whether BiP specifically stimulates Grp94 ATP hydrolysis on the arm in which it is bound, or whether ATP hydrolysis can occur on both arms. BiP enhances the ATPase of E103A/K467A heterodimers to a similar extent as WT/K467A heterodimers (Figure 3.4.A), meaning Grp94 ATP hydrolysis can occur on either or both arms and is not specific to the arm in which BiP is bound.

The third question is whether Grp94 adopts different conformations when one or two BiPs are bound. We find that one and two bound BiPs yield similar Grp94 conformations (open and C', Figure 3.5), but a different conformational equilibrium between these states is observed depending on the number of BiPs bound. A single bound BiP is sufficient to drive Grp94 into the C' state, and this state is further stabilized with a second BiP bound.

A functional stoichiometry of one BiP per Grp94 dimer avoids a puzzle posed by the loading structure. Specifically, what would happen if two client-bound BiPs are bound to Grp94? This situation could create steric interference between the chaperones and limit the possible conformations each chaperone can adopt, potentially disrupting the function of both BiP and Grp94. Further, two clients would either be competing for binding in the Grp94 cleft or Grp94

could end up binding two clients. At this time there is no evidence that Hsp90s can bind more than one client simultaneously.

It is unclear from the loading structure whether the 2:1 stoichiometry was achieved because it is the required stoichiometry for client transfer or if the second Hsp70 bound simply because of how the complex was formed. The loading structure was acquired using an ATP-binding deficient mutant of Hsp90 and was stabilized through glutaraldehyde crosslinking, which would collectively prevent Hsp90 from fully closing. Additionally, the loading structure represents only a small fraction of the particles analyzed, other particles demonstrated conformational heterogeneity at all regions of the complex. Our results show BiP and Grp94 form 2:1 stoichiometries without the use of crosslinking, and this stoichiometry stabilizes the C' state of Grp94 to a greater extent than a single bound BiP. This supports the previously proposed cooperative binding between BiP and Grp94[80]. Since a single bound BiP is sufficient to drive Grp94 into the high affinity C' state, BiP and Grp94 fit into a cooperative binding model conceptually similar to the Monod-Wyman-Changeux (MWC) explanation for cooperative binding of oxygen to hemoglobin. Specifically, binding of the first BiP is enough to push a small population of Grp94 from the low affinity open state (tense or T state in the MWC model) to the C' state (relaxed or R state in MWC model). The second BiP can then bind to the C' state with high affinity, further shifting the Grp94 conformational equilibrium to favor this state.

Under ATP conditions, a stoichiometry of two BiPs per Grp94 dimer can only be achieved if there is sufficient time for both BiPs to bind before Grp94 closes. BiP binding accelerates ATP-dependent closure of Grp94 ~50-fold, shortening the mean lifetime (τ) of the open state from ~6 minutes to ~7.7 seconds[80]. The loading complex mechanism in Figure 3.1 assumes the semi-closed conformation of Hsp90α is a long-lived state. In contrast, the C' conformation of Grp94 is a short-

lived intermediate state under ATP conditions (τ~2.1 seconds)[80]. Taken together, Grp94 closes within ~10 seconds when BiP is bound, meaning a 1:1 stoichiometry may be the predominant means of Grp94 closure under biological conditions in which the concentration of BiP in the ADP conformation is low. However, in the cytosolic Hsp70/Hsp90 system, Hop slows Hsp90 closure rates by stabilizing the open state. The presence of Hop would promote cooperativity by making it harder for Hsp90 to completely close, but still allowing the formation of the semi-closed conformation. In Hsp70/Hsp90 systems which lack Hop, does Hsp70 or another co-chaperone function to slow down Hsp90 closure and promote cooperativity? This idea will be discussed further in the next section.

3.4.2 Part 2: The BiP SBD Stabilizes the BiP/Grp94 Complex

The loading complex shows Hop positioning GR within the Hsp90α binding cleft. This raises the question of how client proteins are positioned in Hsp70/Hsp90 systems that lack Hop. By designing a new $Grp94_D$/BiP SBD_A smFRET assay I discovered the BiP SDB populates two configurations when BiP is bound to Grp94 (Figure 3.8.B, and 3.9.A-B). Using a previously established FP assay[12] with Grp94 truncations I found the BiP SBD makes a stabilizing contact with the CTD on the same arm in which BiP is bound (Figure 3.7.A). Mutation of amphipathic helix residues which interact with Hop in the loading complex structure only modestly altered the affinity between BiP and Grp94 (Figure 3.7.A).

Based on the location of the donor fluorophore on Grp94 in $Grp94_D$/BiP SBD_A smFRET (A610C), the CTD binding interface likely corresponds to the high FRET SBD configuration (ε~0.7). Even though the amphipathic helix mutants only modestly affected BiP/Grp94 affinity, this region could still be the location of the CTD binding interface. Since the BiP SBD forms two

stable contacts with Grp94, disruption of one of these interactions would cause the SBD to preferentially bind at the other site. Because of this, bulk binding assays would likely not report a large decrease in BiP/Grp94 affinity. Future studies could utilize the amphipathic helix mutants in the $Grp94_D$/BiP SBD_A smFRET assay to determine if this is the case. If these mutations disrupt one of the SBD interaction sites, the FRET efficiency distribution would shift to favor the other SBD configuration.

Currently, we have no bulk data to suggest the location of the low FRET SBD configuration (ε~0.35). One possibility is the BiP SBD makes a stabilizing contact with the Grp94 arm adjacent to the one in which BiP is bound. SBD binding to the adjacent Grp94 arm can be tested by measuring monomer exchange kinetics of Grp94 in the presence of BiP and BiP NBD. If the SBD binds to the adjacent arm, Grp94 should exhibit slower exchange kinetics compared to Grp94 alone or Grp94 with BiP NBD.

The discovery of BiP SBD docking to Grp94 opens up new questions. In the cytosolic Hsp70/Hsp90 system, Hop and other co-chaperones regulate the rate of Hsp90 conformational cycling. Does the binding of the SBD affect Grp94 conformational cycling, specifically by slowing down Grp94 closure? Previous literature reports a rate of ~8 min^{-1} for open to C' transitions with saturating BiP[80]. However, this rate is calculated based on parameters from smFRET experiments with non-saturating BiP. The actual rate with saturating BiP has not been experimentally determined, meaning it could be faster than the reported ~8 min^{-1}. Future studies are needed to determine the rate of open to C' transitions in the presence of saturating BiP, and subsequently determine how the presence of the SBD affects this rate. Building on this, how does bound client effect the BiP SBD stabilization of BiP:Grp94 complexes? This question will be discussed in further detail in the next section.

3.4.3 Part 3: BiP Can Bind a Monomeric Fragment of proIGF2 and Form Ternary Complexes with Grp94

Designing a large monomeric fragment of proIGF2 is critical for BiP/Grp94 mechanistic analysis of client transfer. Here, I designed a proIGF2 truncation which removes the E-peptide region past site 1, proIGF2$_{25\text{-}120}$, which meets the necessary criteria. This client is large (95 residues), primarily monomeric, unable to fold, and maintains the micromolar BiP affinity characteristic of peptide clients[116,132]. SEC shows that a single BiP binds to proIGF2$_{25\text{-}120}$ (Figure 3.11.B-C). ProIGF2$_{25\text{-}120}$ also stimulates BiP ATPase, similar to small peptide clients[148] (Figure 3.13.A). This contrasts the observed deceleration of BiP ATPase with the large C_H3 domain[145]. Further, equilibrium and kinetic BiP bulk FRET measurements show BiP binds proIGF2$_{25\text{-}120}$ in a lid-closed state similar to short peptide clients (Figure 3.13.B-C). This result contrasts the proposed lid-open state of BiP when binding the C_H1 domain[116]. BiP appears to bind proIGF2$_{25\text{-}120}$ similarly to short peptide clients under ADP conditions, despite its size being comparable to full-length clients. However, the α-helical lid of Hsp70s is an essential component for functional interactions with clients[116,149,150], and Hsp70s may adopt different modes of binding depending on the client.

Collectively, our results with proIGF2$_{25\text{-}120}$ support a model in which BiP binding client and BiP/Grp94/client ternary complex formation are both reliant on the site 1 region (Figure 3.17). Under ADP conditions, proIGF2$_{25\text{-}120}$, ext site 1, and site 1 all have similar binding affinities to BiP. In contrast, under ATP conditions, proIGF2$_{25\text{-}120}$ exhibits the highest BiP affinity and the affinities of other site 1 constructs progressively decrease as a function of client length (Figure 3.12.D). This suggests the ATP state of BiP makes weak transient interactions across proIGF2$_{25\text{-}120}$ and ATP hydrolysis occurs when BiP encounters the site 1 region (Figure 3.17). This idea is strengthened when proIGF2$_{25\text{-}120}$ is compared to a client which lacks the site 1 region, mIGF2.

mIGF2 minimally binds to BiP and does not stimulate BiP ATPase or lid closure (Figure 3.13.A and C, 3.14.B).

Once BiP is prepared to transfer client, I hypothesize two different BiP/Grp94/client complexes will form based on cellular conditions (Figure 3.17). Under homeostatic conditions, the majority of BiP in the ER will be in the ATP-state unless it is bound to client. The concentration of monomeric, ADP-state BiP will be limited compared to Grp94. Because of this, BiP/Grp94 would utilize a 1:1 stoichiometry for client transfer. First, a single client-bound BiP drives Grp94 into the C' state (Figure 3.17, homeostasis step 1). The client is positioned in the Grp94 binding cleft, BiP dissociates, and Grp94 fully closes (homeostasis step 2).

I predict that proIGF2 will disrupt SBD docking on Grp94 (double sided curved arrows in Figure 3.17). This would likely cause proIGF2 to be presented to Grp94 in a wide variety of configurations, which may be advantageous. BiP and Grp94 work on an array of clients, SBD conformational heterogeneity allows individual clients to be positioned in optimal configurations within the binding cleft instead of limited to one or two configurations if the SBD was docked. However, given Grp94 closes within ~10 seconds of BiP binding[80], optimal positioning of a client would need to occur within this timeframe in order for transfer to successfully occur. Without an additional co-chaperone to slow down Grp94 closure or stabilize the transfer state (such as Hop in the cytosolic Hsp70/Hsp90 system), optimal client positioning is less likely to occur in time. In this case, BiP is more likely to dissociate from Grp94 still bound to client and client transfer would be less efficient.

Under stressed conditions, where successful client transfer is more critical, BiP and Grp94 will utilize a 2:1 stoichiometry for transfer (Figure 3.17). During cell stress, the majority of BiP in the ER will be in the ADP-state due to the increased concentration of unfolded proteins. The

concentration of monomeric, ADP-state BiP will be in excess compared to Grp94. Because of this, a BiP which is not bound to a client can bind to Grp94 first (Figure 3.17, stress step 1). Since the BiP SBD can bind to Grp94 in the absence of client (Figure 3.8.B and 3.9.A-B), I hypothesize the BiP SBD in this step will act similarly to Hop in the cytosolic Hsp70/Hsp90 system. Specifically, SBD binding will promote cooperativity by slowing down Grp94 closure while still allowing the formation of the C' state. From here, a client-bound BiP can bind to Grp94 with high affinity (Figure 3.17, stress step 2). This client has a longer timeframe to be optimally positioned within the Grp94 binding cleft since the first BiP stabilizes the C' state, increasing the efficiency of transfer. Once the client is positioned, both BiPs dissociate and Grp94 fully closes (stress step 3).

This model is dependent on the SBD stabilization of BiP/Grp94 complexes being disrupted in the presence of client. The FP measurements of BiP:proIGF2$_{25\text{-}120}$ binding to Grp94 in Figure 3.15.A attempt to answer this question, but we do not have enough evidence to conclude the decrease in BiP/Grp94 affinity is due to loss of SBD stabilization. The presence of client and urea does not affect BiP/Grp94 interaction at interface I. If the decrease in affinity is caused by disruption of SBD binding, the K_D should plateau roughly around the K_D of BiP NBD/Grp94 at high concentrations of proIGF2$_{25\text{-}120}$. The enhancement to BiP/Grp94 affinity due to SBD binding would be gone, leaving only the interaction at interface I. However, the decrease in BiP/Grp94 affinity does not saturate within the range of proIGF2$_{25\text{-}120}$ concentrations tested (Figure 3.15.B). If proIGF2$_{25\text{-}120}$ could be stored in lower concentrations of urea or diluted/dialyzed out of the 8M urea storage buffer, then higher concentrations could be tested. Additionally, the conformation of Grp94 in BiP/Grp94/client ternary complexes cannot be reliable determined from the smFRET results in Figure 3.16.B. Future studies could include a fluorescent-label on proIGF2$_{25\text{-}120}$ to ensure only Grp94 molecules bound to BiP and client are being analyzed.

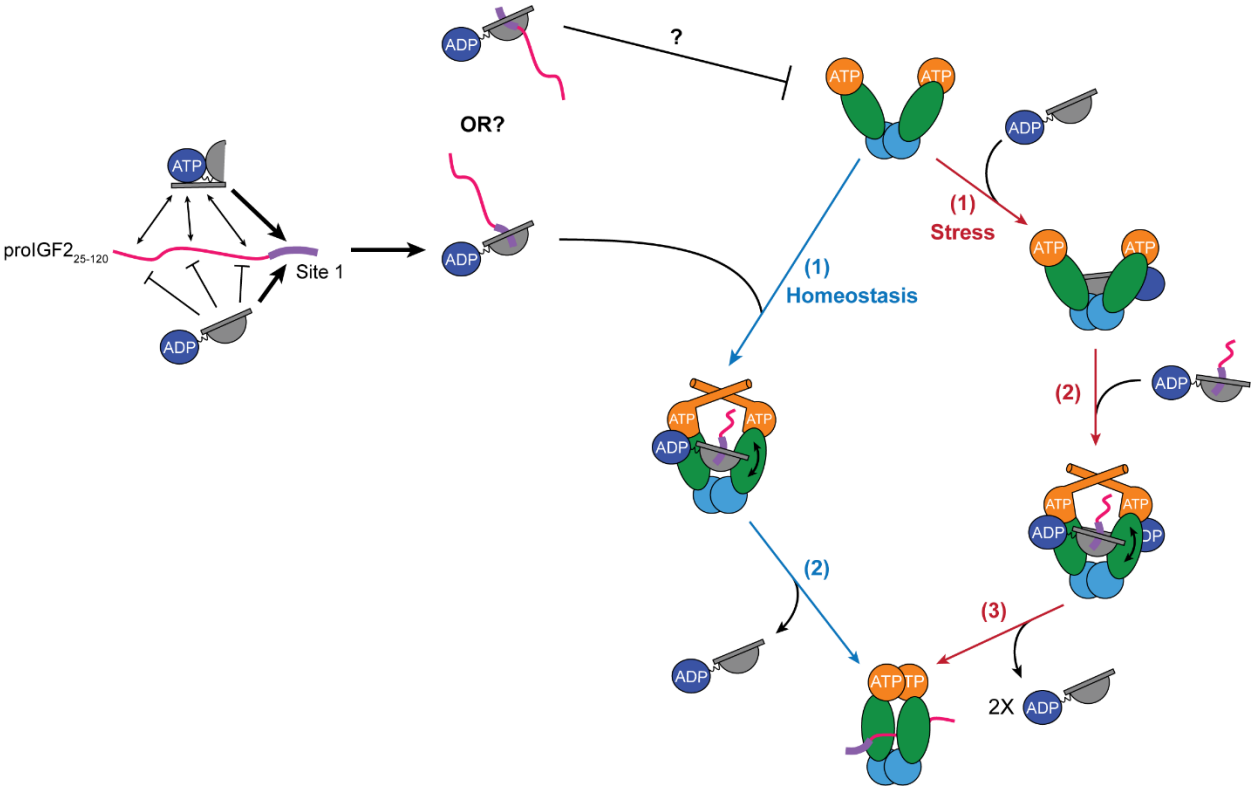

Figure 3.17. Proposed model of BiP binding proIGF2$_{25-120}$ and client transfer with Grp94. For proIGF2$_{25-120}$, the mIGF2 region is shown in pink and the site 1 region is bolded and shown in purple. Question mark denotes the unknown orientation of BiP and Grp94 binding to proIGF2$_{25-120}$.

An open question is the orientation of proIGF2$_{25-120}$ when bound to BiP, and whether Grp94 prefers a specific client orientation (indicated by question mark in Figure 3.17). Hsp70s can bind most client proteins in both the N-to-C or C-to-N orientations[33], so BiP may bind proIGF2$_{25-120}$ heterogeneously. If Grp94 has a preference for client orientation, only a fraction of BiP:client would be able to form ternary complexes with Grp94. These open questions could be tested with smFRET. Fluorescently-labeled proIGF2$_{25-120}$ can be tethered to the surface of a microscope slide and fluorescently-labeled BiP can be added to bind to the client. The Y636C labeling position on the BiP α-helical lid is close to the binding cleft, and depending on the orientation of BiP binding will produce different FRET signals. Fluorescently-labeled Grp94 can also be added to this experimental setup to determine whether Grp94 binds better when BiP is bound to the client in either the N-to-C or C-to-N orientation.

3.5 Methods

Protein Expression and Purification

Mouse Grp94 (72-765) with the charge-linker removed (Δ287-328) was truncated to make the NM Grp94 fragment (Δ595-765) and $Grp94_{monomer}$ fragment (Δ725-765). These Grp94 constructs, the Grp94 variants (N91C, E103A, K467A, A610C, W654A, M662A, N91C/K467A), BiP (27-655), the BiP variants (D27C, T229A, G518C, G518C/Y636C), BiP NBD (27-411), and the BiP NBD variants (D27C, T229G/G227D) were all expressed in *E. coli* BL21 cells in pET151D vectors which contain a 6X His-tag and TEV cleavage site. All proteins were first purified by Ni-NTA affinity chromatography and the 6X His-tag was cleaved with TEV. Subsequent Ni-NTA affinity chromatography removed 6X His-tag and TEV and anion exchange chromatography removed bound nucleotide. Proteins were buffer exchanged with size exclusion chromatography into storage buffers. Grp94 constructs were stored in 25mM Tris pH 7.5, 75mM KCl, 1mM 2-Mercaptoethanol (BME), and 5% Glycerol. BiP and BiP NBD constructs were stored in 25mM Tris pH 7.5, 50mM KCl, 1mM BME, and 5% Glycerol[49]. The N91C and N91C/K467A Grp94 variants were labeled with Alex Fluor 555 (donor) and Alexa Fluor 647 (acceptor) as previously described[85]. The D27C variant of BiP and BiP NBD was labeled with FITC as previously described[12].

For $proIGF2_{25\text{-}120}$ and mIGF2, the mature IGF2 region was mutated to remove all cysteines except Cys70. E-peptide and Ext. Site 1 contain an N-terminal 6X His-tag and cysteine mutation at Ser95. $ProIGF2_{25\text{-}125}$, mIGF2, E-peptide, and Ext. Site 1 were all expressed in *E. coli* BL21 cells and purified from inclusion bodies. Briefly, inclusion bodies were washed and insoluble protein was denatured in 8M urea, 25mM Tris buffer containing reducing agent TCEP. Protein was purified by ion-exchange chromatography and/or Ni-NTA affinity chromatography in denaturing

conditions. Proteins were stored denatured in buffer containing 8M urea. Proteins used in HPLC or FP assays were labeled with FITC-maleimide with excess dye being removed by buffer exchange or ion exchange chromatography. FITC-labeled site 1 was synthesized by Alan Scientific (Gaithersburg, MD). Site 1 was N-terminally labeled with FITC via an amino hexanoic acid linker.

ATPase Assay

Grp94 ATPase measurements utilize the hydrolytically inactive T229G/G227D BiP NBD variant[151]. Grp94 ATPase was measured by depletion of NADH via an enzyme-linked assay with pyruvate kinase and lactate dehydrogenase on a plate reader (BioTek)[152]. NADH depletion was monitored at an absorbance of 340nm. 2μM Grp94 dimer was assayed in 25mM Tris pH 7.5, 50mM KCl, 1mM ATP, 1mM $MgCl_2$, 2mM BME, 0.1μM Lactate Dehydrogenase, 0.1μM Pyruvate Kinase, 0.4mM PEP, and 0.4mM NADH at 35°C. Grp94 heterodimers were formed by mixing 1μM of each Grp94 construct and incubating at 30°C for 2 hours to monomer exchange prior to starting measurements. The ATPase rate is reported per dimer of Grp94. Since monomer exchange is not fully efficient, the heterodimer sample represents a mixture of heterodimers and homodimers. The heterodimer ATPase (A_{het}) was calculated using

$$A_{het} = \frac{A_{measured\ het} - (A_{homodimer1} \times 0.25) - (A_{homodimer2} \times 0.25)}{0.5} \qquad (1)$$

Where $A_{measured\ het}$ is the measured ATPase for a 1:1 mixture of two different Grp94 variants, and $A_{homodimer1}$ and $A_{homomdimer2}$ are the measured ATPase values for the individual homodimers.

BiP ATPase was measured using the enzyme-coupled assay described above and 2μM BiP. Buffer conditions consist of 60mM HEPES pH 7.0, 50mM KCl, 1mM ATP, 1mM $MgCl_2$, 0.1μM Lactate Dehydrogenase, 0.1μM Pyruvate Kinase, 0.4mM PEP, and 0.4mM NADH at 37°C. The concentration of urea was kept constant in ATPase measurements titrating $proIGF2_{25\text{-}120}$ and

mIGF2. ATPase measurements including proIGF2$_{25\text{-}120}$ (A) were fit with a saturating binding equation

$$A = c + d\frac{[B + x + K_D] - \sqrt{[B + x + K_D]^2 - 4[B]x}}{2[B]} \quad (2)$$

Where *c* is the ATPase in the absence of client, *d* is the ATPase amplitude, *x* is the concentration of proIGF2$_{25\text{-}120}$, K_D is the dissociation constant between BiP and proIGF2$_{25\text{-}120}$, and *B* is the concentration of BiP used in the experiments.

Grp94 Bulk FRET

Grp94 bulk experiments were started by mixing 125nm donor-labeled and 125nm acceptor-labeled Grp94 in 25mM Tris pH 7.5, 50mM KCl, 1mM $MgCl_2$, 0.5mg/mL bovine serum albumin (BSA) and 2mM BME at 30°C for 2 hours to monomer exchange. Closure kinetics were initiated with 1mM ATP in the presence or absence of BiP NBD. Bulk FRET data was collected with a Fluoromax-4 spectrofluorometer (Horiba Scientific) with a donor excitation wavelength of 530nm and donor and acceptor emission wavelengths of 565nm and 670nm respectively. Slit widths were set to 1.5nm for excitation and 4.5nm for emission. Bulk FRET efficiency (E) was calculated by the donor (D) and acceptor (A) emission fluorescence

$$E = \frac{A}{(D + A)} \quad (3)$$

For equilibrium Grp94 FRET, $K_{D,app}$ values were calculated using a single-site binding equation

$$E = \frac{a[x]}{K_{D,app} + [x]} \quad (4)$$

Where *a* is the FRET efficiency amplitude and *x* is the concentration of added BiP NBD. All data points were from multiple separate experiments, each with a different concentration of BiP NBD.

BiP Bulk FRET

The G518C/Y636C BiP variant was labeled with Alexa Fluor 555 (donor) and Alexa Fluor 647 (acceptor) as previously described[12]. Fluorescently labeled BiP was diluted to 50nM in 60mM HEPES pH 7.0, 50mM KCl, 1mg/mL BSA, and 1mM DTT. For experiments with ATP, 1mM ATP and 1mM $MgCl_2$ was used. For experiments with ADP, BiP is first incubated with 0.1mM ATP and 0.1mM $MgCl_2$ then 1mM hexokinase-treated ADP is flushed in. ADP is hexokinase-treated with 0.005units/μL hexokinase, 1mM glucose, and 5mM $MgCl_2$ at 37°C for 1 hour. The concentration of urea was kept constant in FRET measurements titrating $proIGF2_{25-120}$. FRET data was collected with a Fluoromax-4 spectrofluorometer (Horiba Scientific) with a donor excitation of 532nm and donor and acceptor emission wavelengths of 567nm and 668nm respectively. Slit widths were set to 4nm for both excitation and emission with an integration time of 0.5 seconds at 30°C. FRET efficiency was calculated with Equation 3. For equilibrium BiP FRET, all data points were from multiple separate experiments, each with a different concentration of $proIGF2_{25-120}$.

Single Molecule FRET

For Grp94 smFRET, Grp94 with a C-terminal SNAP-tag was selectively biotinylated using a benzyl-guanine derivative as described previously[85]. Acceptor-labeled SNAP-Grp94 and donor-labeled Grp94 were monomer exchanged in 50mM HEPES pH 8.0, 50mM KCl, 0.6mM $MgCl_2$, 2mM BME, and 0.5mg/mL BSA at 30°C for 2 hours. Glass slides and coverslips were prepared as previously described[85]. Grp94 was applied to the slide after dilution to 1nM with an oxygen scavenging system (0.4% Glucose, 1.5units/μL Catalase, 0.04units/μL Glucose Oxidase) and triplet-state quencher cocktail (2mM Propyl Galate, 2mM 4-nitrobenzyl alcohol, 4mM Trolox).

BiP was then applied to the slide. For experiments with BiP and proIGF2$_{25\text{-}120}$, BiP was preincubated with proIGF2$_{25\text{-}120}$ for 2 hours at 30°C prior to being applied to the slide.

For Grp94$_D$/BiP SBD$_A$ smFRET, Grp94 A610C was labeled with Alexa Fluor 555 (donor) and BiP G518C was labeled with Alexa Fluor 647 (acceptor). Grp94 K467A with a C-terminal SNAP tag was selectively biotinylated as described above. K467A SNAP-Grp94 and donor-labeled Grp94 were monomer exchanged at a ratio of 3:1 in 50mM HEPES pH 7.0, 50mM KCl, 1mM $MgCl_2$, 0.5mg/mL BSA, and 2mM BME at 30°C for 2 hours. Acceptor-labeled BiP was incubated in 50mM HEPES pH 7.0, 50mM KCl, 1mM ADP, 1mM $MgCl_2$, and 1mg/mL BSA at 30°C for 2 hours. Glass slides and coverslips were prepared as discussed above. Prior to applying protein to the slide, donor-labeled Grp94/K467A SNAP-Grp94 heterodimers and acceptor-labeled BiP were incubated with 1mM ADP and 1mM $MgCl_2$ for 30 minutes at 30°C. The protein sample was applied to the slide after dilution with the oxygen scavenging system and triplet-state quencher cocktail. The concentration of donor-labeled Grp94 after dilution was 0.5nM.

Single molecule total internal reflection fluorescence (TIRF) imaging was performed on a custom microscope as described previously[85]. smFRET measurements include donor fluorophore excitation at 532nm, using laser powers dictated by the data integration time. Alternating excitation experiments include acceptor excitation with a laser power of 150μW at 633nm. All alternating excitation experiments have a sampling interval of 2.4 seconds with a signal integration time of 1 second.

In order for background fluorescence to be subtracted for both donor and acceptor signals, smFRET analysis was only performed on molecules with a recorded donor photobleaching event. FRET efficiency values were only calculated for time points where both the donor and acceptor fluorophores were not photobleached. For continuous excitation experiments, only molecules

which had an acceptor signal at the beginning and end of imaging were analyzed. The smFRET efficiency (E) was calculated as

$$E = \frac{A}{(\gamma \times D + A)} \quad (5)$$

Where *A* is the acceptor emission, *D* is the donor emission, and the γ value is 1.75 as determined by a previous analysis of Grp94[85]. For $Grp94_D$/BiP SBD_A smFRET, the smFRET efficiency was calculated with γ=1. The FRET efficiency histograms were constructed by compiling the efficiency values for each frame for each molecule. FRET efficiency histograms of $Grp94_D$/BiP SBD_A were fit to a one-state (for $Grp94_D$ only), two-state (for alternating excitation) or three-state (for continuous excitation) model

$$Count(E) = \Sigma_i \frac{A_i e^{\left(-(E-\varepsilon_i)^2/2\sigma_i^2\right)}}{\sigma_i\sqrt{2\pi}} \quad (6)$$

Where A_i is the histogram area associated with each state, ε_i is the mean FRET efficiency, and σ_i is the standard deviation. The third state in continuous excitation histograms were fixed at ε=0.1 and σ=0.09 based on the donor only FRET signal (Figure 3.9.C).

Analytical Size Exclusion Chromatography

The elution profile of FITC-proIGF2$_{25\text{-}120}$ was determined by diluting the client to concentrations between 1 and 8μM in HPLC Buffer (25mM Tris pH 7.5, 50mM KCl, 1mM $MgCl_2$). AdvanceBio SEC 300Å Protein Standards (Agilent Technologies) were used for molecular weight calculations. For samples including BiP, BiP was diluted to 5μM in HPLC Buffer with either 0.1mM ATP or 1mM ADP and 5μM FITC-labeled client where applicable. 10μL of each sample was injected onto an Agilent AdvanceBio SEC 300Å, 2.7-μm, 4.6 X 300-mm analytical SEC column pre-equilibrated with HPLC Buffer. Samples were run over the column at

a flow rate of 0.2mL/min. The protein standards were detected by absorbance at 280nm, BiP was detected by absorbance at 220 and 280nm, and FITC-labeled client was detected by absorbance at 220 and 495nm. The ratio between proIGF2$_{25\text{-}120}$ elution peaks was calculated by dividing the integrated peak areas, which were determined using the Agilent OpenLab CDS software.

Dynamic Light Scattering

DLS data was obtained using an ALV DLS/SLS-5022F system (ALV-Laser Vertriebsgesellschaft m.b.H) coupled with a 22mW HeNe Laser (JDS Uniphase Corporation). E-peptide and proIGF2 were diluted to a concentration of 1μM and proIGF2$_{25\text{-}120}$ was diluted to a concentration of 10μM in 25mM Tris pH 7.5, 50mM KCl, 1mM ATP, 0.1mM ADP, 1mM $MgCl_2$, and 1mM DTT. Light scattering signals from the protein samples were monitored at a 90° scattering angle. Each reported value is averaged from 10 rounds of 20 second measurements at 25°C and 630nm. Each individual measurement gave an associated intensity correlation function which was then transferred to a size-distribution function, attaining the R_H[138].

Fluorescence Polarization

50nM FITC-labeled BiP D27C or BiP NBD D27C was incubated in 60mM HEPES pH 7.0, 50mM KCl, 1mM hexokinase-treated ADP, 1mM DTT, 1mg/mL BSA, and 0.556M urea (where applicable) for 30 minutes at 30°C. ADP is hexokinase-treated with 0.005units/μL hexokinase, 1mM glucose, and 5mM $MgCl_2$ at 37°C for 1 hour. Clients, where applicable, were added directly from the purified stock in 8M urea and incubated for an additional 30 minutes at 30°C prior to starting measurements. FP measurements were performed on a Fluoromax-4

spectrofluorometer (Horiba Scientific) with excitation wavelength of 493nm and emission wavelength of 518nm. Both slit widths were set to 6nm with an integration time of 1 second.

For BiP/client and Grp94/client FP assays, BiP or Grp94 was pre-incubated in 60mM HEPES pH 7.0, 50mM KCl, and 1mM DTT for 30 minutes at 30°C, after which 50nM FITC-labeled client was added. FITC-Site 1 was incubated with BiP for an additional hour prior to the start of measurements. For BiP/Grp94/client FP assays, BiP was pre-incubated as in BiP/client assays, then 50nM FITC-labeled client and Grp94 was added. For ATP experiments, 1mM ATP and 1mM $MgCl_2$ was used. For ADP experiments, ADP is hexokinase-treated as described above prior to addition. FP measurements were performed as described above.

For all FP experiments, the 30-minute time point was used in calculating the K_D. K_D values were calculated using the single-site binding equation

$$P = \frac{a[x]}{K_D + [x]} + c \tag{7}$$

Where P is polarization, a is the polarization amplitude, c is the polarization value in the absence of added protein, and x is the concentration of added protein. All titrations to determine K_D values were from multiple separate experiments, each with a different concentration of added protein.

CHAPTER 4: A Unique Rotamer Shift in the BiP-Induced Grp94 C' State Transforms Inhibitor Specificity

AUTHOR CONTRIBUTIONS

Hoxie, R. and Huang, B. designed, conducted and analyzed the smFRET experiments. Gelles, J. and Friedman, L.J. provided assistance and feedback for smFRET experiments. Deans, E. and Hoxie, R. designed and performed the bulk FRET experiments. Azam, T. designed and performed the ATPase experiments. Deans, E. designed and performed all other experiments. Hoxie, R., Deans, E., and Street, T. conceived the idea of the project and Deans, E. and Street, T. wrote this chapter.

4.1 Abstract

Hsp90α and Grp94 are both drug targets due to their involvement in stabilizing oncogenic proteins. Numerous ATP-competitive Hsp90 inhibitors have been developed as potential cancer treatments. However, the structural and mechanistic basis of Hsp90 inhibitor action is difficult to determine due to the conformational and compositional heterogeneity of the cytosolic Hsp70/Hsp90 system. For the BiP/Grp94 system, previous unpublished findings from Reyal Hoxie and Bin Huang of the Street Lab uncovered that BiP radically alters the impact of ATP-competitive inhibitors on the conformation of Grp94. Specifically, some inhibitors are conformationally compatible with the BiP-stabilized Grp94 C' state while others are not. These results will be discussed in the Introduction. Here, I discover the structural basis for this surprising effect. To determine which NTD residues are responsible for the observed conformational specificities of certain inhibitors, I mutated residues in the Grp94 nucleotide pocket based on two candidate structures of the Grp94 C' state: the "coiled-coil" conformation and the "semi-closed" conformation. Mutation of F199 reveals this residue undergoes a rotamer change in the C' state, similar to the equivalent residue in the Hsp90α semi-closed state. Some inhibitors can accommodate this rotamer change while others cannot, explaining the observed conformational specificity of certain Hsp90 inhibitors when bound to Grp94. Conservation of the NTD pocket structure between the Hsp90α semi-closed state and the Grp94 C' state indicates both chaperones bind inhibitors in the same way. This finding provides further evidence that insights from one Hsp70/Hsp90 system can be applicable to other systems, and opens the door for the more tractable BiP/Grp94 system to be utilized for structural and mechanistic analysis of Hsp90 inhibitor action on client proteins.

4.2 Introduction

4.2.1 Hsp90 Inhibitors

Numerous oncogenic proteins rely on Hsp90 for stabilization[2,14,15] and, because of this, Hsp90 inhibitors have been heavily researched as anti-cancer drugs. The major effect of Hsp90 inhibitors *in vivo* is the degradation of client proteins[153]. For example, inhibition of Hsp90 leads to the degradation of client kinases[154] and can induce apoptosis in small-cell lung cancer cell lines[155]. This chapter focuses on ATP-competitive Hsp90 inhibitors which prevent ATP-dependent conformational cycling of Hsp90. ATP-competitive inhibitors have multiple shared traits, including structural compatibility with the Hsp90 open conformation and incompatibility with the closed conformation (Figure 4.1). Currently, there are over a dozen Hsp90 inhibitors in clinical trials; AUY922, Hsp990, and XL888 are specifically highlighted in Figure 4.1 because these inhibitors are discussed in further detail in this chapter. Hsp90 inhibitors share a hot-spot group that hydrogen bonds with a conserved aspartate residue (Hsp90α D93) deep within the Hsp90 nucleotide pocket[156] (shown in dark blue in Figure 4.1.A). Away from this shared hot-spot, ATP-competitive Hsp90 inhibitors are structurally diverse.

As discussed in Chapter 1, Hsp90 inhibitors have been proposed to exert strong anti-cancer effects when Hsp90 is in complex with Hsp70[16], suggesting the combined Hsp70/Hsp90 system is a major biological target of these inhibitors. Understanding how Hsp90 inhibitors structurally and mechanistically influence the Hsp70/Hsp90 system is important, but analysis of the cytosolic Hsp70/Hsp90 pair is difficult due the extensive regulation of this system. If the joint mechanism of Hsp70/Hsp90 pairs is conserved then discoveries from the BiP/Grp94 system can provide insights and predictions for the cytosolic Hsp70/Hsp90 system. Conversely, structural conservation should enable the numerous available structures of cytosolic Hsp90 with and without

inhibitors to provide predictions for how inhibitors influence the BiP/Grp94 pair. Grp94 itself is a potential drug target via its influence on HER2 in certain breast cancers[18], and developing paralog-specific inhibitors is an active area of research. However, Hsp90 inhibitors can generally bind both the cytosolic Hsp90 and Grp94 since the nucleotide binding pocket is largely conserved.

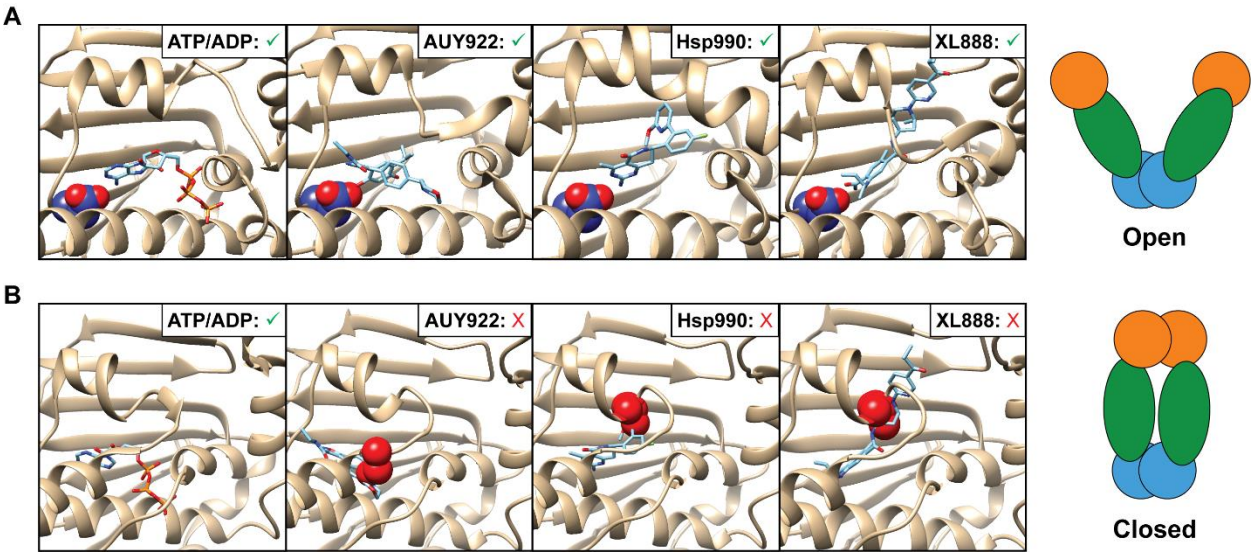

Figure 4.1. A. Structures of ATP (PDB: 3T0Z), AUY922 (PDB: 6LTI), Hsp990 (PDB: 4U93), and XL888 (PDB: 4AWO) bound to the Hsp90α NTD. Binding of inhibitors to the NTD is likely a reliable indication of how the inhibitors bind to the NTD in the context of full-length Hsp90 in the open state. Asp93 shown in dark blue. **B.** Superposition of structures containing AUY922, Hsp990, and XL888 onto the Hsp90α closed structure (PDB: 5FWK). Hsp90 structures are shown in tan, nucleotides/inhibitors shown in light blue, and residues which clash with inhibitors are shown in red.

4.2.2 BiP Radically Alters the Impact of Hsp90 Inhibitors on the Conformation of Grp94

Recall from Chapter 1 that BiP accelerates ATP-dependent closure of the Grp94 dimer, and, in the absence of ATP, BiP stabilizes the Grp94 C' state which has a FRET efficiency higher than that of the closed state[80]. During the normal ATPase cycle of Grp94 in the absence of BiP, Grp94 can also adopt a state with FRET efficiency similar to the BiP-induced C' state[85]. In this case the C' state is populated in opening events, via a C→C'→O transition. The BiP-induced C' state and the BiP-independent C' state have the same name because of their comparable FRET efficiency, but it is unclear if these states are identical. This chapter focuses only on the BiP-

induced C' state. However, in the Discussion I will propose that a peculiar feature of the BiP-induced C' state may explain a peculiar feature of the Grp94 ATPase cycle in the absence of BiP.

A structure of the C' state has not been determined, meaning that the detailed configuration of the nucleotide binding pocket is not known. Nevertheless, FRET measurements have indirectly suggested that BiP modifies the structure of the Grp94 nucleotide binding pocket in the C' state. Specifically, Reyal Hoxie and Bin Huang discovered that some Hsp90 inhibitors allow BiP to push Grp94 into the C' state, while others do not.

The initial evidence that BiP alters the impact of ATP-competitive inhibitors on the conformation of Grp94 came from a previously described bulk-FRET assay in which increasing the BiP NBD concentration increases Grp94 FRET efficiency due to BiP driving Grp94 into the high-FRET C' state[87]. Given that all commercially available Hsp90 inhibitors are sterically incompatible with the well-established ATP-bound closed conformation, and that the C' conformation of Grp94 involves closure of the dimer arms, one might expect that all Hsp90 inhibitors would prevent BiP-induced conformational changes to Grp94. However, the FRET assay shows something different – when Grp94 is bound to BiP, Hsp90 inhibitors have variable effects on Grp94 conformation (Figure 4.2.A). Figure 4.2.B ranks these inhibitors by the degree to which they change the Grp94 conformation. Hsp990 and XL888 show maximal suppression of BiP-induced conformal changes to Grp94 while AUY922 has the least suppression, and ADP sits between these two extremes. The surprising conclusion is that Hsp90 inhibitors can unmask different structural consequences on Grp94, but this is only evident when Grp94 is in complex with BiP. However, these findings give no indication of an underlying structural explanation.

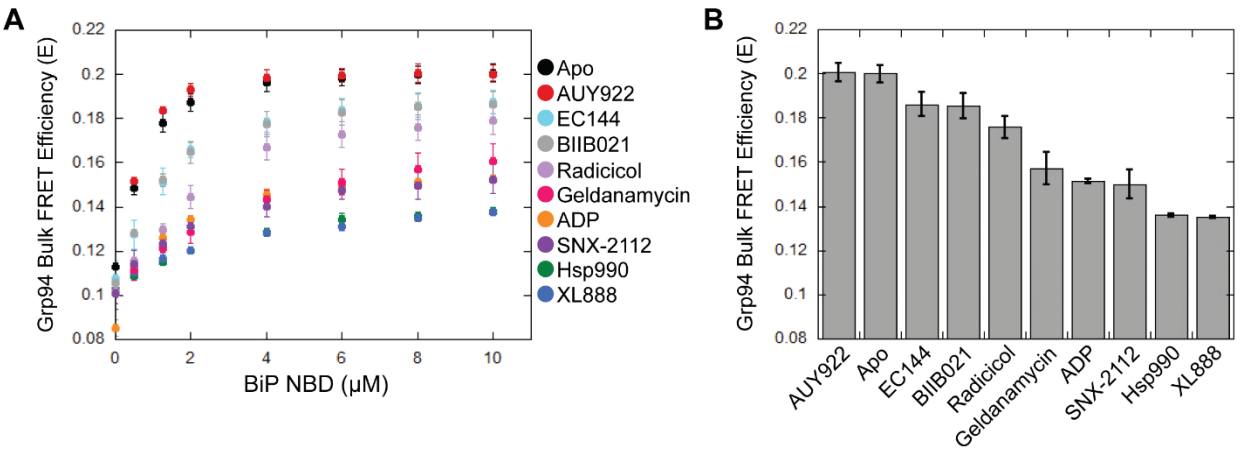

Figure 4.2. A. Grp94 bulk FRET efficiency at varying concentrations of BiP NBD with no inhibitor (black), 1mM ADP (orange), or 50μM inhibitor. **B.** Grp94 bulk FRET efficiency at 8μM BiP NBD. Error bars are the SEM from at least two measurements.

AUY922, Hsp990, XL888, and ADP were selected for a more detailed smFRET analysis. These three inhibitors bind tightly to Grp94 according to a thermal shift assay (TSA, at an inhibitor concentration of 50μM): Hsp990 (ΔT_m=10.1°C), AUY922 (ΔT_m=15.4°C), and XL888 (ΔT_m=8.6°C). In the absence of BiP, none of these ligands influence the Grp94 conformation, which is maintained in the open state (ε~0.15, Figure 4.3). In the presence of BiP, different outcomes are observed for each ligand. For AUY922 the Grp94 C' state (ε~0.9, Figure 4.3.B) remains highly populated, whereas for XL888 and Hsp990 the C' state is minimally populated and Grp94 instead adopts a heterogeneous mixture of the open state and configurations with intermediate FRET (ε ~ 0.3-0.5) that have not been observed previously (Figure 4.3.C-D). Under ADP conditions the C' configuration may be transiently populated, but a broad distribution of FRET values is observed with a peak efficiency at ε ~ 0.8 (Figure 4.3.E). The broad distribution of efficiency values observed with ADP arises in part from signal averaging in which Grp94 conformational changes occur on a similar timescale as the integration time. Analysis of signal averaging on Grp94 smFRET measurements has been discussed in a previous publication[80]. Additionally, commercial stocks of ADP contain ~2% ATP[119]. Contaminating ATP, which was

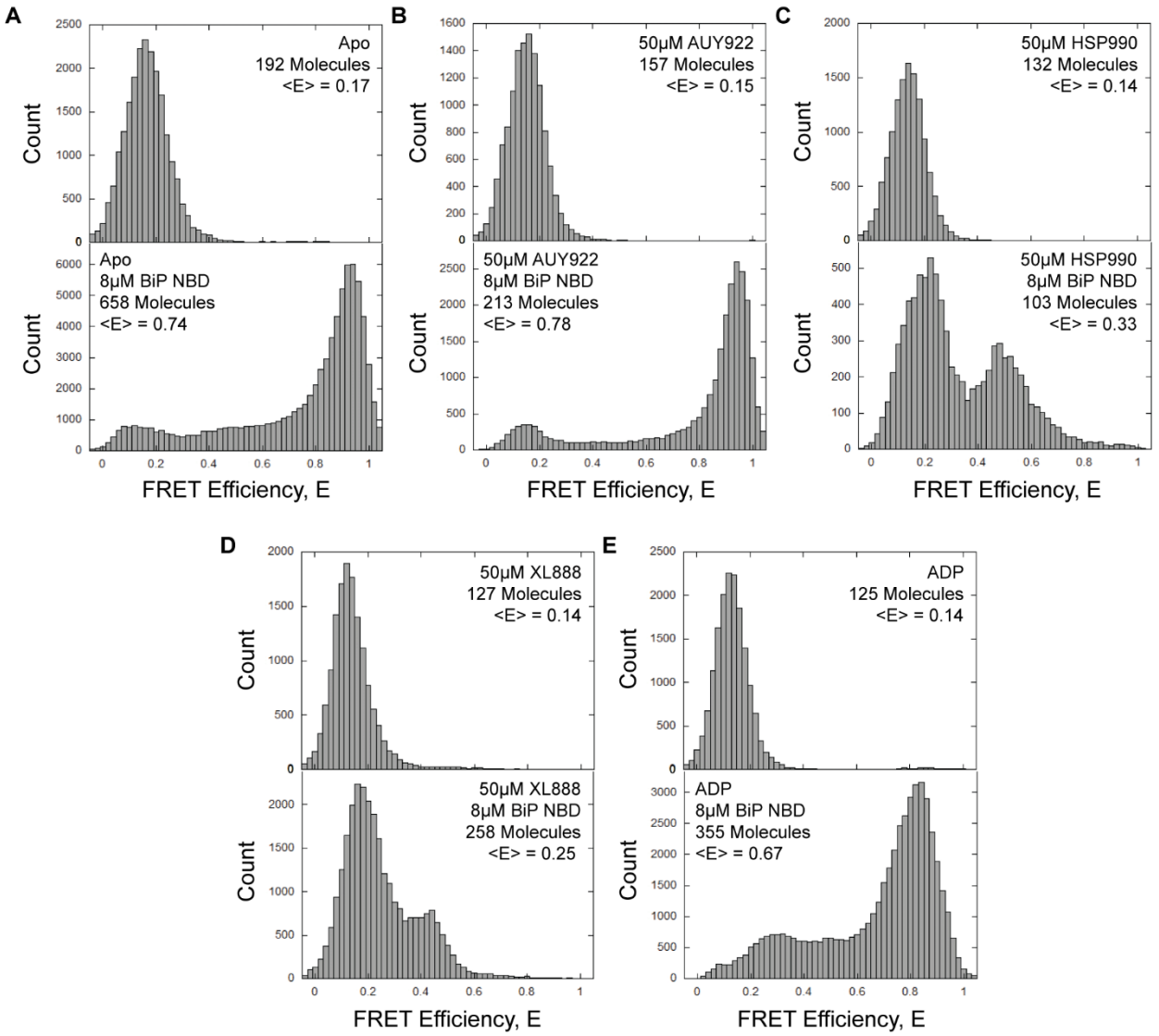

Figure 4.3. smFRET efficiency histograms for Grp94 with and without 8μM BiP NBD. Results shown for measurements in the absence of any ligand (Apo, **A**), and in the presence of 50μM AUY922 (**B**), 50μM Hsp990 (**C**), 50μM XL888 (**D**), and 1mM ADP (**E**). Data collected at integration time of 1s (650μW at 532nm, 150μW at 633nm). <E> is the average FRET efficiency for the entire histogram.

not removed from ADP stocks in Figure 4.3.E, may also contribute to the FRET efficiency distribution.

The smFRET results are more definitive than the bulk FRET since individual populations can be measured by smFRET. Bulk FRET measures the average FRET efficiency of all Grp94 conformations present. Figure 4.4.B shows that the bulk FRET measurements follow the same trend as the average FRET efficiency (<E>) in smFRET, in which a greater change in bulk FRET

efficiency correlates to greater C' accumulation in smFRET. Therefore, bulk FRET measurements can be used as a tool to assess the C' compatibility of different Hsp90 inhibitors.

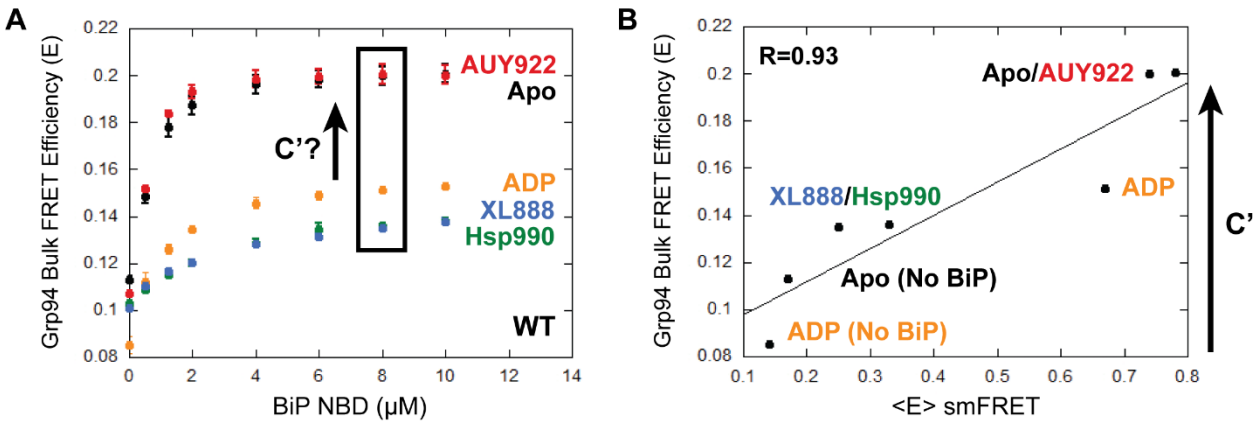

Figure 4.4. A. Grp94 bulk FRET efficiency at varying concentrations of BiP NBD with no inhibitor (black), 1mM ADP (orange), or 50μM inhibitor. Data is the same as in Figure 4.2.A. **B.** Relationship between Grp94 smFRET and bulk FRET with 8μM BiP NBD. Bulk FRET data is boxed out in panel A. Solid line is a linear fit with correlation coefficient (R) shown in figure. Arrow indicates increasing C' population.

4.3 Results

The above FRET results are complex and intriguing. The main conclusion is that BiP unmasks inhibitor-specific changes to the structure of Grp94, but the cause is unclear. Rather than focus on the new Grp94 conformations with intermediate FRET efficiency values that are populated from Hsp990 and XL888, we first want to understand why AUY922 allows BiP to push Grp94 into the C' conformation but Hsp990 and XL888 do not. A plausible explanation is that BiP induces a change to the structure of the Grp94 nucleotide binding pocket in the C' state, and this change is sterically compatible with the structure of AUY922 but incompatible with Hsp990 or XL888. Recall from Chapter 1 that the Trap1 "coiled-coil" structure and the Hsp90 "semi-closed" structure are candidate models for the BiP-stabilized C' state of Grp94. Both structures have no ligand bound to the NTD and show notable changes to the configuration of the nucleotide binding

pocket, suggesting that these structures could have different steric compatibility with AUY922, Hsp990, and XL888.

In the comparison of the coiled-coil and semi-closed structures, a conserved Phe residue stands out (Hsp90α_{F138}, Trap1$_{F205}$, and Grp94$_{F199}$). In the semi-closed structure, the Phe sidechain position is flipped out due to a rotamer change around the C_α-C_β bond, creating a hydrophobic cluster with multiple lid residues, including a conserved Leu (Hsp90α_{L107}, Trap1$_{L172}$, and Grp94$_{L163}$, Figure 4.5). The flipped F138 sidechain position in the Hsp90α semi-closed structure is unusual, and in the PBD we found no other instances of an Hsp90 family-member structure that has a similar Phe sidechain orientation at this position. For the coiled-coil structure the corresponding Phe sidechain is not flipped out and the Leu sidechain occupies a different location in the nucleotide binding pocket.

Figure 4.6 shows a docking analysis of AUY922, Hsp990, XL888, and ADP onto the nucleotide binding pocket of the coiled-coil and semi-closed structures. Both structures are sterically compatible with AUY922 but clash with Hsp990 and XL888, which is consistent with the experimental observation that Grp94 can populate the C' conformation when bound to AUY922 but not when bound to Hsp990 and XL888 (Figure 4.3). Interestingly, the residues which clash with Hsp990 are different for the coiled-coil and semi-closed structures. In the coiled-coil structure Hsp990 clashes with the Leu sidechain, while in the semi-closed structure Hsp990 primarily clashes with the Phe sidechain. For XL888, both the coiled-coil and semi-closed structures predict extensive clashes with the peptide backbone of the lid. ADP shows a clash with the semi-closed structure, which is consistent with the decreased C' population observed experimentally (Figure 4.3), whereas no clash is predicted for the coiled-coil structure. The

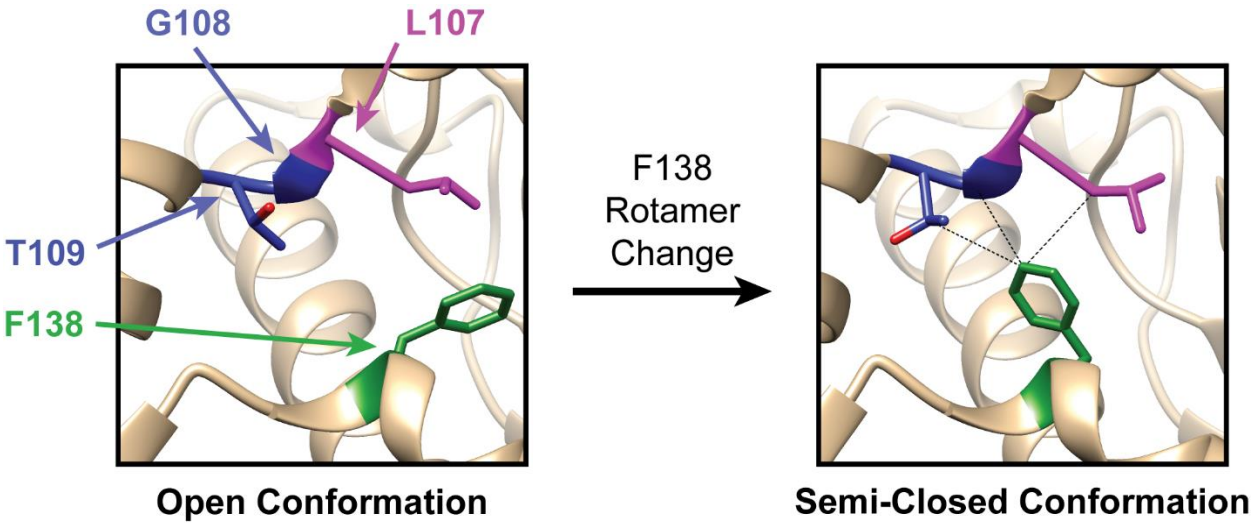

Figure 4.5. F138 (green) rotamer change between the Hsp90α open (left, PDB: 5J2V) and semi-closed (right, PDB: 7KW7) conformations. The residues involved in the hydrophobic cluster are labeled. L107 is shown in magenta and G108 and T109 are shown in blue on the structures. (*Right*) The hydrophobic cluster is indicated by black dashed lines between the residues.

predicted compatibilities of nucleotides and inhibitors for the semi-closed and coiled-coil structures are summarized in Table 4.1.

Docking shows that a BiP-induced change to the Grp94 nucleotide binding pocket could explain why AUY922 is C'-compatible but Hsp990 and XL888 are not (Figure 4.6). However, docking does not differentiate whether the pocket changes are more like the coiled-coil structure or the semi-closed structure. The Grp94 mutations F199A and L163A can differentiate between these possibilities. In this comparison, AUY922 is a control because it should continue to be C'-compatible for both mutations. XL888 is also a control because it should continue to be C'-incompatible for both mutations due to the extensive clashes with the peptide backbone of the lid. Hsp990 provides the main test, in which the semi-closed structure predicts that the F199A mutation will make Hsp990 more C'-compatible, whereas the coiled-coil structure predicts no change from F199A. In contrast, the coiled-coil structure predicts that L163A will make Hsp990 more C'-compatible, whereas the semi-closed structure predicts no change from L163A. Table 4.1 shows how these predictions would be manifested in Grp94 FRET measurements with BiP, analogous to

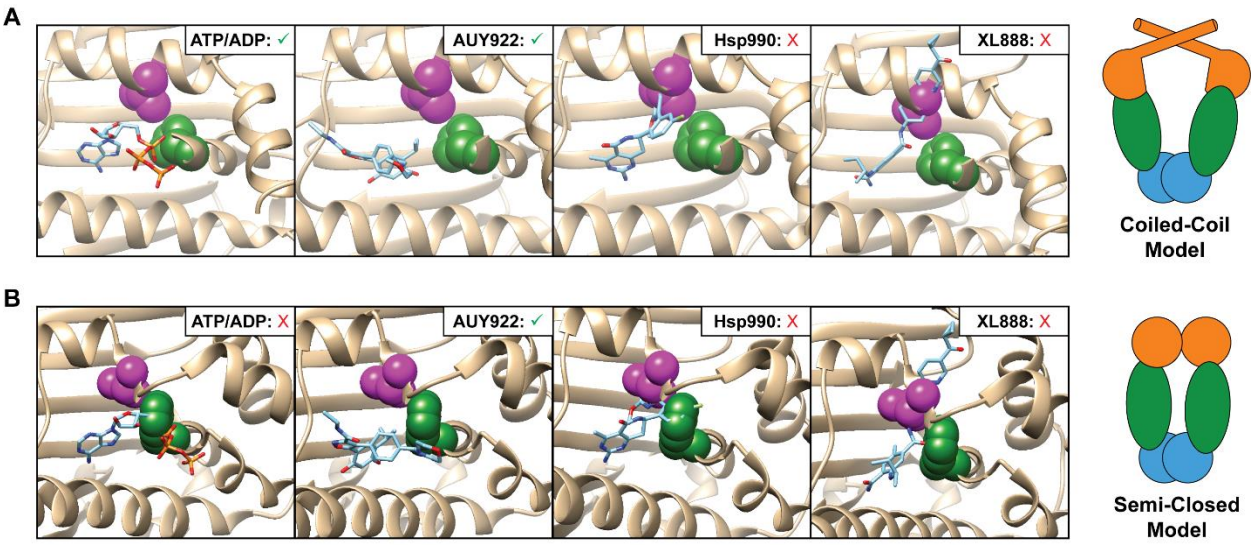

Figure 4.6. A. Superposition of structures containing ATP (PDB: 3T0Z), AUY922 (PDB: 6LTI), Hsp990 (PDB: 4U93), and XL888 (PDB: 4AWO) onto the coiled-coil Trap1 NTD structure (PDB: 5F3K). **B.** Superposition of structures containing ATP, AUY922, Hsp990, and XL888 onto the semi-closed Hsp90α NTD structure (PDB: 7KW7). Hsp90 structures shown in tan, nucleotide/inhibitors shown in light blue. The residues corresponding to L107 and F138 are shown in magenta and green respectively.

those shown in Figure 4.4.A. The coiled-coil model predicts a FRET increase from the Grp94 L163A mutation whereas the semi-closed model predicts a FRET increase from the Grp94 F199A mutation (indicated by arrows in Table 4.1).

With the above predictions in mind, we constructed the L163A and F199A Grp94 variants. Because L163 and F199 are in the nucleotide binding pocket, we anticipated that the mutations could destabilize Grp94. Indeed, the melting temperatures (T_m) of L163A (41.8±0.1°C) and F199A (36.7±0.1°C) are both decreased compared to wild type (44.3±0.1°C). Despite this destabilization, ATPase measurements show F199A maintains a similar activity to wild-type Grp94 (Figure 4.7), indicating this mutation does not disrupt nucleotide binding. In contrast, L163A shows a complete loss of activity in the absence of BiP NBD. This loss of activity is due to impaired ATP binding rather than a loss of ATPase function, which will be discussed further in the Discussion. Both L163A and F199A exhibit an enhancement of activity in the presence of BiP NBD and this activity

	Coiled-Coil	Semi-Closed	
WT	✓	✓	**AUY922**
	X	X	**Hsp990**
	X	X	**XL888**
Hsp90α L107A (Grp94 L163A)	✓	✓	**AUY922**
	✓ (↑)	X	**Hsp990**
	X	X	**XL888**
Hsp90α F138A (Grp94 F199A)	✓	✓	**AUY922**
	X	✓ (↑)	**Hsp990**
	X	X	**XL888**

Table 4.1. Predicted compatibility of Hsp90 inhibitors to various Grp94 constructs based on structural models of the coiled-coil and semi-closed structures. Grp94 numbering is in parentheses. Green check marks indicate C' compatibility, red X marks indicate C' incompatibility, and up arrows indicate a predicted increase in bulk FRET efficiency compared to WT in experiments analogous to Figure 4.4.A.

is abolished by AUY922, Hsp990, and XL888 (Figure 4.7), indicating the mutants maintain the ability to bind inhibitors.

FP measurements show that Grp94 L163A and F199A bind the BiP NBD with similar affinity to WT Grp94 under apo conditions (WT K_D: 0.23±0.01μM; L163A K_D: 0.28±0.01μM; F199A K_D: 0.18±0.02μM). Of note, BiP/Grp94 affinity is nucleotide, pH, and temperature sensitive. The K_D values reported here differ from the affinities reported in Chapter 3 due to differences in experimental conditions.

As discussed previously, bulk FRET measurements can report on the extent of C' compatibility for Hsp90 inhibitors (Figure 4.4.A), so we constructed the FRET-labeled Grp94 L163A and F199A variants. According to Table 4.1, AUY922 and XL888 act as controls because AUY922 should remain C' compatible and XL888 should remain C' incompatible for both the L163A and F199A variants. This is indeed what is observed experimentally, where the L163A and F199A FRET levels remain high with AUY922 and low with XL888 (Figure 4.8). For Hsp990,

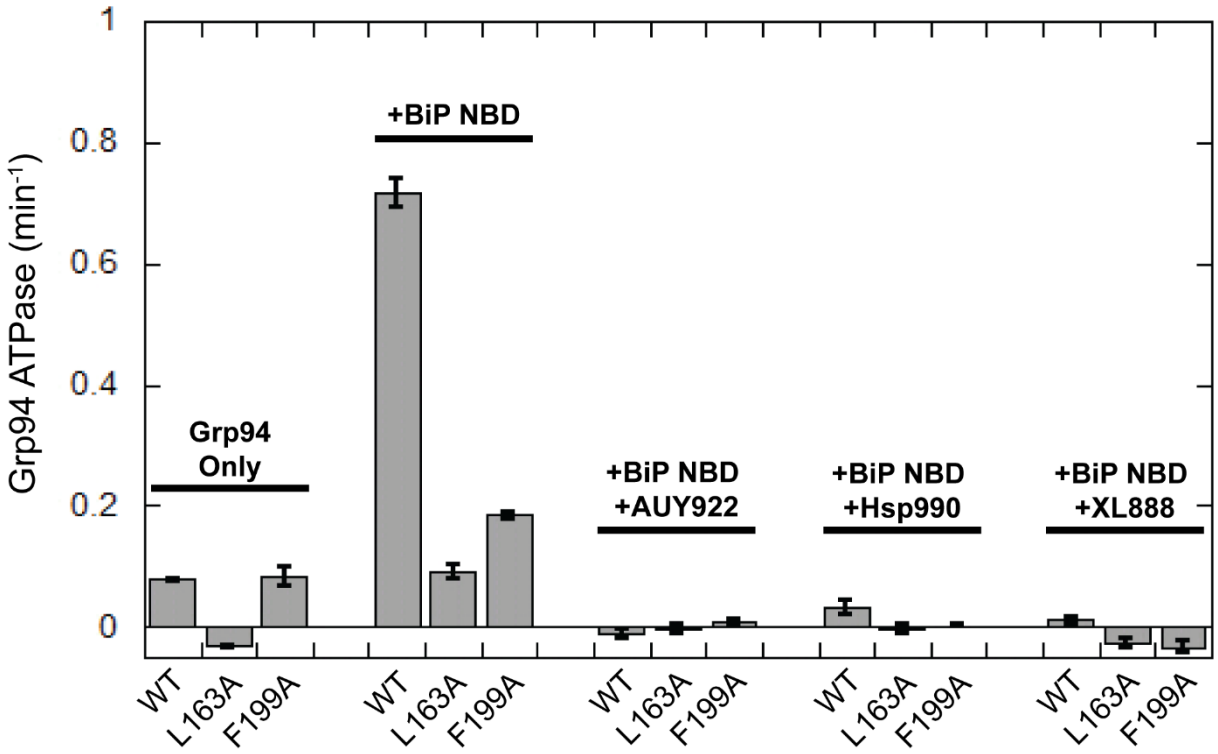

Figure 4.7. ATPase activity for WT Grp94, Grp94 L163A, and Grp94 F199A with and without 8μM of a hydrolytically inactive BiP NBD variant, and in the absence or presence of 50μM AUY922, Hsp990, or XL888.

the F199A mutation increases Grp94 FRET efficiency whereas the L163A results in a modest decrease (Figure 4.8). These results are consistent with the predictions for the semi-closed structure and inconsistent with the predictions from the coiled-coil model.

Overall, we conclude that the pattern of C' compatibility observed experimentally (Figure 4.3) can be explained by BiP-induced changes to the Grp94 pocket, which would cause steric clashes with XL888 and Hsp990, but not AUY922 (Figure 4.9). Our results indicate that the Grp94 F199 pocket residue plays a unique role for inhibitor binding in the context of the BiP-stabilized C' conformation. Finally, the semi-closed structure of cytosol-specific Hsp90 bound to Hsp70 can explain the experimentally observed pattern of inhibitor compatibility to the C' conformation of the ER-specific Grp94 bound to BiP. This last point shows that a deep mechanistic and structural

conservation between these long-diverged Hsp70/Hsp90 systems is relevant to their mode of action with commercially-developed inhibitors.

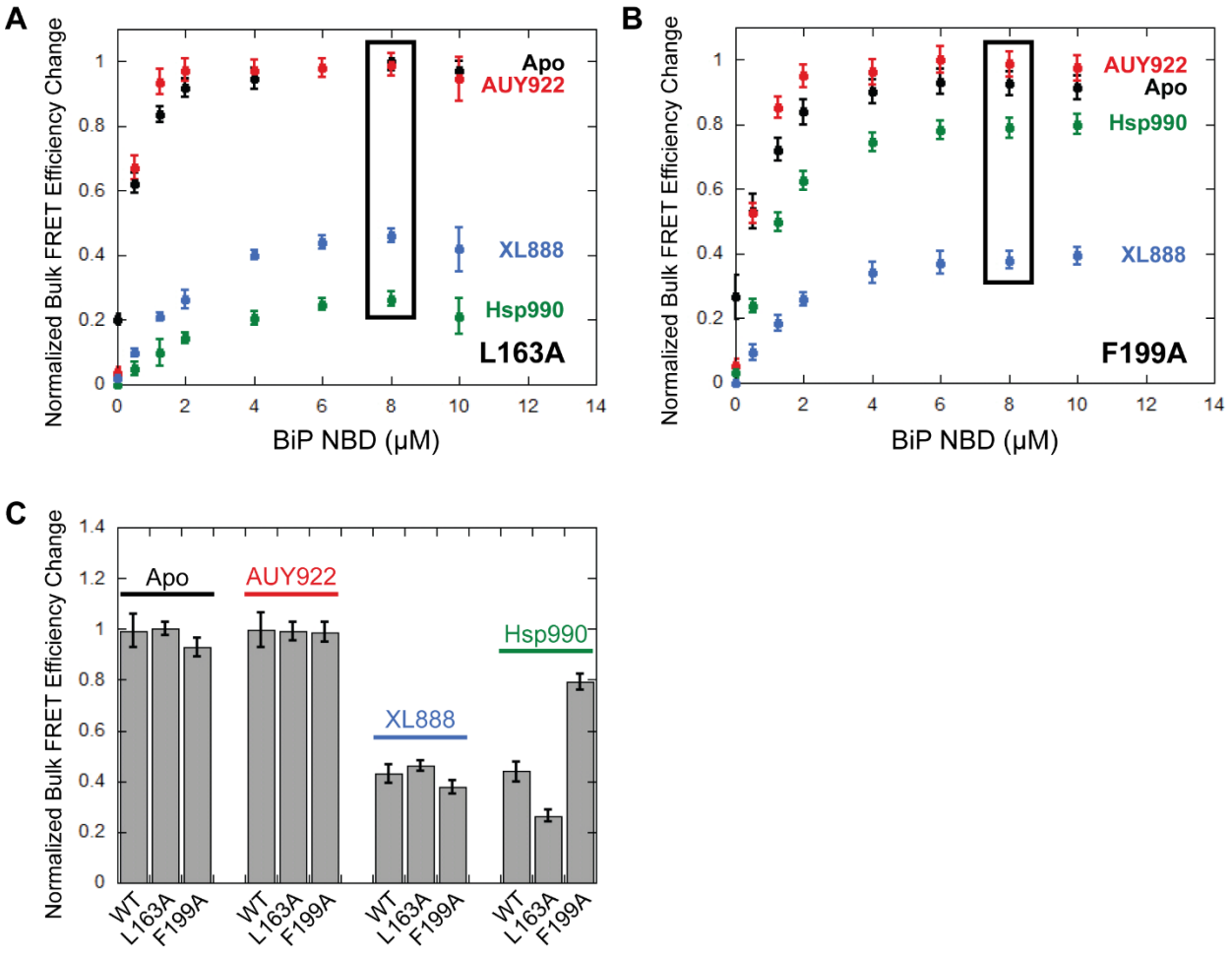

Figure 4.8. A-B. Grp94 L163A (**A**) and F199A (**B**) normalized bulk FRET efficiency change at varying concentrations of BiP NBD with no inhibitor (black) or 50μM AUY922 (red), XL888 (blue), or Hsp990 (green). **C.** Normalized Grp94 bulk FRET efficiency change at 8μM BiP NBD for wild-type, L163A, and F199A with no inhibitor or 50μM inhibitor. Bulk FRET data is boxed out in panels A and B, wild-type data is same as in Figure 4.4.A. Error bars are the propagated uncertainty from at least two measurements.

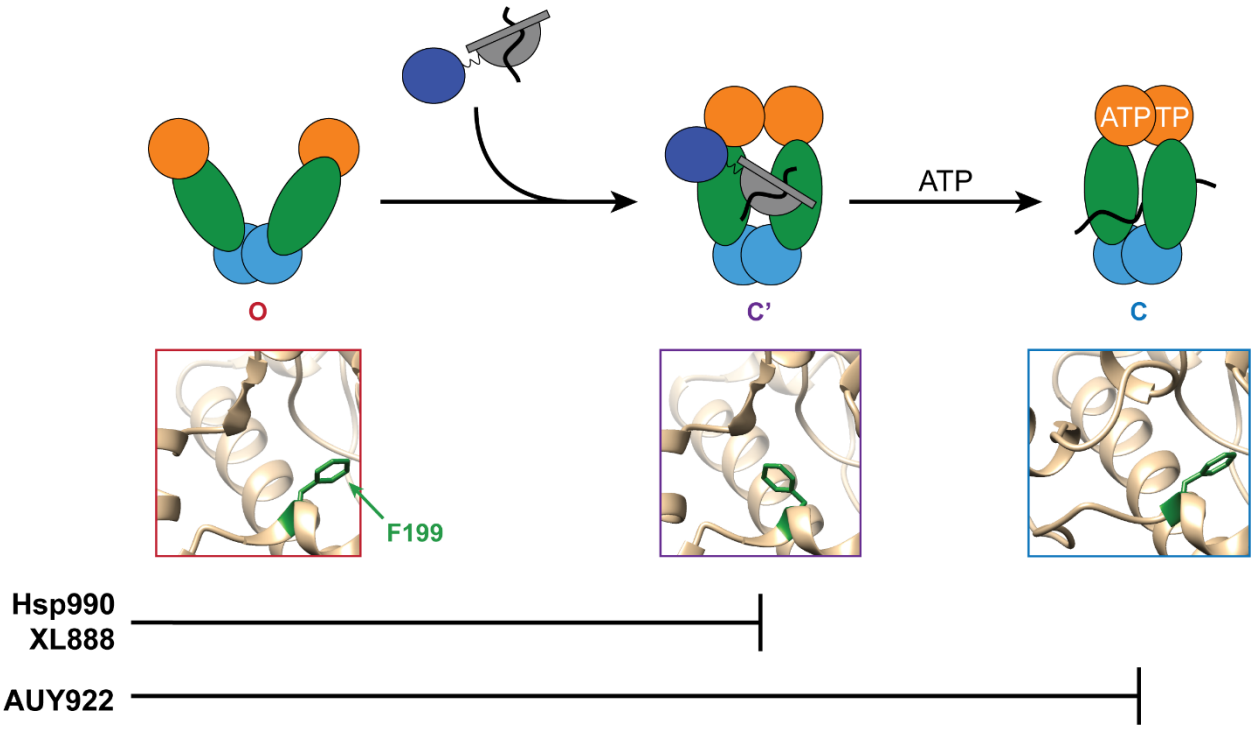

Figure 4.9. Schematic of BiP-induced Grp94 conformational changes, and the corresponding conformational specificity of Hsp90 inhibitors Hsp990, XL888, and AUY922. Labels for the open (O), C', and closed (C) Grp94 conformational states and the F199 rotamer position of each conformational state (open state PDB: 5J2V; C' state PDB: 7KW7; closed state PDB: 7KRJ) are under the corresponding cartoon.

4.4 Discussion

Coordinated Hsp70/Hsp90 chaperoning has features that are conserved in prokaryotes, eukaryotes, and within organelles, but the structural and mechanistic details of this joint function remain an active area of research. The discovery that BiP both brings clients to Grp94 and also accelerates Grp94 arm closure for client trapping provided new insights into Hsp70/Hsp90 function[80]. BiP accelerates Grp94 arm closure by stabilizing the C' state, a high-energy closure intermediate. Beyond this, however, our knowledge of the C' state is limited since a structure of this state has not been determined. Here, by designing point mutations based on candidate homolog structures, we discover the Grp94 C' state nucleotide pocket shares a unique characteristic of the Hsp90α semi-closed state. Specifically, a Phe199 rotamer change is energetically favorable in the

C’ state and some ligands can accommodate this change and others cannot. This rotamer change creates a hydrophobic cluster with residues from the lid which cuts off a section of the nucleotide pocket, explaining the decreased accumulation of C’ state with ADP versus apo conditions (Figure 4.3.E).

The ATPase of the Grp94 L163A variant shows this mutant is nearly inactive when not bound to BiP (Figure 4.7). This result suggests the L163A variant either has impaired nucleotide binding or impaired ATPase function. L163 (L107 in Hsp90α) was previously shown to play a major role in determining the flexibility of α-helix3, and replacement of the sidechain with alanine stabilizes a single conformation of this helix[157]. Comparing the NTD structures of wild-type and the L163A variant, both sidechains occupy the same hydrophobic pocket (Figure 4.10.A and C). However, since the alanine sidechain is shorter than that of leucine, it forces α-helix3 to adopt a “loop in” conformation in order for alanine to occupy the pocket. This “loop in” conformation clashes with ATP (Figure 4.10.A-B), indicating the L163A mutation impairs Grp94 nucleotide binding, resulting in the observed decrease in ATPase activity.

The stabilization of α-helix3 may also explain the observed decrease in L163A bulk FRET efficiency with Hsp990 (Figure 4.8.A and C). The change in Grp94 bulk FRET efficiency with Hsp990 (Figure 4.4.A) is likely due to the accumulation of intermediate configurations, as observed in smFRET (Figure 4.3.C). Decreased flexibility of α-helix3 with the L163A mutation may prevent Grp94 from reaching these intermediate configurations, ultimately decreasing the observed FRET efficiency change. However, further studies are needed to test this idea.

The pocket structure of the Hsp90α semi-closed state explains the pattern of C’ compatibility for Grp94 (Figure 4.8). This indicates that both chaperones bind inhibitors in a similar way and provides further evidence that findings from one Hsp70/Hsp90 system can be

applicable to others. Because of this, the more tractable BiP/Grp94 system can be used for future structural and mechanistic analysis of Hsp90 inhibitor action. Competitive inhibitors prevent ATP-dependent conformational changes of Hsp90, but it is not clear how this causes a change to client protein folding and degradation, and ultimately cell death. The coordinated function of Hsp70/Hsp90 also appears to be important for the efficacy of Hsp90 inhibitors[16], but again it is not clear why. One possibility is that Hsp90 inhibitors only need to prevent arm closure, and in this case AUY922 would be less effective compared to Hsp990 and XL888 since AUY922 allows BiP to lock Grp94 into a closed state. The semi-closed state does differ from the closed state, but both states can trap client proteins between the dimer arms. Hsp990 and XL888 are not compatible with the C' or closed state, suggesting no client trapping could occur. Future studies can utilize the different C' compatibilities of AUY922, Hsp990, and XL888 to evaluate outcomes of various client proteins.

While our results are consistent with the Grp94 C' nucleotide pocket resembling that of the semi-closed conformation, the C' NTD structure likely does not fully resemble the semi-closed conformation. A previous study utilized a Grp94 crosslinking mutant derived from the coiled-coil structure which showed robust disulfide formation in the presence of BiP and a ~50-fold increase in affinity between crosslinked Grp94 and BiP versus wild type[80]. The semi-closed conformation would be unable to support crosslinking at this site due to the C_α-C_α distance being more than double that of the coiled-coil conformation, and the R-groups face in opposite directions. Because of this, there are two main possibilities for the C' NTD structure. The first is the C' NTD structure is comprised of elements of both the semi-closed and coiled-coil structures. The second is that the C' state is not a singular state but an ensemble of high FRET intermediate conformations which

could include the semi-closed and coiled-coil states. Future structural studies are needed to address these questions about the Grp94 C' state.

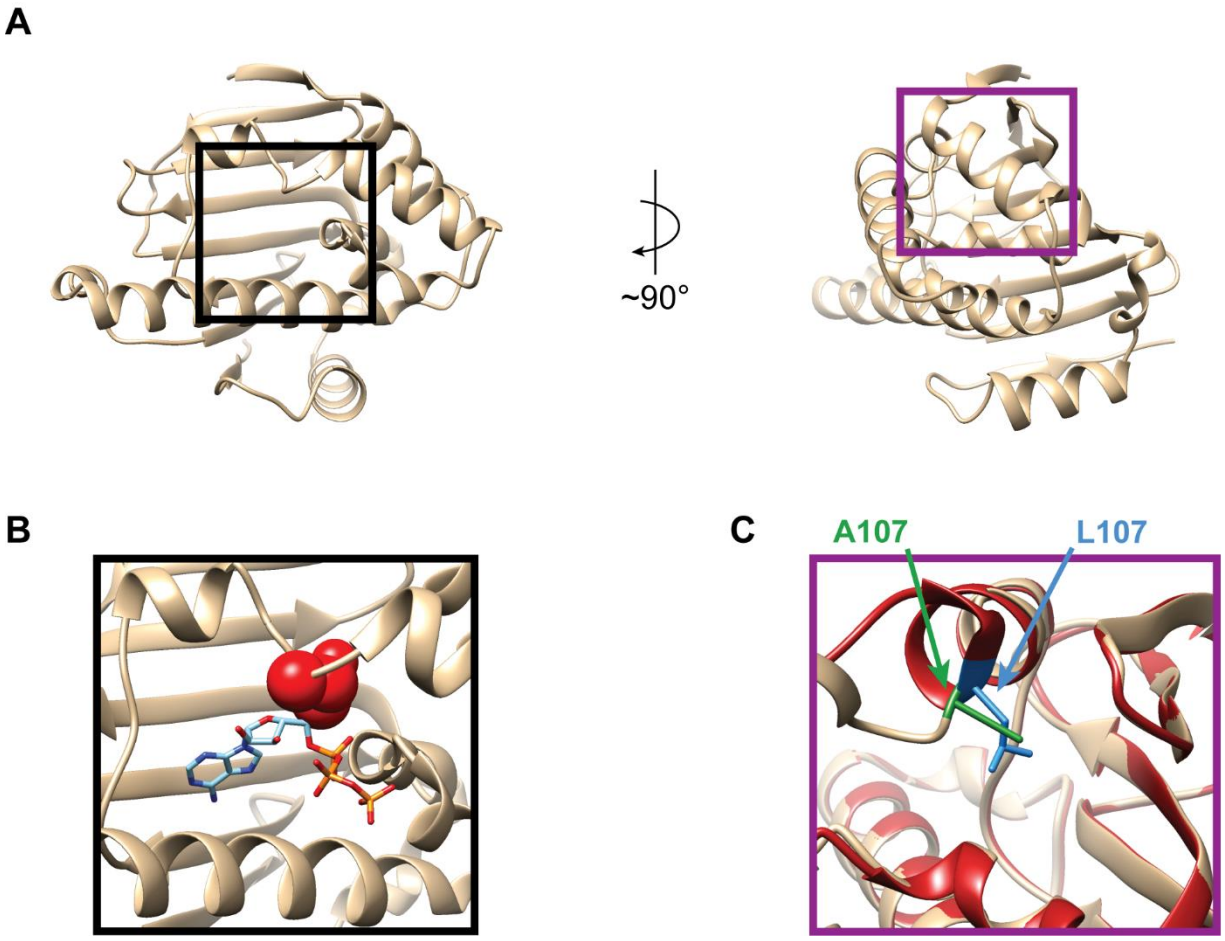

Figure 4.10. A. Front (left) and side (right) view of the Hsp90α A107 NTD (PDB: 5J80). **B.** Superposition of an ATP-bound Hsp90α NTD structure (PDB: 3T0Z) onto the Hsp90α A107 NTD structure. ATP shown in light blue and residues which clash with ATP are shown in red. **C.** Overlay of A107 (tan) and L107 (red, PDB: 3T0Z) Hsp90α NTD structures. A107 shown in green, L107 shown in blue.

4.4.1 Relevance of F199 to the Grp94 ATP-Driven Conformational Cycle

An observation from Salvatore LaRussa of the Street Lab indicates Grp94 undergoes substrate inhibition at high concentrations of ATP[158]. ATPase measurements at variable ATP concentrations exhibit a "bump" in Grp94 activity at low concentrations of ATP and a slow decrease of activity at higher concentrations (Figure 4.11.A). The "bump" in Grp94 activity

roughly corresponds to the ATP concentration with the highest predicted fraction of Grp94 mixed-nucleotide state (ATP:Apo), and this population decays as Grp94 binds a second ATP molecule at higher concentrations of ATP (ATP:ATP, Figure 4.11.B). Because of this, the ATPase measurements in Figure 4.11.A are fit with a model in which ATP hydrolysis occurs at different rates whether one (v_1) or two (v_2) ATP molecules are bound to a Grp94 dimer and assumes the ATP affinity (K_D) of one Grp94 arm is independent of the nucleotide state of the opposing arm (see Methods). Grp94 exhibits a ~2.5-fold decrease in ATPase rate when two versus one molecule of ATP is bound. Since arm closure is the rate-limiting step of the Grp94 ATPase cycle, the enhanced activity under non-saturating ATP conditions likely corresponds to faster closure.

A Phe199 rotamer shift in the Grp94 C' state could provide an explanation for faster arm closure of Grp94 when the dimer is bound to only one ATP molecule. I hypothesize the Phe199 rotamer shift stabilizes the Grp94 lid configuration during ATP-dependent closure. This hypothesis predicts that bound nucleotide would prevent the Phe199 rotamer change, which would prevent formation of the hydrophobic cluster with the lid. If a Grp94 dimer has ATP on both arms, neither arm would have the stabilizing Phe199/lid hydrophobic cluster. Conversely, a Grp94 dimer with only one ATP bound would have one NTD stabilized by the Phe199/lid hydrophobic cluster. This additional stabilization of the C' state would lower the energetic barrier to closure (Figure 4.11.C), explaining the enhanced Grp94 activity under non-saturating ATP conditions. Since the rotamer change cannot occur with the F199A mutant, regardless of the nucleotide state of Grp94, this mutant should not exhibit a "bump" in activity at low ATP concentrations. Additionally, the C' state should be more highly populated in Grp94 smFRET measurements with decreasing ATP concentrations, whereas the F199A mutant would exhibit no change.

This idea could be further tested by performing the same ATPase measurements as in Figure 4.11.A but with a Grp94 heterodimer, in which one arm is wild-type and the other containing a nucleotide pocket mutation which prevents or diminishes ATP binding, such as L163A. The heterodimer should not exhibit a decay in activity with increasing concentrations of ATP. A similar experiment was previously done with yeast Hsp90 heterodimers, in which one arm was wild-type and the other contained an ATP-binding defective mutation (WT/D79N)[159]. These

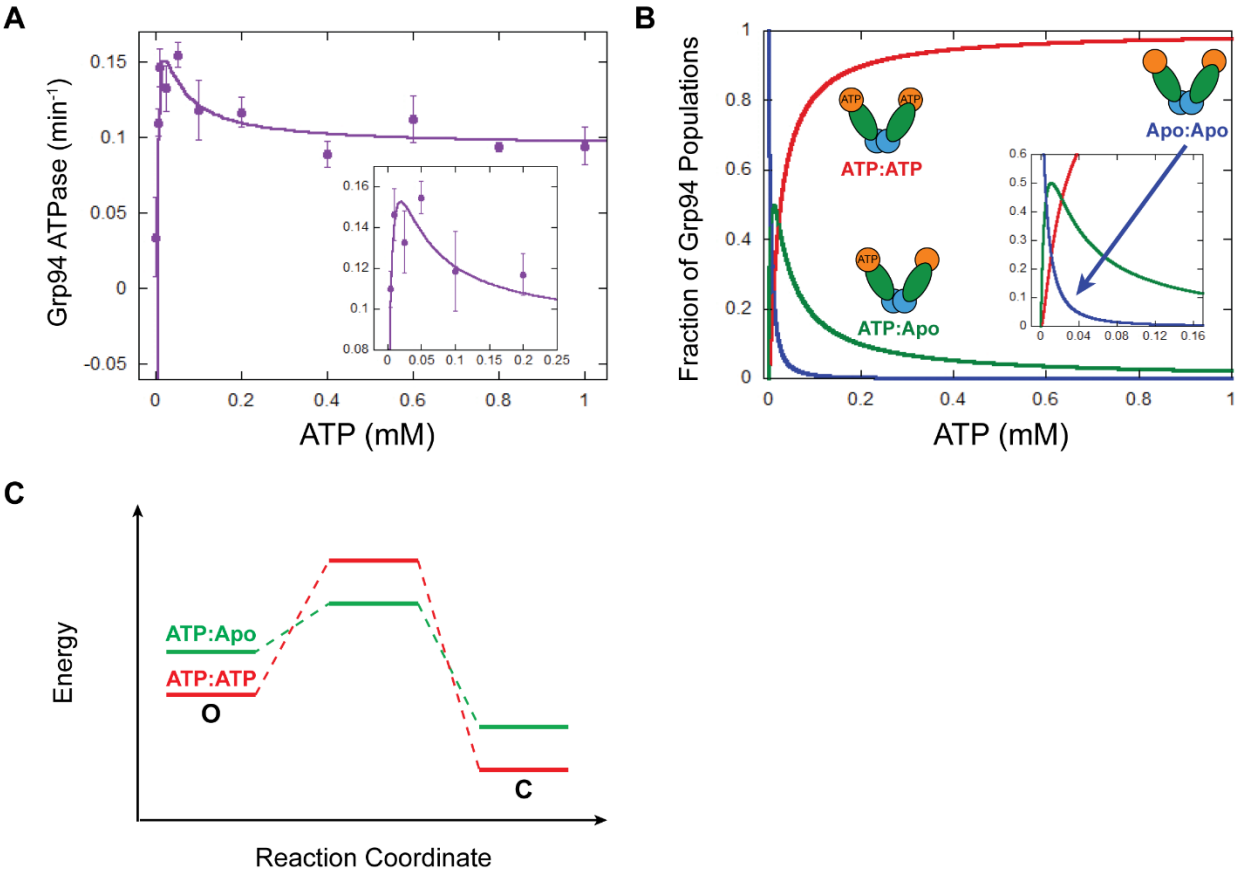

Figure 4.11. A. Wild-type Grp94 ATPase measurements at varying concentrations of ATP. Solid line is a fit to Equation 3 (v_1=0.24±0.02min^{-1}; v_2=0.10±0.03min^{-1}; K_D=11±3.4μM). (*Inset*) Grp94 ATPase measurements at low ATP concentrations. Error bars are the SEM of three measurements, reported errors for hydrolysis rates and ATP affinity are the fitting error. Figure adapted from LaRussa, SA (2023)[158]. **B.** Predicted populations of Grp94 nucleotide states (ATP:ATP (red), ATP:Apo (green), and Apo:Apo (blue)) at varying concentrations of ATP. (*Inset*) Zoom in of Grp94 populations at low ATP concentrations. **C.** Proposed Grp94 closure reaction scheme. Open (O) and closed (C) Grp94 states are labeled beneath the corresponding energy state.

heterodimers exhibited only a modest difference in activity compared to wild-type homodimers. However, a similar experiment has not been done with Grp94.

Additionally, wild-type yeast Hsp90 does not exhibit substrate inhibition such as Grp94[159,160]. Other Hsp90s exhibit differences in ATPase activity, such as Trap1 which exhibits substrate inhibition similar to Grp94[161] or HtpG which does not[48]. The difference in activity between Hsp90s is likely due to the variation of ATP affinities among these chaperones. Grp94 and Trap1 exhibit low micromolar affinity for ATP (K_D ~ 10-100μM)[152,158], whereas cytosolic Hsp90s and HtpG exhibit low millimolar affinity for ATP (K_D ~ 0.13-1mM)[162,163]. For cytosolic Hsp90s and HtpG, the mixed nucleotide state (ATP:Apo) will remain a prevalent fraction of the population even at high concentrations of ATP, resulting in no observable substrate inhibition.

4.5 Methods

Inhibitor Docking Analysis

Docking analyses were performed with MatchMaker on UCSF Chimera[164]. For the Trap1 coiled-coil structure (PDB: 5F3K), the lid is removed (residues 190-202) since Sung and colleagues suggest that it would be displaced upon the binding of nucleotide[67].

Protein Expression and Purification

Wild-type mouse Grp94 (72-765) with the charged-linker removed (Δ287-328), its variants (N91C, L163A, F199A, N91C/L163A, and N91C/F199A), the BiP NBD (27-411), and its variant (D27C) were all expressed in *E. coli* BL21 cells in pET151D vectors which contain a 6X His-tag and TEV cleavage site. All proteins were first purified by Ni-NTA affinity chromatography and the 6X His-tag was cleaved with TEV protease. Subsequent Ni-NTA affinity chromatography

removed 6X His-tag and TEV and anion exchange chromatography removed bound nucleotide. Proteins were buffer exchanged with size exclusion chromatography into storage buffers. Grp94 was stored in 25mM Tris pH 7.5, 75mM KCl, 1mM BME, and 5% Glycerol. BiP NBD was stored in 25mM Tris pH 7.5, 50mM KCl, 1mM BME, and 5% Glycerol.

Thermal Shift Assay

Measurements were performed on a StepOnePlus™ Real-Time PCR System (Applied Biosystems). The temperature was increased by 0.3°C/min from 10 to 95°C and protein unfolding was monitored by the fluorescence of Sypro Orange. Experimental conditions consist of 4μM Grp94, 1X Sypro Orange, 25mM HEPES pH 7.5, 60mM KCl, 5mM $MgCl_2$ and, for experiments including ligands, 5mM ADP or 50μM inhibitor. To determine the T_m, the fluorescence data was fit to a Boltzmann sigmoidal curve as previously described[165].

Fluorescence Polarization

The D27C variant of the BiP NBD was labeled with FITC as previously described[12]. Fluorescence polarization measurements were performed with 50nM FITC-labeled BiP NBD on a Fluoromax-4 spectrofluorometer (Horiba Scientific). Fluorometer setup had an excitation wavelength of 493nm and an emission wavelength of 518nm with 6nm slit widths, and an integration time of 1 second. Buffer conditions consist of 25mM HEPES pH 8.0, 50mM KCl, 0.6mM $MgCl_2$, 2% DMSO v/v, 1mM BME, and 0.75mg/mL BSA at 37°C. Samples were incubated for 10 minutes prior to the addition of Grp94. For all FP experiments, the 30-minute time point was used in calculating the K_D. K_D values were calculated using the single-site binding equation:

$$P = \frac{a[x]}{K_D + [x]} + c \quad (1)$$

Where *P* is polarization, *a* is the polarization amplitude, *c* is the polarization value in the absence of Grp94, and *x* is the concentration of Grp94. All Grp94 titrations to determine K_D values were from multiple separate experiments, each with a different concentration of Grp94.

Grp94 Bulk FRET

The N91C, N91C/L163A, and N91C/F199A Grp94 variants were labeled with Alexa Fluor 555 (donor) and Alexa Fluor 647 (acceptor) as previously described[85]. Grp94 bulk FRET experiments were started by mixing 125nm donor-labeled and 125nm acceptor-labeled Grp94 and incubating at room temperature for 1.5 hours to monomer exchange. Experimental conditions consist of 25mM HEPES pH 8.0, 50mM KCl, 0.6mM $MgCl_2$, 1mM BME, 2% DMSO v/v, and 0.75mg/mL BSA at 37°C for the N91C and N91C/L163A variants and 35°C for the N91C/F199A variant. For samples with inhibitor 50μM was used and samples with ADP used 1mM with a matching concentration of $MgCl_2$ added. Bulk FRET data was collected with a Fluoromax-4 spectrofluorometer (Horiba Scientific) with a donor excitation wavelength of 532nm and donor and acceptor emission wavelengths of 565nm and 670nm respectively. Slit widths were set to 1.5nm for excitation and 4.5nm for emission, with an integration time of 0.5 seconds. FRET efficiency (E) was calculated by the donor (D) and acceptor (A) emission fluorescence:

$$E = \frac{A}{D + A} \quad (2)$$

All data points were from multiple separate experiments, each with a different concentration of BiP NBD. FRET efficiency change was calculated by subtracting the lowest FRET efficiency value of a dataset from all data points (dataset includes Apo, AUY922, ADP, Hsp990, and XL888

FRET measurements for a singular Grp94 variant). FRET efficiency change was normalized by dividing all data points by the maximal FRET efficiency change value in a dataset.

ATPase Assay

Grp94 ATPase was measured by depletion of NADH via an enzyme-linked assay with pyruvate kinase and lactate dehydrogenase on a plate reader (BioTek)[152]. NADH depletion was monitored at an absorbance of 340nm. Backgrounds were collected for 30 minutes to 1 hour prior to the addition of Grp94. For ATPase measurements shown in Figure 4.7, 2μM Grp94 dimer was assayed in 25mM Tris pH 7.5, 50mM KCl, 1mM $MgCl_2$, 1 mg/mL BSA, 0.1μM Lactate Dehydrogenase, 0.1μM Pyruvate Kinase, 0.4mM PEP, and 0.4mM NADH at 30°C. For samples with inhibitor, 50μM was used. For F199A with and without BiP, F199A with BiP and Hsp990, and all samples with XL888, 50μM of ATP was used. All other samples used 1mM ATP. The ATPase rate is reported per dimer of Grp94.

For ATPase measurements shown in Figure 4.11.A, 1.5μM Grp94 dimer was assayed in 25mM HEPES pH 7.5, 150mM KCl, 2.5mM $MgCl_2$, 0.5% DMSO v/v, 0.1μM Lactate Dehydrogenase, 0.1μM Pyruvate Kinase, 0.4mM PEP, and 0.4mM NADH at 35°C. The ATPase rate is reported per dimer of Grp94. ATPase measurements (A) were fit assuming there are two different activities whether one or two ATP molecules are bound to a Grp94 dimer:

$$A = \frac{v_1 \times \frac{2 \times [ATP]}{K_D} + v_2 \times \frac{[ATP]^2}{(K_D)^2}}{1 + \frac{2 \times [ATP]}{K_D} + \frac{[ATP]^2}{(K_D)^2}} \quad (3)$$

Where v_1 is the ATPase rate with one ATP molecule bound, v_2 is the ATPase rate with two ATP molecules bound, and K_D is the dissociation constant for the binding of one ATP molecule to a Grp94 dimer. Derivation can be found in LaRussa, SA (2023)[158].

Single Molecule FRET

Grp94 with a C-terminal SNAP tag was selectively biotinylated using a benzyl-guanine derivative as described previously[85]. Acceptor-labeled SNAP-Grp94 and donor-labeled Grp94 were monomer exchanged in 50mM HEPES pH 8.0, 50mM KCl, 0.6mM $MgCl_2$, 2mM BME, and 0.5mg/mL BSA at 30°C for 2 hours. Glass slides and coverslips were prepared as discussed previously[85]. Grp94 was applied to the slide after dilution to 1nM with an oxygen scavenging system (0.4% Glucose, 1.5units/μL Catalase, 0.04units/μL Glucose Oxidase) and triplet-state quencher cocktail (2mM Propyl Galate, 2mM 4-nitrobenzyl alcohol, 4mM Trolox). For experiments with ADP and inhibitors, the Grp94 sample was preincubated with the ligands. In relevant experiments, BiP NBD was then applied to the slide. Single molecule TIRF imaging was performed on a custom microscope as previously described[85]. smFRET measurements include donor fluorophore excitation with a laser power of 650μW at 532nm and acceptor fluorophore excitation with a laser power of 150μW at 633nm. Alternating excitation experiments have a sampling interval of 2.4 seconds with a signal integration time of 1 second.

In order for background fluorescence to be subtracted for both the donor and acceptor signals, smFRET analysis was only performed on molecules with a recorded donor photobleaching event. FRET efficiency values were only calculated for time points where both the donor and acceptor fluorophores were not photobleached. The smFRET efficiency (E) is calculated as

$$E = \frac{A}{(\gamma \times D + A)} \tag{4}$$

Where *A* is the acceptor emission, *D* is the donor emission, and the γ value is 1.75 as determined by a previous analysis of Grp94[85]. FRET efficiency histograms were constructed by compiling the efficiency values for each frame for each molecule.

REFERENCES

1. Verghese Jacob, Abrams Jennifer, Wang Yanyu, & Morano Kevin A. Biology of the Heat Shock Response and Protein Chaperones: Budding Yeast (Saccharomyces cerevisiae) as a Model System. *Microbiol. Mol. Biol. Rev.* **76**, 115–158 (2012).

2. Schopf, F. H., Biebl, M. M. & Buchner, J. The HSP90 chaperone machinery. *Nat. Rev. Mol. Cell Biol.* **18**, 345–360 (2017).

3. Kampinga, H. H. & Craig, E. A. The HSP70 chaperone machinery: J proteins as drivers of functional specificity. *Nat. Rev. Mol. Cell Biol.* **11**, 579–592 (2010).

4. Rosenzweig, R., Nillegoda, N. B., Mayer, M. P. & Bukau, B. The Hsp70 chaperone network. *Nat. Rev. Mol. Cell Biol.* **20**, 665–680 (2019).

5. Franco, A. *et al.* All-or-none amyloid disassembly via chaperone-triggered fibril unzipping favors clearance of α-synuclein toxic species. *Proc. Natl. Acad. Sci.* **118**, e2105548118 (2021).

6. Boulon, S. *et al.* HSP90 and Its R2TP/Prefoldin-like Cochaperone Are Involved in the Cytoplasmic Assembly of RNA Polymerase II. *Mol. Cell* **39**, 912–924 (2010).

7. Genest, O., Wickner, S. & Doyle, S. M. Hsp90 and Hsp70 chaperones: Collaborators in protein remodeling. *J. Biol. Chem.* **294**, 2109–2120 (2019).

8. Genest, O., Hoskins, J. R., Kravats, A. N., Doyle, S. M. & Wickner, S. Hsp70 and Hsp90 of E. coli directly interact for collaboration in protein remodeling. *J. Mol. Biol.* **427**, 3877–3889 (2015).

9. Kravats, A. N. *et al.* Interaction of E. coli Hsp90 with DnaK involves the DnaJ binding region of DnaK. *J. Mol. Biol.* **429**, 858–872 (2017).

10. Kravats, A. N. *et al.* Functional and physical interaction between yeast Hsp90 and Hsp70. *Proc. Natl. Acad. Sci.* **115**, E2210–E2219 (2018).

11. Doyle, S. M. *et al.* Intermolecular Interactions between Hsp90 and Hsp70. *J. Mol. Biol.* **431**, 2729–2746 (2019).

12. Sun, M., Kotler, J. L. M., Liu, S. & Street, T. O. The endoplasmic reticulum (ER) chaperones BiP and Grp94 selectively associate when BiP is in the ADP conformation. *J. Biol. Chem.* **294**, 6387–6396 (2019).

13. Wang, R. Y.-R. *et al.* Structure of Hsp90–Hsp70–Hop–GR reveals the Hsp90 client-loading mechanism. *Nature* **601**, 460–464 (2022).

14. Butler, L. M., Ferraldeschi, R., Armstrong, H. K., Centenera, M. M. & Workman, P. Maximizing the Therapeutic Potential of HSP90 Inhibitors. *Mol. Cancer Res.* **13**, 1445–1451 (2015).

15. Miyata, Y., Nakamoto, H. & Neckers, L. The Therapeutic Target Hsp90 and Cancer Hallmarks. *Curr. Pharm. Des.* **19**, 347–365 (2013).

16. Rodina, A. *et al.* The epichaperome is an integrated chaperome network that facilitates tumour survival. **Nature**, 397–401 (2016).

17. Moran Luengo, T., Kityk, R., Mayer, M. P. & Rudiger, S. G. D. Hsp90 Breaks the Deadlock of the Hsp70 Chaperone System. *Mol Cell* **70**, 545-552 e9 (2018).

18. Patel, P. D. *et al.* Paralog-selective Hsp90 inhibitors define tumor-specific regulation of HER2. *Nat. Chem. Biol.* **9**, 677–684 (2013).

19. Mayer, M. P. Hsp70 chaperone dynamics and molecular mechanism. *Trends Biochem. Sci.* **38**, 507–514 (2013).

20. Yang, J., Nune, M., Zong, Y., Zhou, L. & Liu, Q. Close and Allosteric Opening of the Polypeptide-Binding Site in a Human Hsp70 Chaperone BiP. *Structure* **23**, 2191–2203 (2015).

21. Bertelsen, E. B., Chang, L., Gestwicki, J. E. & Zuiderweg, E. R. P. Solution conformation of wild-type E. coli Hsp70 (DnaK) chaperone complexed with ADP and substrate. *Proc. Natl. Acad. Sci. U. S. A.* **106**, 8471–8476 (2009).

22. Voith von Voithenberg, L. *et al.* Comparative analysis of the coordinated motion of Hsp70s from different organelles observed by single-molecule three-color FRET. *Proc. Natl. Acad. Sci.* **118**, e2025578118 (2021).

23. Wang, W., Liu, Q., Liu, Q. & Hendrickson, W. A. Conformational equilibria in allosteric control of Hsp70 chaperones. *Mol. Cell* **81**, 3919-3933.e7 (2021).

24. Preissler, S. *et al.* Physiological modulation of BiP activity by trans-protomer engagement of the interdomain linker. *eLife* **4**, e08961 (2015).

25. Kityk, R., Kopp, J. & Mayer, M. P. Molecular Mechanism of J-Domain-Triggered ATP Hydrolysis by Hsp70 Chaperones. *Mol. Cell* **69**, 227-237.e4 (2018).

26. Harrison, C. GrpE, a nucleotide exchange factor for DnaK. *Cell Stress Chaperones* **8**, 218–224 (2003).

27. Behnke, J., Feige, M. J. & Hendershot, L. M. BiP and Its Nucleotide Exchange Factors Grp170 and Sil1: Mechanisms of Action and Biological Functions. *J. Mol. Biol.* **427**, 1589–1608 (2015).

28. Clerico, E. M., Tilitsky, J. M., Meng, W. & Gierasch, L. M. How Hsp70 Molecular Machines Interact with Their Substrates to Mediate Diverse Physiological Functions. *J. Mol. Biol.* **427**, 1575–1588 (2015).

29. Fourie, A. M., Sambrook, J. F. & Gething, M. J. Common and divergent peptide binding specificities of hsp70 molecular chaperones. *J. Biol. Chem.* **269**, 30470–30478 (1994).

30. Rüdiger, S., Germeroth, L., Schneider-Mergener, J. & Bukau, B. Substrate specificity of the DnaK chaperone determined by screening cellulose-bound peptide libraries. *EMBO J.* **16**, 1501–1507 (1997).

31. Zhu, X. *et al.* Structural Analysis of Substrate Binding by the Molecular Chaperone DnaK. *Science* **272**, 1606–1614 (1996).

32. Zahn, M. *et al.* Structural Studies on the Forward and Reverse Binding Modes of Peptides to the Chaperone DnaK. *J. Mol. Biol.* **425**, 2463–2479 (2013).

33. Clerico, E. M. *et al.* Selective promiscuity in the binding of E. coli Hsp70 to an unfolded protein. *Proc. Natl. Acad. Sci.* **118**, e2016962118 (2021).

34. Jin, Y. *et al.* The ER chaperones BiP and Grp94 regulate the formation of insulin-like growth factor 2 (IGF2) oligomers. *J. Mol. Biol.* 166963 (2021) doi:10.1016/j.jmb.2021.166963.

35. Kundel, F. *et al.* Hsp70 Inhibits the Nucleation and Elongation of Tau and Sequesters Tau Aggregates with High Affinity. *ACS Chem. Biol.* **13**, 636–646 (2018).

36. Soto, C. & Pritzkow, S. Protein misfolding, aggregation, and conformational strains in neurodegenerative diseases. *Nat. Neurosci.* **21**, 1332–1340 (2018).

37. Wentink, A. S. *et al.* Molecular dissection of amyloid disaggregation by human HSP70. *Nature* 1–6 (2020) doi:10.1038/s41586-020-2904-6.

38. Greene, L. E., Zinner, R., Naficy, S. & Eisenberg, E. Effect of Nucleotide on the Binding of Peptides to 70-kDa Heat Shock Protein (∗). *J. Biol. Chem.* **270**, 2967–2973 (1995).

39. Dollins, D. E., Warren, J. J., Immormino, R. M. & Gewirth, D. T. Structures of GRP94-nucleotide complexes reveal mechanistic differences between the hsp90 chaperones. *Mol. Cell* **28**, 41–56 (2007).

40. Huck, J. D., Que, N. L., Hong, F., Li, Z. & Gewirth, D. T. Structural and Functional Analysis of GRP94 in the Closed State Reveals an Essential Role for the Pre-N Domain and a Potential Client-Binding Site. *Cell Rep.* **20**, 2800–2809 (2017).

41. Hessling, M., Richter, K. & Buchner, J. Dissection of the ATP-induced conformational cycle of the molecular chaperone Hsp90. *Nat Struct Mol Biol* **16**, 287–93 (2009).

42. Lee, B. L. *et al.* The Hsp90 Chaperone: 1H and 19F Dynamic Nuclear Magnetic Resonance Spectroscopy Reveals a Perfect Enzyme. *Biochemistry* **58**, 1869–1877 (2019).

43. Wolmarans, A., Lee, B., Spyracopoulos, L. & LaPointe, P. The Mechanism of Hsp90 ATPase Stimulation by Aha1. *Sci. Rep.* **6**, 33179 (2016).

44. McLaughlin, S. H. *et al.* The Co-chaperone p23 Arrests the Hsp90 ATPase Cycle to Trap Client Proteins. *J. Mol. Biol.* **356**, 746–758 (2006).

45. Prodromou, C. *et al.* Regulation of Hsp90 ATPase activity by tetratricopeptide repeat (TPR)-domain co-chaperones. *EMBO J.* **18**, 754–762 (1999).

46. Motojima-Miyazaki, Y., Yoshida, M. & Motojima, F. Ribosomal protein L2 associates with E. coli HtpG and activates its ATPase activity. *Biochem. Biophys. Res. Commun.* **400**, 241–245 (2010).

47. Street, T. O., Lavery, L. A. & Agard, D. A. Substrate Binding Drives Large-Scale Conformational Changes in the Hsp90 Molecular Chaperone. *Mol. Cell* **42**, 96–105 (2011).

48. Jin, Y., Hoxie, R. S. & Street, T. O. Molecular mechanism of bacterial Hsp90 pH-dependent ATPase activity. *Protein Sci. Publ. Protein Soc.* **26**, 1206–1213 (2017).

49. Halpin, J. C., Huang, B., Sun, M. & Street, T. O. Crowding Activates Heat Shock Protein 90. *J. Biol. Chem.* jbc.M115.702928 (2016) doi:10.1074/jbc.M115.702928.

50. Nathan D F & Lindquist S. Mutational analysis of Hsp90 function: interactions with a steroid receptor and a protein kinase. *Mol. Cell. Biol.* **15**, 3917–3925 (1995).

51. Bohen, S. P. & Yamamoto, K. R. Isolation of Hsp90 mutants by screening for decreased steroid receptor function. *Proc. Natl. Acad. Sci.* **90**, 11424–11428 (1993).

52. Noddings, C. M., Wang, R. Y.-R., Johnson, J. L. & Agard, D. A. Structure of Hsp90–p23–GR reveals the Hsp90 client-remodelling mechanism. *Nature* **601**, 465–469 (2022).

53. Verba, K. A. *et al.* Atomic structure of Hsp90-Cdc37-Cdk4 reveals that Hsp90 traps and stabilizes an unfolded kinase. *Science* **352**, 1542–1547 (2016).

54. Genest, O. *et al.* Uncovering a region of heat shock protein 90 important for client binding in E. coli and chaperone function in yeast. *Mol. Cell* **49**, 464–473 (2013).

55. Street, T. O. *et al.* Cross-monomer substrate contacts reposition the Hsp90 N-terminal domain and prime the chaperone activity. *J. Mol. Biol.* **415**, 3–15 (2012).

56. Weickert, S., Wawrzyniuk, M., John, L. H., Rüdiger, S. G. D. & Drescher, M. The mechanism of Hsp90-induced oligomerization of Tau. *Sci. Adv.* **6**, (2020).

57. Tortosa, E. *et al.* Binding of Hsp90 to Tau Promotes a Conformational Change and Aggregation of Tau Protein. *J. Alzheimers Dis.* **17**, 319–325 (2009).

58. Huard, D. J. E., Jonke, A. P., Torres, M. P. & Lieberman, R. L. Different Grp94 components interact transiently with the myocilin olfactomedin domain in vitro to enhance or retard its amyloid aggregation. *Sci. Rep.* **9**, 12769 (2019).

59. Daturpalli, S., Waudby, C. A., Meehan, S. & Jackson, S. E. Hsp90 inhibits alpha-synuclein aggregation by interacting with soluble oligomers. *J Mol Biol* **425**, 4614–28 (2013).

60. Amankwah, Y. S. *et al.* Grp94 Works Upstream of BiP in Protein Remodeling Under Heat Stress. *J. Mol. Biol.* **434**, 167762 (2022).

61. Smith, D. F., Stensgard, B. A., Welch, W. J. & Toft, D. O. Assembly of progesterone receptor with heat shock proteins and receptor activation are ATP mediated events. *J. Biol. Chem.* **267**, 1350–1356 (1992).

62. Smith, D. F. *et al.* Identification of a 60-Kilodalton Stress-Related Protein, p60, which Interacts with hsp90 and hsp70. *Mol. Cell. Biol.* **13**, 869–876 (1993).

63. Chen, S., Prapapanich, V., Rimerman, R. A., Honoré, B. & Smith, D. F. Interactions of p60, a mediator of progesterone receptor assembly, with heat shock proteins hsp90 and hsp70. *Mol. Endocrinol.* **10**, 682–693 (1996).

64. Hutchison, K. A., Dittmar, K. D., Czar, M. J. & Pratt, W. B. Proof that hsp70 is required for assembly of the glucocorticoid receptor into a heterocomplex with hsp90. *J. Biol. Chem.* **269**, 5043–5049 (1994).

65. Biebl, M. M. *et al.* NudC guides client transfer between the Hsp40/70 and Hsp90 chaperone systems. *Mol. Cell* **82**, 555-569.e7 (2022).

66. Genest, O., Hoskins, J. R., Camberg, J. L., Doyle, S. M. & Wickner, S. Heat shock protein 90 from Escherichia coli collaborates with the DnaK chaperone system in client protein remodeling. *Proc Natl Acad Sci U A* **108**, 8206–11 (2011).

67. Sung, N. *et al.* 2.4 Å resolution crystal structure of human TRAP1NM, the Hsp90 paralog in the mitochondrial matrix. *Acta Crystallogr Struct Biol* **72**, 904–11 (2016).

68. Jansen, G. *et al.* An Interaction Map of Endoplasmic Reticulum Chaperones and Foldases. *Mol. Cell. Proteomics* **11**, 710–723 (2012).

69. Melnick, J., Aviel, S. & Argon, Y. The endoplasmic reticulum stress protein GRP94, in addition to BiP, associates with unassembled immunoglobulin chains. *J Biol Chem* **267**, 21303–6 (1992).

70. Melnick, J., Dul, J. & Argon, Y. Sequential interaction of the chaperones BiP and Grp94 with immunoglobulin chains in the endoplasmic reticulum. *Nature* **370**, 373–375 (1994).

71. Morishima, Y., Murphy, P. J., Li, D. P., Sanchez, E. R. & Pratt, W. B. Stepwise assembly of a glucocorticoid receptor.hsp90 heterocomplex resolves two sequential ATP-dependent events involving first hsp70 and then hsp90 in opening of the steroid binding pocket. *J Biol Chem* **275**, 18054–60 (2000).

72. Wegele, H., Wandinger, S. K., Schmid, A. B., Reinstein, J. & Buchner, J. Substrate transfer from the chaperone Hsp70 to Hsp90. *J Mol Biol* **356**, 802–11 (2006).

73. Kirschke, E., Goswami, D., Southworth, D., Griffin, P. R. & Agard, D. Glucocorticoid Receptor Function Regulated by Coordinated Action of the Hsp90 and Hsp70 Chaperone Cycles. *Cell* **157**, 1685–1697 (2014).

74. Bertolotti, A., Zhang, Y., Hendershot, L. M., Harding, H. P. & Ron, D. Dynamic interaction of BiP and ER stress transducers in the unfolded-protein response. *Nat. Cell Biol.* **2**, 326–332 (2000).

75. Shen, J., Chen, X., Hendershot, L. & Prywes, R. ER Stress Regulation of ATF6 Localization by Dissociation of BiP/GRP78 Binding and Unmasking of Golgi Localization Signals. *Dev. Cell* **3**, 99–111 (2002).

76. Okamura, K., Kimata, Y., Higashio, H., Tsuru, A. & Kohno, K. Dissociation of Kar2p/BiP from an ER Sensory Molecule, Ire1p, Triggers the Unfolded Protein Response in Yeast. *Biochem. Biophys. Res. Commun.* **279**, 445–450 (2000).

77. Carrara, M., Prischi, F. & Ali, M. M. U. UPR Signal Activation by Luminal Sensor Domains. *Int. J. Mol. Sci.* **14**, 6454–6466 (2013).

78. Wei, J. & Hendershot, L. M. Characterization of the Nucleotide Binding Properties and ATPase Activity of Recombinant Hamster BiP Purified from Bacteria (∗). *J. Biol. Chem.* **270**, 26670–26676 (1995).

79. Kadowaki, H. & Nishitoh, H. Signaling Pathways from the Endoplasmic Reticulum and Their Roles in Disease. *Genes* **4**, 306–333 (2013).

80. Huang, B. *et al.* The endoplasmic reticulum chaperone BiP is a closure-accelerating cochaperone of Grp94. *Proc. Natl. Acad. Sci.* **119**, e2118793119 (2022).

81. Sung, N. *et al.* Mitochondrial Hsp90 is a ligand-activated molecular chaperone coupling ATP binding to dimer closure through a coiled-coil intermediate. *Proc. Natl. Acad. Sci.* **113**, 2952–2957 (2016).

82. Halpin, J. C. & Street, T. O. Hsp90 Sensitivity to ADP Reveals Hidden Regulation Mechanisms. *J. Mol. Biol.* **429**, 2918–2930 (2017).

83. Elnatan, D. *et al.* Symmetry broken and rebroken during the ATP hydrolysis cycle of the mitochondrial Hsp90 TRAP1. *eLife* **6**, e25235 (2017).

84. Ratzke, C., Berkemeier, F. & Hugel, T. Heat shock protein 90's mechanochemical cycle is dominated by thermal fluctuations. *Proc. Natl. Acad. Sci.* **109**, 161–166 (2012).

85. Huang, B., Friedman, L. J., Sun, M., Gelles, J. & Street, T. O. Conformational Cycling within the Closed State of Grp94, an Hsp90-Family Chaperone. *J. Mol. Biol.* **431**, 3312–3323 (2019).

86. Flynn, J. M. *et al.* Comprehensive fitness maps of Hsp90 show widespread environmental dependence. *eLife* **9**, e53810 (2020).

87. Hoxie, R. S. Energetic Studies of Hsp90 Inhibitors and Conformational Studies of Hsp90. *ProQuest Dissertations and Theses* (Brandeis University, 2021).

88. Bergman, D., Halje, M., Nordin, M. & Engström, W. Insulin-Like Growth Factor 2 in Development and Disease: A Mini-Review. *Gerontology* **59**, 240–249 (2013).

89. Löfqvist, C. *et al.* Reference Values for IGF-I throughout Childhood and Adolescence: A Model that Accounts Simultaneously for the Effect of Gender, Age, and Puberty. *J. Clin. Endocrinol. Metab.* **86**, 5870–5876 (2001).

90. Sferruzzi-Perri, A. N., Sandovici, I., Constancia, M. & Fowden, A. L. Placental phenotype and the insulin-like growth factors: resource allocation to fetal growth. *J. Physiol.* **595**, 5057–5093 (2017).

91. Duguay, S. J. *et al.* Post-translational Processing of the Insulin-like Growth Factor-2 Precursor ANALYSIS OF O-GLYCOSYLATION AND ENDOPROTEOLYSIS. *J. Biol. Chem.* **273**, 18443–18451 (1998).

92. Cornish, J. *et al.* Preptin, another peptide product of the pancreatic β-cell, is osteogenic in vitro and in vivo. *Am. J. Physiol.-Endocrinol. Metab.* **292**, E117–E122 (2007).

93. Ostrovsky, O., Ahmed, N. T. & Argon, Y. The Chaperone Activity of GRP94 Toward Insulin-like Growth Factor II Is Necessary for the Stress Response to Serum Deprivation. *Mol. Biol. Cell* **20**, 1855–1864 (2009).

94. Ostrovsky, O., Eletto, D., Makarewich, C., Barton, E. R. & Argon, Y. Glucose regulated protein 94 is required for muscle differentiation through its control of the autocrine production of insulin-like growth factors. *Biochim. Biophys. Acta BBA - Mol. Cell Res.* **1803**, 333–341 (2010).

95. Wanderling, S. *et al.* GRP94 Is Essential for Mesoderm Induction and Muscle Development Because It Regulates Insulin-like Growth Factor Secretion. *Mol. Biol. Cell* **18**, 3764–3775 (2007).

96. Ostrovsky, O., Makarewich, C. A., Snapp, E. L. & Argon, Y. An essential role for ATP binding and hydrolysis in the chaperone activity of GRP94 in cells. *Proc. Natl. Acad. Sci.* **106**, 11600–11605 (2009).

97. Ghiasi, S. M. *et al.* Endoplasmic Reticulum Chaperone Glucose-Regulated Protein 94 Is Essential for Proinsulin Handling. *Diabetes* **68**, 747–760 (2019).

98. Marzec, M. *et al.* A Human Variant of Glucose-Regulated Protein 94 That Inefficiently Supports IGF Production. *Endocrinology* **157**, 1914–1928 (2016).

99. Lorenson, M. Y., Patel, T., Liu, J. W. & Walker, A. M. Prolactin (PRL) is a zinc-binding protein. I. Zinc interactions with monomeric PRL and divalent cation protection of intragranular PRL cysteine thiols. *Endocrinology* **137**, 809–16 (1996).

100. Baumann, G. P. Growth hormone isoforms. *Growth Horm IGF Res* **19**, 333–40 (2009).

101. Noormägi, A., Gavrilova, J., Smirnova, J., Tõugu, V. & Palumaa, P. Zn(II) ions co-secreted with insulin suppress inherent amyloidogenic properties of monomeric insulin. *Biochem J* **430**, 511–8 (2010).

102. Erthal, L. C. *et al.* Regulation of the assembly and amyloid aggregation of murine amylin by zinc. *Biophys Chem* **218**, 58–70 (2016).

103. Mayer, M. P. & Gierasch, L. M. Recent advances in the structural and mechanistic aspects of Hsp70 molecular chaperones. *J. Biol. Chem.* **294**, 2085–2097 (2019).

104. Mayer, M. P. & Bukau, B. Hsp70 chaperones: Cellular functions and molecular mechanism. *Cell. Mol. Life Sci.* **62**, 670–684 (2005).

105. Imamoglu, R., Balchin, D., Hayer-Hartl, M. & Hartl, F. U. Bacterial Hsp70 resolves misfolded states and accelerates productive folding of a multi-domain protein. *Nat. Commun.* **11**, 365 (2020).

106. UCSF Chimera—A visualization system for exploratory research and analysis - Pettersen - 2004 - Journal of Computational Chemistry - Wiley Online Library.

107. Klimstra, W. B., Heidner, H. W. & Johnston, R. E. The Furin Protease Cleavage Recognition Sequence of Sindbis Virus PE2 Can Mediate Virion Attachment to Cell Surface Heparan Sulfate. *J. Virol.* **73**, 6299–6306 (1999).

108. Xue, B., Dunbrack, R. L., Williams, R. W., Dunker, A. K. & Uversky, V. N. PONDR-FIT: A Meta-Predictor of Intrinsically Disordered Amino Acids. *Biochim. Biophys. Acta* **1804**, 996–1010 (2010).

109. Sferruzzi-Perri, A. N., Sandovici, I., Constancia, M. & Fowden, A. L. Placental phenotype and the insulin-like growth factors: resource allocation to fetal growth. *J. Physiol.* **595**, 5057–5093 (2017).

110. Qiu, Q., Basak, A., Mbikay, M., Tsang, B. K. & Gruslin, A. Role of pro-IGF-II processing by proprotein convertase 4 in human placental development. *Proc. Natl. Acad. Sci. U. S. A.* **102**, 11047–11052 (2005).

111. Basak, A. *et al.* Enzymic characterization in vitro of recombinant proprotein convertase PC4. *Biochem. J.* **343 Pt 1**, 29–37 (1999).

112. Cheng, K.-C. *et al.* Characterization of preptin-induced insulin secretion in pancreatic β-cells. *J. Endocrinol.* **215**, 43–49 (2012).

113. Yang, G. *et al.* Circulating preptin levels in normal, impaired glucose tolerance, and type 2 diabetic subjects. *Ann. Med.* **41**, 52–56 (2009).

114. Valenzano, K. J., Heath-Monnig, E., Tollefsen, S. E., Lake, M. & Lobel, P. Biophysical and Biological Properties of Naturally Occurring High Molecular Weight Insulin-like Growth Factor II Variants. *J. Biol. Chem.* **272**, 4804–4813 (1997).

115. Maji, S. K. *et al.* Functional Amyloids As Natural Storage of Peptide Hormones in Pituitary Secretory Granules. *Science* **325**, 328–332 (2009).

116. Marcinowski, M. *et al.* Substrate discrimination of the chaperone BiP by autonomous and cochaperone-regulated conformational transitions. *Nat. Struct. Mol. Biol.* **18**, 150–158 (2011).

117. Rosam, M. *et al.* Bap (Sil1) regulates the molecular chaperone BiP by coupling release of nucleotide and substrate. *Nat. Struct. Mol. Biol.* **25**, 90–100 (2018).

118. Banerjee, R., Jayaraj, G. G., Peter, J. J., Kumar, V. & Mapa, K. Monitoring conformational heterogeneity of the lid of DnaK substrate-binding domain during its chaperone cycle. *FEBS J.* **283**, 2853–2868 (2016).

119. Liu, S. & Street, T. O. 5′-N-ethylcarboxamidoadenosine is not a paralog-specific Hsp90 inhibitor. *Protein Sci.* **25**, 2209–2215 (2016).

120. Takeda, S. & McKay, D. B. Kinetics of Peptide Binding to the Bovine 70 kDa Heat Shock Cognate Protein, a Molecular Chaperone. *Biochemistry* **35**, 4636–4644 (1996).

121. Schneider, M. *et al.* BiPPred: Combined sequence- and structure-based prediction of peptide binding to the Hsp70 chaperone BiP. *Proteins Struct. Funct. Bioinforma.* **84**, 1390–1407 (2016).

122. Phillips, R. B., Kondev, Jane, Theriot, J., Garcia, H. G. & Orme, N. *Physical biology of the cell*. (2013).

123. Kegel, W. K. & Schoot, P. van der. Competing Hydrophobic and Screened-Coulomb Interactions in Hepatitis B Virus Capsid Assembly. *Biophys. J.* **86**, 3905–3913 (2004).

124. Muchowski, P. J. & Wacker, J. L. Modulation of neurodegeneration by molecular chaperones. *Nat. Rev. Neurosci.* **6**, 11–22 (2005).

125. Feige, M. J. *et al.* An unfolded CH1 domain controls the assembly and secretion of IgG antibodies. *Mol. Cell* **34**, 569–579 (2009).

126. Buchanan, C. M., Peng, Z., Cefre, A. & Sarojini, V. Preptin Analogues: Chemical Synthesis, Secondary Structure and Biological Studies. *Chem. Biol. Drug Des.* **82**, 429–437 (2013).

127. Jiang, Y., Fu, H., Springer, T. A. & Wong, W. P. Electrostatic Steering Enables Flow-Activated Von Willebrand Factor to Bind Platelet Glycoprotein, Revealed by Single-Molecule Stretching and Imaging. *J. Mol. Biol.* **431**, 1380–1396 (2019).

128. Flechtner, J. B. *et al.* High-Affinity Interactions between Peptides and Heat Shock Protein 70 Augment CD8+ T Lymphocyte Immune Responses. *J. Immunol.* **177**, 1017–1027 (2006).

129. Chilukoti, N. *et al.* Hsp70 Inhibits Aggregation of IAPP by Binding to the Heterogeneous Prenucleation Oligomers. *Biophys. J.* **120**, 476–488 (2021).

130. Sarkar, M., Kuret, J. & Lee, G. Two motifs within the tau microtubule-binding domain mediate its association with the hsc70 molecular chaperone. *J. Neurosci. Res.* **86**, 2763–2773 (2008).

131. Kopp, M. C., Larburu, N., Durairaj, V., Adams, C. J. & Ali, M. M. UPR proteins IRE1 and PERK switch BiP from chaperone to ER stress sensor. *Nat. Struct. Mol. Biol.* **26**, 1053–1062 (2019).

132. Yang, J. *et al.* Conformation transitions of the polypeptide-binding pocket support an active substrate release from Hsp70s. *Nat. Commun.* **8**, 1201 (2017).

133. Maeda, H. *et al.* Biological Heterogeneity of the Peptide-binding Motif of the 70-kDa Heat Shock Protein by Surface Plasmon Resonance Analysis*. *J. Biol. Chem.* **282**, 26956–26962 (2007).

134. Siegenthaler, R. K. & Christen, P. Tuning of DnaK Chaperone Action by Nonnative Protein Sensor DnaJ and Thermosensor GrpE. *J. Biol. Chem.* **281**, 34448–34456 (2006).

135. Sekhar, A., Rosenzweig, R., Bouvignies, G. & Kay, L. E. Mapping the conformation of a client protein through the Hsp70 functional cycle. *Proc. Natl. Acad. Sci.* **112**, 10395–10400 (2015).

136. McCarty, J. S. *et al.* Regulatory Region C of theE. coliHeat Shock Transcription Factor, σ32, Constitutes a DnaK Binding Site and is Conserved Among Eubacteria. *J. Mol. Biol.* **256**, 829–837 (1996).

137. Gamer, J. *et al.* A cycle of binding and release of the DnaK, DnaJ and GrpE chaperones regulates activity of the Escherichia coli heat shock transcription factor sigma32. *EMBO J.* **15**, 607–617 (1996).

138. Stetefeld, J., McKenna, S. A. & Patel, T. R. Dynamic light scattering: a practical guide and applications in biomedical sciences. *Biophys. Rev.* **8**, 409–427 (2016).

139. Ebong, I. *et al.* Heterogeneity and dynamics in the assembly of the Heat Shock Protein 90 chaperone complexes. *Proc. Natl. Acad. Sci.* **108**, 17939–17944 (2011).

140. Murphy, P. J. M., Kanelakis, K. C., Galigniana, M. D., Morishima, Y. & Pratt, W. B. Stoichiometry, Abundance, and Functional Significance of the hsp90/hsp70-based Multiprotein Chaperone Machinery in Reticulocyte Lysate *. *J. Biol. Chem.* **276**, 30092–30098 (2001).

141. Bhattacharya, K. *et al.* The Hsp70-Hsp90 co-chaperone Hop/Stip1 shifts the proteostatic balance from folding towards degradation. *Nat. Commun.* **11**, 5975 (2020).

142. Presman, D. M. & Hager, G. L. More than meets the dimer: What is the quaternary structure of the glucocorticoid receptor? *Transcription* **8**, 32–39 (2017).

143. Presman, D. M. *et al.* DNA binding triggers tetramerization of the glucocorticoid receptor in live cells. *Proc. Natl. Acad. Sci.* **113**, 8236–8241 (2016).

144. Gregory Fettweis *et al.* The mineralocorticoid receptor forms higher order oligomers upon DNA binding. *bioRxiv* 2023.01.26.525752 (2023) doi:10.1101/2023.01.26.525752.

145. Mayer, M., Reinstein, J. & Buchner, J. Modulation of the ATPase Cycle of BiP by Peptides and Proteins. *J. Mol. Biol.* **330**, 137–144 (2003).

146. Jan-Willem Meent, Jonathan Bronson, Frank Wood, Ruben Gonzalez Jr., & Chris Wiggins. Hierarchically-coupled hidden Markov models for learning kinetic rates from single-molecule data. in *Proceedings of the 30th International Conference on Machine Learning* (eds. Sanjoy Dasgupta & David McAllester) vol. 28 361–369 (PMLR, 2013).

147. van de Meent, J.-W., Bronson, J. E., Wiggins, C. H. & Gonzalez, R. L. Empirical Bayes Methods Enable Advanced Population-Level Analyses of Single-Molecule FRET Experiments. *Biophys. J.* **106**, 1327–1337 (2014).

148. Knarr, G., Gething, M.-J., Modrow, S. & Buchner, J. BiP Binding Sequences in Antibodies. *J. Biol. Chem.* **270**, 27589–27594 (1995).

149. Strub, A., Zufall, N. & Voos, W. The Putative Helical Lid of the Hsp70 Peptide-binding Domain is Required for Efficient Preprotein Translocation into Mitochondria. *J. Mol. Biol.* **334**, 1087–1099 (2003).

150. Tokunaga, M., Kato, S., Kawamura-Watabe, A., Tanaka, R. & Tokunaga, H. Characterization of deletion mutations in the carboxy-terminal peptide-binding domain of the Kar2 protein in Saccharomyces cerevisiae. *Yeast* **14**, 1285–1295 (1998).

151. Wei, J., Gaut, J. R. & Hendershot, L. M. In Vitro Dissociation of BiP-Peptide Complexes Requires a Conformational Change in BiP after ATP Binding but Does Not Require ATP Hydrolysis. *J. Biol. Chem.* **270**, 26677–26682 (1995).

152. Leskovar, A., Wegele, H., Werbeck, N. D., Buchner, J. & Reinstein, J. The ATPase Cycle of the Mitochondrial Hsp90 Analog Trap1 *. *J. Biol. Chem.* **283**, 11677–11688 (2008).

153. Theodoraki, M. A. & Caplan, A. J. Quality control and fate determination of Hsp90 client proteins. *Heat Shock Protein 90 Hsp90* **1823**, 683–688 (2012).

154. Whitesell, L., Mimnaugh, E. G., De Costa, B., Myers, C. E. & Neckers, L. M. Inhibition of heat shock protein HSP90-pp60v-src heteroprotein complex formation by benzoquinone

ansamycins: essential role for stress proteins in oncogenic transformation. *Proc. Natl. Acad. Sci.* **91**, 8324–8328 (1994).

155. Rodina, A. *et al.* Selective compounds define Hsp90 as a major inhibitor of apoptosis in small-cell lung cancer. *Nat. Chem. Biol.* **3**, 498–507 (2007).

156. Hoxie, R. S. & Street, T. O. Hsp90 chaperones have an energetic hot-spot for binding inhibitors. *Protein Sci. Publ. Protein Soc.* **29**, 2101–2111 (2020).

157. Amaral, M. *et al.* Protein conformational flexibility modulates kinetics and thermodynamics of drug binding. *Nat. Commun.* **8**, 2276 (2017).

158. LaRussa, S. A. The R102A Mutation Uncovers the Inhibitory Roles of ATP in Grp94. *ProQuest Dissertations and Theses* (Brandeis University, 2023).

159. Mishra, P. & Bolon, D. N. A. Designed Hsp90 Heterodimers Reveal an Asymmetric ATPase-Driven Mechanism In Vivo. *Mol. Cell* **53**, 344–350 (2014).

160. Mader, S. L. *et al.* Conformational dynamics modulate the catalytic activity of the molecular chaperone Hsp90. *Nat. Commun.* **11**, 1410 (2020).

161. Elnatan, D. & Agard, D. A. Calcium binding to a remote site can replace magnesium as cofactor for mitochondrial Hsp90 (TRAP1) ATPase activity. *J. Biol. Chem.* **293**, 13717–13724 (2018).

162. Prodromou, C. *et al.* Identification and Structural Characterization of the ATP/ADP-Binding Site in the Hsp90 Molecular Chaperone. *Cell* **90**, 65–75 (1997).

163. Millson, S. H. *et al.* Features of the Streptomyces hygroscopicus HtpG reveal how partial geldanamycin resistance can arise with mutation to the ATP binding pocket of a eukaryotic Hsp90. *FASEB J.* **25**, 3828–3837 (2011).

164. Pettersen, E. F. *et al.* UCSF Chimera—A visualization system for exploratory research and analysis. *J. Comput. Chem.* **25**, 1605–1612 (2004).

165. Huynh, K. & Partch, C. L. Analysis of Protein Stability and Ligand Interactions by Thermal Shift Assay. *Curr. Protoc. Protein Sci.* **79**, 28.9.1-28.9.14 (2015).

APPENDIX A: Compilation of Measured Dissociation Constants

	Labeled Protein	Titrated Protein	K_D (μM)	pH	KCl (mM)	Nucleotide	Temp (°C)
FP	Site 1	BiP	0.95±0.17	6	50	HK-ADP	37
			13±2	6	50	ATP	37
			0.69±0.08	6	150	HK-ADP	37
			14±0.5	6	150	ATP	37
			0.46±0.06	6	300	HK-ADP	37
			16±1.9	6	300	ATP	37
			0.46±0.05	6	450	HK-ADP	37
			15±3.5	6	450	ATP	37
		BiP T229A	20±3	6	50	ATP	37
		BSA	13±2	6	50	ADP	37
	Site 2	BiP	5.3±0.6	6	50	HK-ADP	37
			5.8±0.5	6	150	HK-ADP	37
			4.3±0.5	6	300	HK-ADP	37
	Site 3	BiP	15±1	6	50	HK-ADP	37
			12±1.6	6	300	HK-ADP	37
	mIGF2	BiP	2.7±1	6	50	HK-ADP	37
			9.7±4.5	6	50	ATP	37
	Ext. Site 1	BiP	0.67±0.17	6	50	HK-ADP	37
			8±3.8	6	50	ATP	37
			0.72±0.11	6	150	HK-ADP	37
			0.85±0.21	6	300	HK-ADP	37
	Ext. Site 1 + Site 2	BiP	0.52±0.13	6	50	HK-ADP	37
			1.9±0.6	6	50	ATP	37
			0.82±0.19	6	150	HK-ADP	37
			0.86±0.07	6	300	HK-ADP	37
FRET	BiP	E-peptide	0.015±0.005	6	50	ADP	37
			0.098±0.01	6	50	ATP	37
			0.019±0.004	6	50	ADP + 5% ATP	37
			0.03±0.01	6	75	ADP	37
			0.16±0.04	6	75	ATP	37
			0.12±0.05	6	150	ADP	37
			0.68±0.07	6	150	ATP	37
			0.39±0.08	6	300	ADP	37
			0.45±0.1	6	450	ADP	37
			0.25±0.06	6	50	ATP	37
		E-peptide +6	0.35±0.01	6	50	ATP	37
		E-peptide +3	1.44±0.04	6	50	ATP	37
		E-peptide 92-132	0.15±0.04	6	50	ADP	37
			1.3±0.2	6	50	ATP	37
		Ext. Site 1 + Site 2	0.05±0.01	6	50	ADP	37
			0.85±0.06	6	50	ATP	37

Table A.1. Compilation of dissociation constants presented in Chapter 2. Errors are the SEM of at least three measurements.

	Labeled Protein	Titrated Protein	Other	K_D (μM)	pH	KCl (mM)	Nucleotide	Temp (°C)
FP	BiP	Grp94		0.16±0.06	7	50	HK-ADP	30
			0.556M Urea	0.24±0.02	7	50	HK-ADP	30
			2.5μM $proIGF2_{25-120}$	0.55±0.05	7	50	HK-ADP	30
			5μM $proIGF2_{25-120}$	0.95±0.2	7	50	HK-ADP	30
			9μM $proIGF2_{25-120}$	1.8±0.65	7	50	HK-ADP	30
		NM Grp94		1.47±0.17	7	50	HK-ADP	30
		$Grp94_{Monomer}$		0.24±0.02	7	50	HK-ADP	30
		Grp94 W654A		0.23±0.02	7	50	HK-ADP	30
		Grp94 M662A		0.25±0.02	7	50	HK-ADP	30
	BiP NBD	Grp94		1.12±0.16	7	50	HK-ADP	30
			0.556M Urea	2.4±0.63	7	50	HK-ADP	30
			2.5μM $proIGF2_{25-120}$	1.04±0.05	7	50	HK-ADP	30
			5μM $proIGF2_{25-120}$	1.68±0.18	7	50	HK-ADP	30
			9μM $proIGF2_{25-120}$	2.06±0.12	7	50	HK-ADP	30
		NM Grp94		1.77±0.1	7	50	HK-ADP	30
		$Grp94_{Monomer}$		1±0.09	7	50	HK-ADP	30
	$proIGF2_{25-120}$	BiP		2.5±0.4	7	50	HK-ADP	30
				3.8±1.4	7	50	ATP	30
		BiP T229A		3.5±0.6	7	50	ATP	30
		BiP, Grp94		3.7±0.7*	7	50	HK-ADP	30
	Ext Site 1	BiP		1.9±0.5	7	50	HK-ADP	30
				5.5±0.5	7	50	ATP	30
	Site 1	BiP		2.5±0.7	7	50	HK-ADP	30
				16±3.8	7	50	ATP	30
FRET	WT/WT Grp94	BiP NBD		0.61±0.05	7.5	50	Apo	30
	WT/K467A Grp94	BiP NBD		5.2±0.94	7.5	50	Apo	30

Table A.2. Compilation of dissociation constants presented in Chapter 3. Errors are the SEM of at least three measurements. *Grp94 expressed in monomer concentration.

	Labeled Protein	Titrated Protein	K_D (μM)	pH	KCl (mM)	Nucleotide	Temp (°C)
FP	BiP NBD	Grp94	0.23±0.01	8	50	Apo	37
		Grp94 L163A	0.28±0.01	8	50	Apo	37
		Grp94 F199A	0.18±0.02	8	50	Apo	37

Table A.3. Compilation of dissociation constants presented in Chapter 4. Errors are the SEM of at least three measurements.

	Labeled Protein	Titrated Protein	Other	K_D (μM)	pH	KCl (mM)	Nucleotide	Temp (°C)
FP	BiP	Grp94	50μM Hsp990	0.35±0.01	7	50	HK-ADP	30
			100μM Hsp990	0.37±0.01	7	50	HK-ADP	30
			50μM AUY922	0.2±0.01	7	50	HK-ADP	30
	BiP NBD	Grp94		0.32±0.01	8	50	Apo	25
	$proIGF2_{25-120}$	BiP		1.01±0.12	7	50	HK-ADP	37
				7.85±0.82	7	50	ATP	37
	Ext. Site 1	BiP		1.63±0.43	7	50	HK-ADP	37
	Site 1	BiP		1.5±0.2	7.5	50	HK-ADP	37
				11±3.3	7.5	50	ATP	37

Table A.4. Compilation of miscellaneous dissociation constants. Errors are the SEM of at least three measurements.

APPENDIX B: Fit Parameters of Single Molecule FRET Efficiency Histograms

Condition	Low FRET Gaussian	High FRET Gaussian	Figure
$Grp94_D$/BiP SBD_A smFRET Integration Time: 250ms Number of Traces: 94 R = 0.992	ε = 0.327±0.004 σ = 0.122±0.002 P = 0.40	ε = 0.725±0.002 σ = 0.122±0.002 P = 0.60	3.9.A
$Grp94_D$/BiP SBD_A smFRET Integration Time: 65ms Number of Traces: 60 R = 0.982	ε = 0.340±0.004 σ = 0.110±0.002 P = 0.53	ε = 0.697±0.004 σ = 0.110±0.002 P = 0.47	3.9.B

Table B.1. Fit Parameters of Gaussian Fitting of Single Molecule FRET Efficiency Histograms with Fixed σ Values. ε is the mean FRET efficiency of a state, σ is the standard deviation of the gaussian, P is the fraction of the total population in the FRET state. Errors are the fitting error. R is the correlation coefficient.

Condition	Low FRET Gaussian	High FRET Gaussian	Figure
$Grp94_D$/BiP SBD_A smFRET Integration Time: 1s Number of Traces: 64 R= 0.997	ε = 0.400±0.006 σ = 0.132±0.006 P = 0.36	ε = 0.730±0.003 σ = 0.110±0.002 P = 0.64	3.8.B
$Grp94_D$/BiP SBD_A smFRET Integration Time: 250ms Number of Traces: 94 R = 0.992	ε = 0.326±0.005 σ = 0.131±0.008 P = 0.42	ε = 0.727±0.003 σ = 0.119±0.003 P = 0.58	3.9.D
$Grp94_D$/BiP SBD_A smFRET Integration Time: 65ms Number of Traces: 60 R= 0.983	ε = 0.338±0.004 σ = 0.104±0.005 P = 0.50	ε = 0.693±0.005 σ = 0.116±0.005 P = 0.50	3.9.D

Table B.2. Fit Parameters of Gaussian Fitting of Single Molecule FRET Efficiency Histograms with Floating σ Values. ε is the mean FRET efficiency of a state, σ is the standard deviation of the gaussian, P is the fraction of the total population in the FRET state. Errors are the fitting error. R is the correlation coefficient.